Summer 8-15-2017

Hollow and Porous Plasmonic Nanostructures for Highly Efficient Chemical and Biological Sensing

Keng-Ku Liu
Washington University in St. Louis

WASHINGTON UNIVERSITY IN ST. LOUIS

Institute of Materials Science and Engineering

Dissertation Examination Committee:
Srikanth Singamaneni, Chair
Parag Banerjee
Guy Genin
Jeremiah Morrissey
Bryce Sadtler

Hollow and Porous Plasmonic Nanostructures for Highly Efficient Chemical and Biological Sensing

by

Keng-Ku Liu

A dissertation presented to
The Graduate School
of Washington University in
partial fulfillment of the
requirements for the degree
of Doctor of Philosophy

August, 2017

Saint Louis, Missouri

Table of Contents

List of Figures

List of Abbreviations

LSPR	Localized surface plasmon resonance
SERS	Surface enhanced Raman scattering
SPR	Surface plasmon resonance
EM	Electromagnetic
RIU	Refractive index unit
AuNCs	Au nanocages
AuNR	Au nanorod
AuNP	Au nanoparticle
AuNS	Au nanosphere
AKI	Acute kidney injury
NGAL	Neutrophil gelatinase-associated lipocalin
IL-18	Interleukin-18
KIM-1	Kidney injury molecule-1
CysC	Cystatin C
FABP	Fatty acid-binding protein
CKD	Chronic kidney disease
ICU	Intensive care unit
EG	Ethylene glycol
CTAB	Cetyltrimethylammonium bromide
CTAC	Cetyltrimethylammonium chloride
PVP	Poly(vinyl pyrrolidone)
2-NT	2-naphthalenethiol
PSS	Poly(styrene sulfonate)
PAH	Poly(allylamine hydrochloride)

P2VP	Poly(2-vinyl pyridine)
pATP	4-aminothiophenol
GA	Glutaraldehyde
TMPS	Trimethoxypropylsilane
APTMS	(3-aminopropyl)trimethoxysilane
SDS	Sodium dodecyl sulfate
PBS	Phosphate buffered saline
TEM	Transmission electron microscope
SEM	Scanning electron microscope
UV-Vis	Ultraviolet-visible
Vis-NIR	Visible-Near infrared
FDTD	Finite-difference time-domain
DDA	Discrete dipole approximation
FOM	Figure of merit
FWHM	Full width at half maximum
LbL	Layer-by-layer
PEM	Polyelectrolyte multilayers

Acknowledgements

First and foremost, I would like to thank my advisor Prof. Srikanth Singamaneni, without him none of this would have been possible. I appreciate his taking me into his group, providing me an excellent atmosphere for doing research, and teaching me how to perform research. I still remember that he took me for a lab trip and gave me the lab key on the first day that I met him. The enthusiasm he has for science and research was motivational for me. He always encouraged me to think independently. I am thankful for the excellent example he has provided and it will continue to inspire me in my future career.

I thank my PhD committee Prof. Parag Banerjee, Prof. Guy Genin, Prof. Jeremiah Morrissey, and Prof. Bryce Sadtler for their valuable advice, insightful comments, and input on my research.

I would like to thank all the previous and current members of the soft nanomaterials lab: Dr. Naveen Gandra, Dr. Limei Tian, Dr. Saide Zeynep Nergiz, Dr. Amit Jaiswal, Dr. Bo Hu, Dr. Guoyou Huang, Dr. Rong Hu, Dr. Congzhou Wang, Dr. Hongcheng Sun, Dr. Huzeyfe Yilmaz, Dr. Ailing Feng, Sirimuvva Tadepalli, Qisheng Jiang, Sisi Cao, Jingyi Luan, Zheyu Wang, Hamed Gholami Derami, Rohit Gupta, Jie Hu, Ting Xu, Marilee Fisher, Sang hyun Park, Max Fei, Christopher Portz, Emily Lu Wang, Sang hyun Bae, Abishek Venkatesan Iyer, Jieun Yim, Abigail Andresen for creating an excellent atmosphere for research and their valuable discussions and research assistance. Additionally, I would like to thank all my friends. My time in St. Louis has been a lot of fun due to the many colleagues and friends.

Most of all, I am indebted to my parents for giving me an excellent upbringing and education and supporting me in all my pursuits. Thank my family members for all their love, support, and encouragement.

Finally, I would like to thank my wife, Shu-Yu Lin. She was always there supporting and encouraging me. Thank you.

Keng-Ku Liu

Washington University in St. Louis

August 2017

Abstract of the Dissertation

Hollow and Porous Plasmonic Nanostructures for Highly Efficient Chemical and Biological Sensing

by

Keng-Ku Liu

Doctor of Philosophy in Materials Science and Engineering

Washington University in St. Louis, 2017

Professor Srikanth Singamaneni, Chair

Localized surface plasmon resonance (LSPR) involves the collective and coherent oscillation of dielectrically confined conduction electrons. The LSPR wavelength of noble metal nanoparticles (such as gold, silver and copper), which falls into the visible and near infrared range of the electromagnetic spectrum, is sensitive to the composition, size, shape, dielectric properties of the surrounding medium, and proximity to other nanostructures (plasmon coupling). Based on the sensitivity of the surface plasmon resonance to the changes in the dielectric properties of the surrounding medium and the enhancement of the electromagnetic (EM) field in proximity of metal nanostructures, two important classes of plasmonic sensors have evolved: refractometric LSPR and surface enhanced Raman scattering (SERS) sensors. SERS involves the large enhancement of the Raman scattering from analytes adsorbed on or in close proximity to a nanostructured metal surface.

Most of the SERS substrates based on individual nanostructures offer modest SERS enhancement. On the other hand, interstitial sites between assembled or lightly aggregated nanostructures, often termed as electromagnetic hotspots, offer large SERS signal enhancements, enabling the single molecule detection under ideal conditions. Although the assemblies of

nanostructures are highly SERS-active, the SERS response is very sensitive to the assembly state, thus making it challenging to realize uniform and reproducible SERS substrates with high density of EM hotspots based on such traditional assemblies. Furthermore, the fabrication of SERS substrates based on the controlled assemblies of nanostructures involves either complex chemical methods or expensive lithographic techniques. Therefore, it is desirable to engineer nanostructures with inherent EM hotspots, which can significantly enhance the EM field and enable the sensitive detection of analytes using SERS.

Hollow and porous metal nanostructures are a novel class of plasmonic nanostructures that exhibit extraordinary optical and catalytic properties compared to their solid counterparts, due to a higher surface to volume ratio and the facile tunability of the LSPR wavelength over a broad range from visible to parts of near infrared. In this work, we design, synthesize, and comprehensively characterize the optical properties of hollow nanostructures including plasmonic nanocages and nanorattles comprised of gold nanostructures as cores and porous gold cube as shells. We demonstrate that hollow and porous plasmonic nanostructures exhibit a significantly higher refractive index sensitivity compared to other solid nanostructures of similar size, leading to LSPR sensors with higher sensitivity and lower limit-of-detection compared to biosensors based on solid counterparts. Furthermore, we demonstrate that plasmonic nanorattles host electromagnetic hotspots between the core and the shell, offering significantly higher SERS enhancement as compared to other solid nanostructures of similar size. Through a systematic study, we unveil the influence of size, shape and orientation of the plasmonic nanorattles on the optical properties and SERS enhancement. The work described here provides guidelines for the design of hollow plasmonic nanostructures for various sensing applications.

Chapter 1: Introduction

1.1 Localized Surface Plasmon Resonance

Surface plasmons involve the collective coherent oscillation of the conductive electrons at the interface of a metal and dielectric material. A broad term, plasmonics involves the control of light at the nanoscale using surface plasmons.[1,2,3,4,5,6,7,8,9] One particular area where plasmonics is expected to make an enoromous impact is the field of life sciences with applications in imaging, diagnosis, and therapeutics.[10,11,12,13] Based on the sensitivity of the surface plasmon resonance to the dielectric ambient and the enhancement of electromagnetic (EM) field in proximity to metal nanostructures, two important classes of plasmonic sensors have evolved: surface plasmon resonance (SPR) and surface enhanced Raman scattering (SERS).[14,15] Conventional SPR sensors rely on propagating surface plasmons at the interface of the thin metal films and a dielectric medium. The sensitivity of the SPR to the changes in the dielectric medium is exploited in sensing applications, which is currently a well-established technique for biosensing and probing thermodynamic and kinetic aspects of biomolecule binding.[16,17] Although extremely sensitive, conventional SPR suffers from complexity in exciting the surface plasmons (requiring complex optical alignment or wave coupling systems such as prisms) and more importantly it lacks the spatial resolution to address single or few molecule events.

On the other hand, excitation of surface plasmons in metal nanostructures does not require a specialized setup, simplifying the operation and making them more appropriate for on-chip, cost-effective and point-of-care diagnostics. The time varying electric field of the EM radiation causes oscillation of conductive electrons in the nanoparticles and the resonance condition, termed localized surface plasmon resonance (LSPR), falling into the visible regime for noble

metals such as gold, silver and copper. The LSPR of the metal nanostructures is sensitive to numerous factors such as composition, size, shape, dielectric medium, and proximity to other nanostructures (plasmon coupling).[18,19] The sensitivity of LSPR to localized changes (10-20 nm from nanoparticle surface) in dielectric medium renders it an attractive transduction platform for chemical and biological sensing.[20,21,22,23,24]

LSPR offers distinct advantages compared to traditional SPR approach:[25,26,27] (i) low bulk sensitivity (ii) simplicity in detection (iii) high spatial resolution down to single nanoparticle and (iv) facile integration with device platforms for developing point-of-care assays. LSPR is shown to be sensitive enough to differentiate various inert gases (refractive index difference on the order of 3×10^{-4} refractive index units (RIU)), to probe the conformational changes of individual biomacromolecules, to detect single biomolecule binding events, to monitor the kinetics of catalytic activity of single nanoparticles and even optically detect single electron.[28,29,30,31,32]

1.2 Surface enhanced Raman scattering

Despite the rich molecular information provided by Raman spectroscopy, the technique was not considered to be a handy analytical tool (let alone detection tool) due to the extremely weak signal intensity of normal Raman scattering, a result of the extremely small scattering cross-section for most molecules.[33, 34] Hence, for the longest period after its discovery, Raman scattering has remained limited to "bulk" investigations. Surface enhanced Raman scattering (SERS), which brings the dramatic enhancement of the Raman scattering of an analyte that is adsorbed on or in close proximity to a metal surface, is emerging as a powerful technique for the trace level detection of various biological and chemical species and believed to make a huge impact on life sciences, environmental monitoring and homeland security.[1, 2, 3, 4, 5, 16, 35]

Despite the initial controversy, at present there is a consensus that the enhancement of the Raman signal originates from two distinct contributions, namely, electromagnetic enhancement and chemical enhancement with the former effect being several orders of magnitide higher than the latter.[36,37] When the excitation light is in resonance with the plasmon frequency of the metal nanoparticle, it results in dipolar radiation causing a characteristic spatial distribution in which certain areas show higher intensity, which is manifested as an electromagnetic enhancement. Analyte molecules subjected to this enhanced electromagnetic field exhibit a dramatic enhancement in Raman scattering. Electromagnetic enhancement critically depends on numerous factors such as the distance between the metal nanostructures, size and shape (i.e. antenna effect) of the nanostructures, composition of the metal, and the excitation wavelength with respect to the plasmon resonance of the metal nanostructures.[38,39,40,41,42]

Numerous SERS substrates from roughened noble metal surfaces to e-beam patterned metal nanostructures with enhancement factors ranging from 10^4 to 10^{10} have been demonstrated over the last two decades.[4,9,15,43,44] Very high enhancement factors ($> 10^9$) have been reported for SERS substrates fabricated from top-down and bottom-up approaches such as e-beam lithography, colloidal lithography, on-wire lithography and self- and directed-assembly, which enable precise control over the size, shape, and organization of the metal nanostructures.[45,46,47,48,49] On the other hand, 3D SERS substrates such as photonic crystal fibers and porous alumina membranes decorated with nanoparticles and periodic nanohole arrays also offer large SERS enhancements (10^6 - 10^9) owing to the large surface area within the source laser footprint and efficient light-matter interaction compared to the 2D counterparts.[26,50,51,52,53]

1.3 Hollow and Porous Metal Nanostructures

Hollow and porous metal nanostructures are a relatively novel class of plasmonic nanostructures. Owing to the higher surface to volume ratio and facile tunability of LSPR wavelength over a broad range from visible to parts of near infrared, hollow and porous metal nanostructures exhibit extraordinary optical and catalytic properties compared to their solid counterparts. Hollow and porous metal nanostructures provide large specific surfaces can serve as carriers for encapsulating multi-functional active materials.[32,54,55] In addition, these nanostructures have been employed for photothermal therapy, contrast agents in bioimaging, catalysts and nanotransducers in biological and chemical sensing.[56,57,58] Among the various reported synthesis methods, galvanic replacement reaction can be used for producing bi- and tri-metallic hollow nanostructures with well-controlled morphologies.[59] Galvanic replacement reaction is an electrochemical reaction which involves the oxidation of one metal with lower reduction potential (which served as a sacrificial template) by the ions of another metal with higher reduction potential. As an effective and simple method, galvanic replacement has been widely employed for the fabrication of hollow and porous nanostructures.

1.4 Motivation and Rationale

Most of the SERS substrates based solely on individual nanostructures offer modest SERS enhancement. On the other hand, interstices between assembled or lightly aggregated nanostructures, often termed as electromagnetic hot spots, offer large SERS signal enhancements, enabling single molecule detection under ideal conditions.[15, 60-62] Although the assemblies of nanostructures are highly SERS-active, the SERS response is very sensitive to the assembly state, thus making it challenging to realize uniform and reproducible SERS substrates with high

density of EM hot spots based on such traditional assemblies.[19, 63] Furthermore, fabrication of SERS substrates based on controlled assemblies of nanostructures involves either complex chemical methods or expensive lithographic techniques.[20, 64-67] Therefore, it is desirable to engineer nanostructures with inherent EM hot spots, which can significantly enhance the EM field and enable sensitive detection of analytes using SERS.[68] In this context, we seek to design and demonstrate gold nanorattles comprised of Au nanostructures (particles or rods) as core and porous gold cube as shell. We hypothesize that the unique structure of the nanorattle results in the formation of an electromagnetic hotspot between the core and the shell. Such nanostructures with inherent electromagnetic hotspots are expected to offer significantly higher SERS enhancement as compared to other solid nanostructures of similar size (e.g., Au nanocubes). Inherent hotspots within the nanostructures will obviate the need for controlled aggregation or assembly of nanostructures to realize electromagnetic hot-spots that are critical for ultrasensitive SERS-based chemical detection.

Hollow and porous plasmonic nanostructures also exhibit significantly higher refractive index sensitivity compared to other solid nanostructures of similar size due to the electromagnetic hotspots within the nanostructures. We envision that these hollow and porous plasmonic nanostructures would enable highly sensitive, specific and stable sensing. Apart from systematically investigating the refractive index sensitivity and electromagnetic decay length of hollow plasmonic nanostructures in comparison to their solid counterparts, we propose to realize a plasmonic biosensor by molecularly imprinting the nanostructures. Specifically, we propose to develop a plasmonic biosensor for the detection of urine biomarkers for acute kidney injury (AKI). AKI is a complex clinical condition whose underlying pathogenesis remains incompletely understood.[69,70,71] Over the same time period, the number of deaths associated with

dialysis-requiring AKI has more than doubled.[72] In a wide variety of common chronic kidney diseases (CKD), renal neutrophil gelatinase-associated lipocalin (NGAL) synthesis and excretion in the urine are increased by almost 10-fold. During AKI, urinary NGAL levels are increased by several log-orders of magnitude while plasma levels increase 5 to10-fold. In an extensive review encompassing many biomarkers of kidney injury, plasma and urine levels of NGAL alone provided early detection and prognosis of patients at risk of developing AKI and supported the differential diagnosis of established AKI.[73,74] Thus, the measurement of plasma and/or urine NGAL levels is of clinical importance such that companies have marketed NGAL assays all of which are immune-based. Therefore, it is a critical need for a low-cost, simple, stable and reliable NGAL assay. The above considerations clearly suggest the need for a label-free approach for rapid and quantitative detection of the proteins in urine at physiologically relevant concentrations (ng/ml).

Most of the existing LSPR-based plasmonic sensing rely on natural antibodies for the capture of target biomolecules. However, natural antibodies suffer from numerous shortcomings such as poor chemical stability, limited shelf-life and excessive cost. In addition, lack of chemical selectivity plague the progress of LSPR-based sensors to the real-world applications. To overcome these issues, we will explore an alternate approach, which involves the use of artificial antibodies that exhibit excellent recognition capabilities (comparable to natural antibodies) and remarkable stability over a wide range of conditions. The design and synthesis of such biomimetic materials capable of recognizing target biomolecules with high affinity and specificity will be performed using molecular imprinting of synthetic polymers.[75]

1.5 Research Goals and Objectives

The ultimate goal of the research is to design and demonstrate a novel class of hollow and porous plasmonic nanostructures for highly efficient detection of trace amounts of chemical and biological analytes based on the LSPR and SERS. Specific objectives are as follows:

Objective 1: Synthesis of size- and shape-controlled hollow and porous plasmonic nanostructures. We will synthesize hollow and porous metal nanostructures of different sizes and shapes (such as cubes and cuboids) using template-mediated method. The ability to precisely control the size and shape of nanostructures is critical for their use as ultrasensitive nanotransducers.

Objective 2: Establish criteria for the rational selection of plasmonic nanostructures for chemical- and biological-sensing applications. Owing to the unique optical properties such as highly tunable LSPR, large refractive index sensitivity, tunable electromagnetic decay length, and large enhancement in the EM field, hollow plasmonic nanostructures are considered to be highly promising candidates for SERS and label-free LSPR-based biosensing. However, detailed investigations correlating the size, shape, orientation (in the case of anisotropic nanostructures) to the SERS activity and LSPR sensitivity is missing. Such an investigation will provide the design criteria for rational choice of hollow plasmonic nanostructures for the chosen transduction platform. We will undertake such detailed investigations using the size- and shape-controlled nanostructures synthesized using template-mediated methods.

Objective 3: Design and demonstrate a plasmonic biosensor based on artificial antibodies and hollow plasmonic nanostructures. In this task, we will design and demonstrate a plasmonic biosensor based on hollow and porous plasmonic nanostructures and artificial antibodies for the sensitive and specific detection of target biomarkers. Although it has been

predicted that hollow nanostructures exhibit significantly higher refractive index sensitivity compared to solid nanoparticles like nanospheres, nanocubes, and nanorods, there have been no reports on the use of hollow nanostructures as plasmonic nanotransducers for biosensing. Successful completion of this task will lay the groundwork for realizing a novel class of biosensors based on hollow plasmonic nanostructures.

Objective 4: Optimizing the SERS activity of plasmonic nanorattles by controlling the extent of galvanic replacement during template-mediated synthesis. In this objective, we will probe the SERS activity of plasmonic nanorattles with different degrees of galvanic replacement to determine the optimal structure for maximum SERS activity. We will use 2-naphthalenethiol (2-NT), a widely employed as a model analyte for SERS owing to its ability to readily adsorb on gold, coated on AuNP followed by silver layer growth. SERS activity will be monitored by adding various amount of gold salt ($HAuCl_4$). Plasmonic nanorattles with optimal structure and inherent electromagnetic hotspots are highly attractive for SERS-based chemical sensing and bioimaging.

1.6 Overview of the Dissertation

This dissertation is organized into the following sections: (i) Development of size- and shape-controlled hollow and porous plasmonic nanostructures for LSPR and SERS applications. (ii) Design and demonstrate LSPR- and SERS-based biological and chemical sensor. (iii) Establish criteria for rational selection of plasmonic nanostructures for chemical and biological sensing applications.

Chapter 2 describes the synthesis of hollow plasmonic nanostructures with high refractive index sensitivity of LSPR for the biological sensing. We demonstrate gold nanocages (AuNCs), a novel class of hollow and porous nanostructures, exhibit significantly higher refractive index

sensitivity and lower EM decay length, both of which make it an excellent candidate for plasmonic biosensing. AuNCs with built-in artificial antibodies achieved by molecular imprinting approach enabled the detection of a kidney injury biomarker (NGAL) down to a concentration of 25 ng/ml. The limit of detection (LOD) achieved with AuNCs as nanotransducers is more than an order of magnitude lower compared to that obtained with AuNRs. Molecularly imprinted AuNCs exhibit excellent selectivity against numerous interfering urinary proteins and remarkable stability over a wide range of pH ranging from 4.5 to 8.5 and specific gravities from 1.005 to 1.030.

In Chapter 3, we systematically investigate the size- and shape-dependent SERS activity of plasmonic nanorattles comprised of Au nanospheres and nanorods as cores and porous Au nanocubes and cuboids as shells. We demonstrate that the increase in the SERS activity of the cubic nanorattles is due to the increase in the extinction (and scattering) coefficient of nanostructures with size. On the other hand, the SERS activity of the plasmonic nanorattles with nanorod cores decreased with the increase in the edge length of the porous cuboid shells. In the case of the cuboid nanorattles, the electromagnetic hotspot within the nanostructure, formed between the edge of the AuNR and porous Au shell, governs the SERS activity.

Chapter 4 describes the polarization-dependent SERS activity of an individual cuboidal plasmonic nanorattle and its solid counterpart *i.e.* Au@Ag nanocuboid. Due to the presence of internal electromagnetic hotspots within the nanorattles, they exhibited SERS activity with a significantly different polarization-dependence compared to their solid counterparts i.e. AuNR@Ag nanocuboids. Similar to most conventional anisotropic solid nanostructures, the nanocuboids exhibited a polarization-dependent SERS activity that is dominated by their sharp corners and edges. Conversely, for the cuboidal nanorattles, the internal electromagnetic hotspot

formed between the AuNR core and the porous Ag-Au shell dominates the SERS activity of the nanorattles. Computational simulations based on the finite-difference time-domain (FDTD) method were employed to understand the electromagnetic field distribution and the SERS enhancement from the plasmonic nanostructures, which also corroborate our experimental findings.

In Chapter 5, plasmonic nanorattles with various extent of galvanic replacement have been fabricated during template-mediated synthesis. Raman reporter (2-NT) was trapped between Au-Ag core-shell nanostructure, which was employed to monitored the SERS activity of nanorattles. The presence of internal electromagnetic hotspots enabled the nanorattles to serve as highly efficient SERS probes. Paper substrates adsorbed with Au nanorattles enabled the trace detection of analyte (4-aminothiophenol, pATP) down to a concentration of 1 pM.

Chapter 6 describes the swelling-mediated massive reconstruction of an ultrathin responsive gelatinous polymer film uniformly adsorbed with plasmonic nanostructures into a randomized network of interacting folds, resulting in bright electromagnetic hotspots within the folds. We reveal a strong correlation between the topology and near-field electromagnetic field enhancement due to the intimate contact between two plasmonic surfaces within the folds, each of them representing a unique combination of local topography and chemical distribution caused by the formation of electromagnetic hotspots. Owing to the efficient trapping of the Raman reporters within the uniquely distributed electromagnetic hotspots, the SERS enhancement from the morphed plasmonic gel was found to be nearly 40 times higher compared to that from the pristine plasmonic gel. Harnessing the nondeterministic nature of the folds, the folded plasmonic gel can be employed as a multidimensional (with dual topo-chemical encoding) optical taggant for prospective anti-counterfeiting applications.

Chapter 2: Gold Nanocages with Built-in Artificial Antibodies for Label-free Plasmonic Biosensing

The results reported in this chapter were published in Journal of Materials Chemistry B, 2014, 2, 167-170. Reproduced with permission from The Royal Society of Chemistry.

2.1 Abstract

We demonstrate that gold nanocages (AuNCs) with built-in artificial antibodies enable the detection of kidney injury biomarker from synthetic urine down to a concentration of 25 ng ml^{-1}. Molecularly imprinted AuNCs exhibit excellent selectivity against numerous interfering urinary proteins and remarkable stability over a wide range of pH and specific gravity.

2.2 Introduction

The refractive index sensitivity of localized surface plasmon resonance (LSPR) of plasmonic nanostructures renders it an attractive transduction platform for chemical and biological sensing.[13, 76-86] Metal nanostructures of different sizes, shapes and composition and assemblies of metal nanostructures are being extensively investigated as transducers for plasmonic chemical and biological sensing.[13, 76, 83, 86] Gold nanocages (AuNCs), a novel class of hollow plasmonic nanostructures, are an attractive platform for theranostic applications; thanks to their highly tunable localized surface plasmon resonance (LSPR) into the near infrared (NIR) where the endogenous absorption coefficient of living tissue is nearly two orders magnitude smaller compared to that in the visible range.[87] Owing to their large scattering and absorption cross sections, AuNCs have also been employed as contrast agents in optical coherence tomography,

photoacoustic imaging and photothermal therapy.[88-90] So far, there have been only a few reports on biosensing application of AuNCs, none of which employ AuNCs as nanotransducers.[91, 92] Although it has been predicted that hollow nanostructures exhibit significantly higher refractive index sensitivity compared to solid nanoparticles like nanospheres, nanocubes, and nanorods, to the best of our knowledge, there have been no reports on the use of gold nanocages as plasmonic nanotransducers for biosensing.[93, 94]

Most of the existing plasmonic sensors rely on natural antibodies for the capture of target biomolecules (*e.g.,* disease biomarkers). However, natural antibodies suffer from numerous shortcomings such as poor chemical stability, excessive cost and limited shelf-life. Moreover, they pose a significant challenge in efficient integration with abiotic micro- and nanotransduction platforms. In this communication, we demonstrate AuNCs with built-in artificial antibodies by molecular imprinting for the sensitive and specific detection of target biomarkers in physiological fluids such as urine.

2.3 Experimental Section

Materials: Ethylene glycol (Lot. no K26B01) and sodium sulfide (Na_2S) were purchased from J. T. baker. Cetyltrimethylammonium bromide (CTAB), ascorbic acid, sodium borohydride, poly(styrene sulfonate) (PSS) (Mw=70,000 g/mol), and poly(allyl amine hydrochloride) (PAH) (Mw=56,000 g/mol), sodium borohydride ($NaBH_4$), Silver nitrate (purity higher than 99%), 4-aminothiophenol (pATP), glutaraldehyde (GA), poly(vinyl pyrrolidone) (PVP, Mw~29,000), chloroauric acid ($HAuCl_4$), myoglobin from human heart (Mw=17.7 kDa), hemopexin from human plasma (Mw=57 kDa), α_1-antitrypsin from human plasma (Mw=52 kDa), α_1-acid glycoprotein from human plasma (Mw=40.8 kDa), albumin from human serum (Mw=66.5 kDa), and hemoglobins human (Mw=64.5 kDa) were obtained from Sigma-Aldrich. Sucrose was

purchased from G-Biosciences Inc. Poly(2-vinyl pyridine) (Mw=200,000 g/mol) was obtained from Scientific Polymer Products Inc. Artificial urine was purchased from Cerilliant Corp. Recombinant human fatty acid-binding protein 1 (FABP1) (MW=14.2 kDa), and recombinant human fatty acid binding protein-3 (FABP3) (MW=14.8 kDa) were obtained from RayBiotech, Inc. Recombinant neutrophil gelatinase associated lipocalin was obtained from SunnyLab (Kent, United Kingdom). All the chemicals have been used as received with no further purification.

Synthesis of silver nanocubes and gold nanocages (AuNCs): Prior to synthesis, all the glassware was cleaned using aqua regia (3:1 volume ratio of 37% hydrochloric acid and concentrated nitric acid). Silver nanocubes were synthesized using a sulfide-mediated method developed by Xia group.[95] Briefly, 90 μl of Na_2S solution (3 mM) in ethylene glycol was added to 6 ml of preheated ethylene glycol at 160 ^{0}C in a disposable glass vial. After 8 min, 1.5 ml of PVP (0.02 g/ml) in ethylene glycol was added to the above mixture, immediately followed by the addition of 0.5 ml of $AgNO_3$ (0.048 g/ml) in ethylene glycol. The reaction was complete in 10 min with a dark ruddy-red meniscus in reaction solution. The product was washed with acetone and water by centrifugation. 10 ml of aqueous PVP solution (9 mM) was add to 1 ml of the above-mentioned silver nanocubes solution. After bringing the suspension to a mild boil for approximately 10 min, 1 mM $HAuCl_4$ was injected at a rate of 0.5 ml/min under vigorous stirring until dark blue color appeared. The product was centrifuged once and redispersed in nanopure water before using (18.2 MΩ-cm).

Synthesis of gold nanorods: Gold nanorods were synthesized using a seed-mediated approach. Seed solution was prepared by adding 0.6 mL of an ice-cold solution of 10 mM sodium

borohydride into 10 mL of vigorously stirred 0.1 M CTAB and 2.5×10^{-4} M $HAuCl_4$ aqueous solution at room temperature. The color of the seed solution changed from yellow to brown. Growth solution was prepared by mixing 95 mL of 0.1 M CTAB, 1.0 mL of 10 mM silver nitrate, 5 mL of 10 mM $HAuCl_4$, and 0.55 mL of 0.1 M ascorbic acid in the same order. The solution was homogenized by gentle stirring. To the resulting colorless solution, 0.12 mL of freshly prepared seed solution was added and set aside in dark for 14 h. Prior to use, the AuNRs solution was centrifuged at 13,000 rpm for 10 min to remove excess CTAB and redispersed in nanopure water.

Adsorption of AuNR on glass surface: To adsorb gold nanocages onto glass substrates, the glass substrates were coated with poly(2-vinyl pyridine) (P2VP) by exposing the piranha cleaned substrates to 1 % (w/v) P2VP solution in ethanol.[96, 97] After rinsing the substrate with ethanol and drying with a stream of nitrogen, it was exposed to AuNCs solution for overnight to enable adsorption of the gold nanocages. Finally, the substrate was rinsed with water to remove the loosely bound nanocages, leaving a highly dense layer of nanocages on the surface.

Molecular Imprinting Procedure: Firstly, AuNC adsorbed glass substrate was placed in 2 ml of 100 mM $NaBH_4$ aqueous solution for 5 minutes with gentle shaking to remove PVP coating from AuNCs surface, followed by thorough rinsing with nanopure water.[98] Subsequently, AuNCs adsorbed on the substrate were modified with p-ATP and glutaraldehyde as crosslinkers by immersing the substrate in 2 ml of phosphate borate buffer (pH 8.3) containing 4 µl of glutaraldehyde (25 %) and 4 µl of pATP (4 mM in ethanol) for 1 minute, followed by rinsing with pH 8.3 buffer. In the next step, template protein (NGAL) was immobilized on nanocages by

exposing the substrate to 115 μg/ml of NGAL in pH 8.3 buffer solution at 4 °C for 2.5 hours, followed by rinsing with pH 8.3 buffer solution. Subsequently, the NGAL-coated substrate was immersed in 3 ml of phosphate buffered saline (PBS, pH 7.5) containing 15 μl of TMPS and 15 μl of APTMS for 40 minutes. Then the substrate was rinsed with buffer solution and stored in PBS solution at 4 °C overnight. Finally, proteins were released by shaking the substrate in 2 ml of oxalic acid (10 mM) in 2 % aqueous sodium dodecyl sulfate (SDS) solution.

NGAL detection and interfering proteins test: After removing template proteins, the molecularly imprinted AuNCs on glass substrates were immersed in 1 ml of different concentrations of NGAL in pH 8.3 buffer solution, followed by gently shaking for 30 minutes and then incubation at 4 °C for 3.5 hours. The same procedure was used to test interfering proteins, including myoglobin from human heart (10 μg/ml), hemopexin from human plasma (10 μg/ml), antitrypsin from human plasma (10 μg/ml), acid glycoprotein from human plasma (10 μg/ml), albumin from human serum (10 μg/ml), hemoglobin (10 μg/ml), FABP1 (1 μg/ml) and FABP3 (1 μg/ml). Extinction spectra were collected from at least three samples for different concentrations of NGAL and interfering proteins to obtain the average LSPR wavelength shift.

NGAL in different pH value and specific gravity of artificial urine test: The molecularly imprinted AuNCs coated substrates were immersed in 1 ml of 230 ng/ml NGAL in artificial urine with different pH (4.5, 5.5, 6.5, 7.5 and 8.5) and specific gravity (1.005, 1.010, 1.020, 1.030), followed by gently shaking for 30 minutes and incubation at 4 °C for 3.5 hours. Extinction spectra were collected from at least three samples to obtain average LSPR wavelength shift.

Characterization techniques: Transmission electron microscopy (TEM) micrographs were recorded on a JEM-2100F (JEOL) field emission instrument. Samples were prepared by drying a drop of the solution on a carbon-coated grid, which had been previously made hydrophilic by glow discharge. Scanning electron microscope (SEM) images were obtained using a FEI Nova 2300 Field Emission SEM at an accelerating voltage of 10 kV. Shimadzu UV-1800 spectrophotometer was employed for collecting UV-vis extinction spectra from solution and substrates

2.4 Results and Discussion

One of the primary hypotheses behind this work is that AuNCs exhibit significantly higher refractive index sensitivity (RIS) compared to gold nanorods (AuNRs) (~200 nm per RIU) and gold nanospheres (40-60 nm per RIU), which enables to lower the limit of detection (LOD) of the target biomarkers.[99, 100] While there have been some previous reports that demonstrate significantly higher refractive index sensitivity of Au nanostars and nanobipyramids, the synthesis of these nanostructures with tight control over shape is challenging.[100] The polydispersity in the shape of these nanostructures results in broad LSPR bands, which severely deteriorates the figure of merit (FOM = refractive index sensitivity/full width at half maximum (FWHM)) of these nanostructures, lowering the detection sensitivity.

AuNCs were obtained by galvanic replacement of Ag nanocubes with gold using $HAuCl_4$. Ag nanocubes were synthesized according to previously reported sulfide-mediated polyol synthesis method.[95] The AuNCs, which exhibited a LSPR wavelength of 783 nm, had an outer edge length of 57±4 nm and a wall thickness of 7±0.9 nm (Fig. 2.1). TEM images clearly reveal the hollow nanostructures with porous sidewalls and an average pore size of about 3 nm. The refractive index sensitivity of AuNCs was found to be 327.3 nm per RIU, which is ~58 % higher

than that of the longitudinal plasmon band of AuNRs (~207 nm per RIU) (Figure S1.3). The relatively narrow extinction band of AuNCs (FWHM of ~ 120 nm) results in a FOM of ~2.7. Electromagnetic (EM) decay length of AuNCs, another important parameter to maximize a LSPR transducer response, was calculated to be ~10.0 nm by fitting the experimental data of LSPR shift using a previously reported exponential equation, which is ~22 % smaller compared to that of AuNRs suggesting the higher local sensitivity in the vicinity of AuNCs surface (see ESI). The high sensitivity of AuNCs is possibly due to the strong electromagnetic fields resulting from the coupling between the external and internal surface plasmon fields in the hollow structures.[93] These results clearly indicate AuNCs to be an excellent choice for LSPR biosensors.

Considering the high refractive index sensitivity of AuNCs, we perform molecular-imprinting on AuNCs to realize highly sensitive plasmonic biosensor for neutrophil gelatinase-associated lipocalin (NGAL), a potential biomarker for acute kidney injury (Figure 2.2A).[101] p-Aminothiophenol (p-ATP) and glutaraldehyde (GA) were employed as crosslinkers to immobilize biomolecule templates on AuNCs surface by forming reversible imine bonds. Following the immobilization of templates, organo-siloxane monomers trimethoxypropylsilane (TMPS) and (3-aminopropyl) trimethoxysilane (APTMS), which are hydrolytically unstable, were copolymerized on template-bound AuNCs. While the Si-C bond and aminopropyl group cannot be cleaved, the methoxy groups of APTMS and TMPS undergo rapid hydrolysis to produce ethanol, methanol and trisilanols. The subsequent condensation of the transient silanols yields a functional amorphous polymer with amine ($-NH_3^+$), hydroxyl (-OH) and methyl ($-CH_3$) functional groups, serving as artificial antibodies. This is of great importance as the concerted weak interactions, namely electrostatic, hydrogen bonding and hydrophobic interactions, are

believed to be the most dominant form of interaction between artificial antibodies and template/target biomolecules.[102] The composition ratio of the siloxane co-polymerization has been adjusted to obtain the best trade-off between template release and mechanical strength.[103] The templates are finally removed by breaking the imine bonds with the crosslinkers using a mixture of oxalic acid and sodium dodecyl sulfate. Finally, the artificial antibodies engineered on the surface of AuNCs are ready for selective binding of the target biomolecules, even in the presence of interfering proteins in physiological fluids.

AuNCs also serve as transducers to monitor each step in molecular imprinting process, including attachment of crosslinkers, immobilization of template proteins, polymerization of organo-siloxane monomers, removal of templates, and rebinding of the target proteins. Extinction spectra of the AuNCs were collected following each step of the imprinting process: pristine AuNCs (step 1), forming a p-ATP/GA crosslinker layer (step 2), immobilization of template proteins (step 3), polymerization of organo-siloxane monomers (step 4), removal of templates (step 5), capture of target proteins (step 6), release of target proteins, (step 7) and its recapture (step 8) (Fig. 2.2B and C). The spectra revealed a progressive red-shift in LSPR wavelength with the deposition of each layer (*i.e.*, from steps 2 to 4) due to the increase in the refractive index (from buffer to the mixture of polymer layer and buffer). Figure 2.2C also shows two cycles of release and capture of target proteins, resulting in blue and red LSPR wavelength shift, respectively, demonstrating the reusability of molecularly imprinted AuNCs.

Figure 2.3A shows the shift in the LSPR wavelength of AuNCs upon exposure to different concentrations of NGAL in artificial urine, which covers the physiological and pathological concentration range. A monotonic increase in the LSPR shift is observed with increasing concentrations of NGAL in artificial urine. Nominally, patients with urine NGAL concentration

of 125 ng/ml or less do not progress to acute kidney injury (AKI), while patients with urine NGAL concentration of 350 ng/ml progress to AKI.[104, 105] The LSPR shift is about 5 nm for 125 ng/ml (5 nM) of NGAL, which is the critical concentration to differentiate if patients progress to AKI. We could easily detect NGAL down to 25 ng/ml (LSPR shift ~2 nm), which is much lower than the concentration range of NGAL in urine of patients with AKI. To test the selectivity of artificial antibodies, the NGAL-imprinted AuNCs were challenged with high concentrations of other urinary proteins as potentially interfering molecules, including 10 μg/ml of myoglobin (Mw=17.7 kDa), hemopexin (Mw=57 kDa), α_1-antitrypsin (Mw=52 kDa), α_1-acid glycoprotein (Mw=40.8 kDa), albumin (Mw=66.5 kDa), and hemoglobins (Mw=64.5 kDa) , and 1 μg/ml of recombinant human fatty acid-binding protein 1 (FABP1)(MW=14.2 kDa), and recombinant human fatty acid binding protein-3 (FABP3)(MW=14.8 kDa). The LSPR shift from all interfering proteins at significantly higher concentration (1-2 orders magnitude) is less than 1 nm, which is much smaller compared to ~5 nm for NGAL (Fig. 2.3B).

The pH value of human urine can range from 4.5 to 8.5 depending on diet or other pathological conditions of subjects. LSPR shift of molecularly imprinted AuNC upon exposure to artificial urine at different pH (4.5 - 8.5) spiked with 230 ng/ml of NGAL exhibited only a small variation indicating the remarkable pH stability of artificial antibodies (Fig. 2.3C). We also tested the plasmonic sensor response to 230 ng/ml of NGAL in urine of different specific gravities (1.005 to 1.030 g/ml). The LSPR shift exhibited a remarkable stability over the range of specific gravities tested, suggesting the excellent stability of the artificial antibodies (Fig. 2.3D). These results clearly suggest the robustness and efficiency of NGAL imprinted AuNCs as plasmonic nanotransducers with built-in recognition elements for the detection of target biomarkers under complex physiological conditions.

2.5 Conclusions

In conclusion, AuNCs, a novel class of hollow and porous nanostructures, exhibit significantly higher refractive index sensitivity and lower EM decay length, both of which make it an excellent candidate for plasmonic biosensing. AuNCs with built-in artificial antibodies achieved by molecular imprinting approach enabled the detection of a kidney injury biomarker (NGAL) down to a concentration of 25 ng/ml. The limit of detection (LOD) achieved with AuNCs as nanotransducers is more than an order of magnitude lower compared to that obtained with AuNRs. In addition to the excellent sensitivity, AuNCs with built-in artificial antibodies for NGAL exhibit excellent selectivity against numerous interfering urinary proteins and remarkable stability across pH ranging from 4.5 to 8.5 and specific gravities from 1.005 to 1.030. AuNCs with built-in artificial antibodies can be potentially employed for rapid urinalysis in point-of-care settings for identifying patients that can progress to AKI, allowing early therapeutic intervention.

2.6 Supporting Information

Supporting Information for chapter 2 is provided in appendix 1.

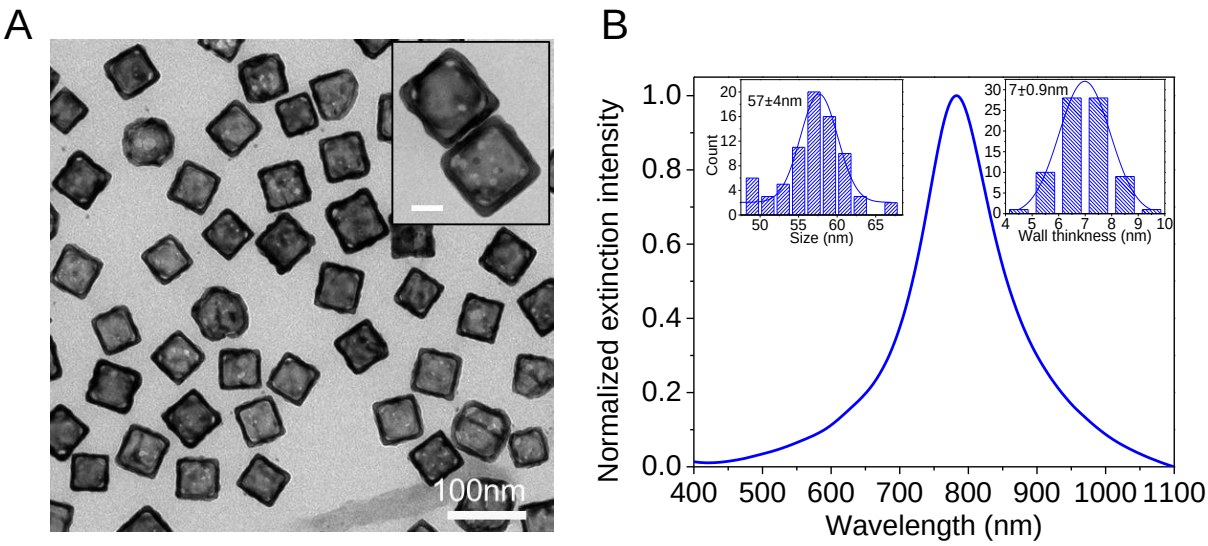

Figure 2. 1 (A) Representative TEM image of AuNCs (inset shows high magnification image). (B) Vis-NIR extinction spectrum of aqueous suspension of AuNCs (inset shows the histogram of side length and wall thickness of AuNCs obtained from TEM images).

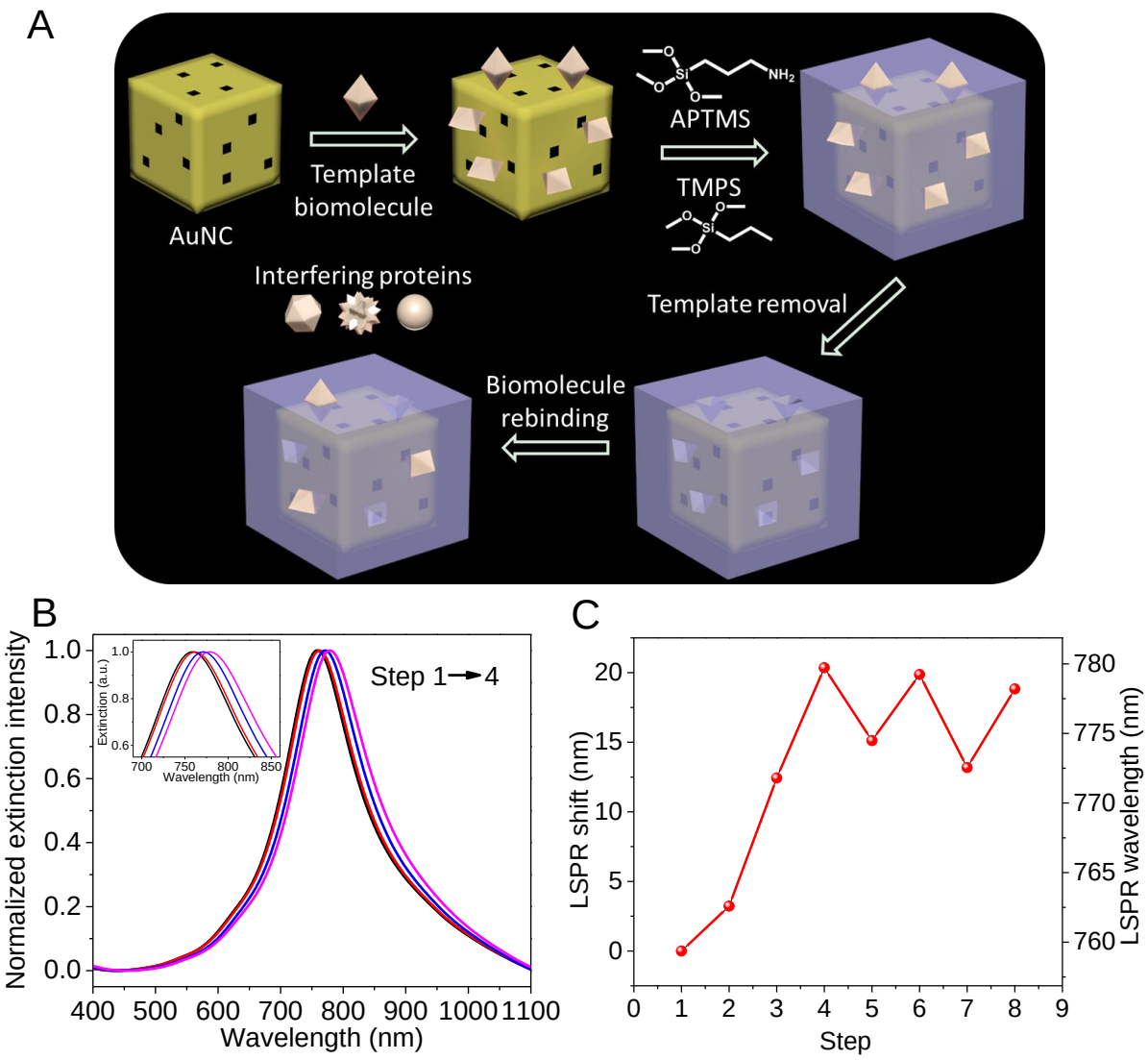

Figure 2. 2 (A) Schematic illustration representing the concept of molecular imprinting on AuNC. (B) Extinction spectra of AuNCs following each step in molecular imprinting process. (C) LSPR wavelength corresponding to each step in MIP, including two cycles of protein release and capture. The concentration of NGAL is 230 ng/ml.

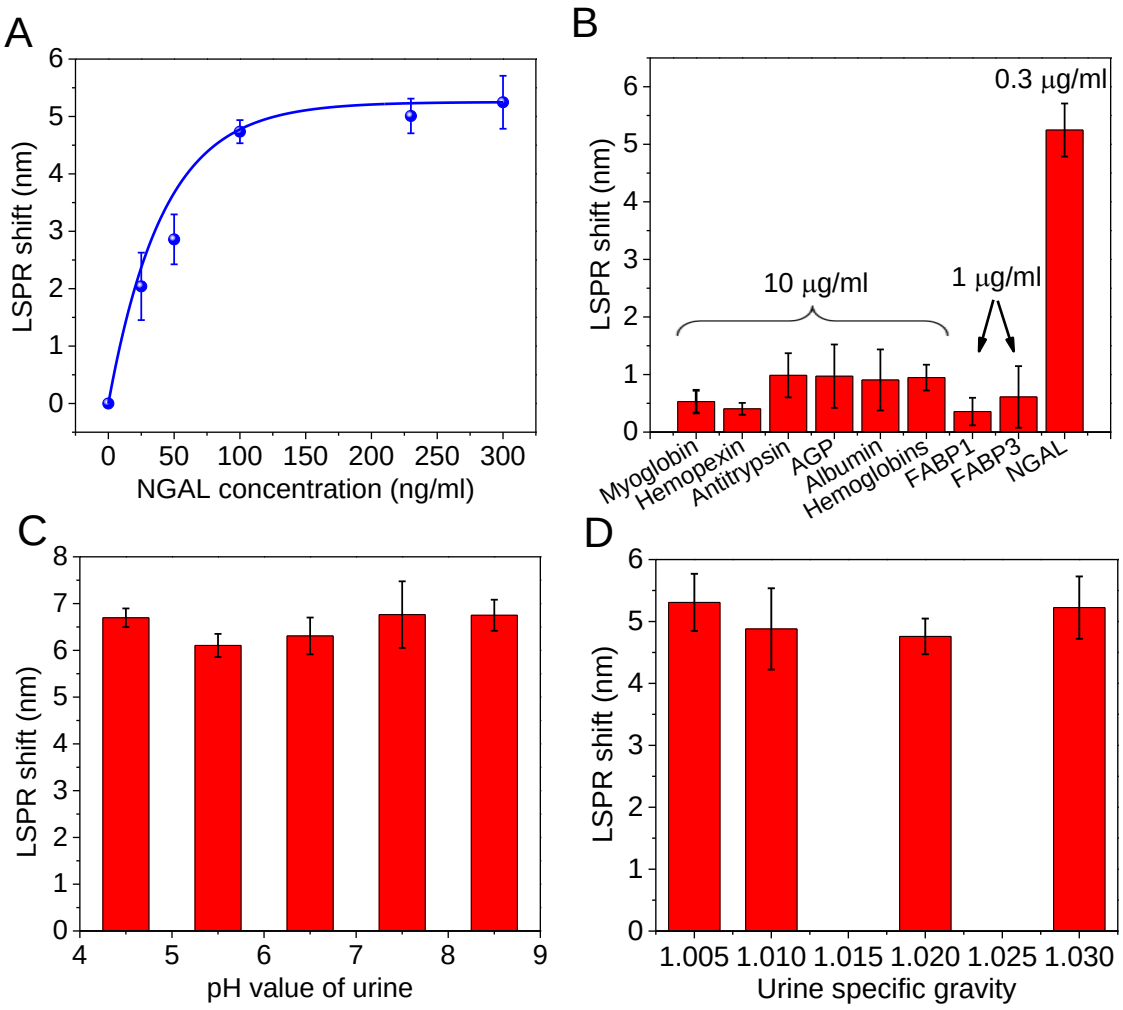

Figure 2. 3 (A) Sensitivity of NGAL imprinted AuNCs as plasmon transducers expressed by LSPR shift in nm as a function of NGAL concentration. (B) LSPR shift of interfering proteins (>10 μg/ml) compared with NGAL (0.3 μg/ml). (C) LSPR shift from 230 ng/ml of NGAL in artificial urine of different pH. (D) LSPR shift from 230 ng/ml of NGAL in artificial urine of different specific gravities.

Chapter 3: Size-dependent Surface Enhanced Raman Scattering Activity of Plasmonic Nanorattles

The results reported in this chapter were published in Chemistry of Materials, 2015, 27, 5261-5270. Reproduced with permission from American Chemical Society.

3.1 Abstract

Surface enhanced Raman scattering (SERS) is considered to be a highly attractive platform for chemical and biological sensing and molecular bioimaging. Most of the SERS substrates and contrast agents rely on individual or lightly aggregated metal nanostructures that either offer limited enhancement or suffer from poor stability and reproducibility. We have recently demonstrated that plasmonic nanorattles, owing to the internal electromagnetic hotspots, offer significantly higher SERS enhancement compared to their solid counterparts. In this work, we investigate the size- and shape-dependent SERS activity of plasmonic nanorattles comprised of Au nanospheres and nanorods as cores and porous Au nanocubes and cuboids as shells. The SERS activity of Au nanorattles with spherical core was found to increase with increase in the edge length of the cubic shell. On the other hand, the SERS activity of Au cuboid nanorattles with AuNR core was found to decrease with increase in the size of the cuboid shell. Finite difference time domain electromagnetic simulations show excellent agreement with our experimental results. Comprehensive understanding of the size- and shape-dependent SERS activity of this novel class of nanostructures can lead to the rational design and fabrication of highly efficient SERS substrates for chemical and biological sensing and ultrabright contrast agents for SERS-based molecular bioimaging.

3.2 Introduction

Surface enhanced Raman scattering (SERS) involves the large enhancement of Raman scattering from molecules adsorbed on or in close proximity to nanostructured metal surface.[106,107] SERS is considered to be a highly promising platform for trace chemical and biological detection, environmental monitoring, forensics and molecular bioimaging.[108,109,16,110,26,111,112,113-115] Various chemical methods such as seed-mediated and polyol synthesis that have enabled manufacture of size- and shape-controlled plasmonic nanostructures with precise control over optical properties have greatly helped in gaining a deeper understanding of the mechanistic aspects of SERS and its progress towards real-world applications.[108,109,16,116,35,117] Over the past two decades, numerous SERS substrates from roughened metal films to highly ordered nanostructure assemblies have been extensively investigated.[15]

Nanoscale gaps between adjacent plasmonic nanostructures exhibit extraordinarily large enhancement of electromagnetic field, which are often termed as electromagnetic hotspots. These electromagnetic hotspots, typically produced by nanostructure assemblies or aggregates, result in large SERS enhancement.[15,118,61,119] Extensive efforts have been dedicated to the design and fabrication of SERS substrates that exhibit both high enhancement and high reproducibility, which are critical for real-world application of SERS.[15, 114, 115, 120] SERS activity of assemblies of nanostructures is highly heterogeneous as the subtle intrinsic asymmetries of the assemblies leads to a dramatic (orders of magnitude) change in the maximum electromagnetic field enhancement.[121,122] It is a great challenge to realize uniform and reproducible SERS substrates with high density of electromagnetic hot spots based on such conventional plasmonic assemblies.[123,118] Furthermore, stringent control of nanostructure assemblies involves either complex chemical methods or expensive and time-consuming lithographic

techniques.[20,64,65,124,125] Therefore, nanostructures with inherent electromagnetic hot spots can serve as ideal SERS substrates for sensitive detection of analytes, which eliminate the need for nanoparticle assemblies or aggregates.[68]

Hollow and porous metal nanostructures are a relatively novel class of plasmonic nanostructures that exhibit extraordinary optical and catalytic properties compared to their solid counterparts, due to increased surface area and facile tunability of localized surface plasmon resonance (LSPR) wavelength over a broad range (visible to parts of near infrared).[126] These nanostructures have been employed as exogenous contrast agents in bioimaging and photothermal therapy, drug carriers, nanotransducers in chemical and biological sensing, and catalysts.[55-58, 127, 128] Among the various reported synthesis methods, galvanic replacement reaction serves as simple method for producing bi- and tri-metallic hollow nanostructures with well-controlled morphologies, composed of Ag and Au, Pd, or Pt.[129, 130] We have recently demonstrated that Au nanorattles comprised of Au nanooctahedron as core and porous gold cube as shell offer significantly higher SERS enhancement compared to other solid nanostructures of similar size (e.g., Au nanocubes).[128] Electromagnetic hotspots within the nanostructures, which are critical for large SERS enhancement, preclude the need for controlled aggregation or assembly of nanostructures. While the preliminary study demonstrates the high SERS activity of the nanostructures, a systematic study of size-dependent SERS activity of plasmonic nanorattles is still missing. In this work, we report the size-dependent SERS activity of plasmonic nanorattles comprised of Au nanosphere or nanorod core and porous Au cubic or cuboid shell. Seed-mediated synthesis in combination with galvanic replacement reaction was employed to realize nanorattles of different sizes. The SERS activity of the nanostructures was probed using 2-napthalenthiol as a model analyte. In the case of cubic nanorattles with a relatively small spherical core, the SERS activity

was found to increase with increase in the edge length of the nanorattles. On the other hand, for nanorattles with Au nanorod core, the SERS activity was found to decrease with increase in the size of cuboid shell.

3.3 Experimental Section

Materials

Gold chloride ($HAuCl_4$), Hexadecyltrimethylammonium bromide (CTAB), sodium borohydride ($NaBH_4$), silver nitrate ($AgNO_3$), ascorbic acid, poly(vinyl pyrrolidone) (PVP, MW=29,000 g/mol), and 2-naphthalenethiol (2-NT) were purchased from Sigma-Aldrich. Hexadecyltrimethylammonium chloride (CTAC) was purchased from Tokyo Chemical Industry (TCI). All the chemicals were used as received without further purification.

Synthesis of Au Nanospheres

CTAC-capped Au nanospheres were synthesized by using a seed-mediated method according to a previous report with slight modifications.[64,131] Au seeds were synthesized by adding 0.6 ml of ice-cold sodium borohydride solution (10 mM) into a solution containing 0.25 ml $HAuCl_4$ (10 mM) and 9.75 ml CTAB (0.1 M) under vigorous stirring at room temperature. The color of seed solution changed from yellow to brown. Seed solution was kept undisturbed at room temperature for 3 h. Growth solution was prepared by mixing 6 ml of $HAuCl_4$ (0.5 mM) and 6 ml of CTAC (0.2 M) under stirring followed by the addition of 4.5 ml of ascorbic acid (0.1 M). Subsequently, 0.3 ml of Au seed solution was added to the growth solution. Au nanospheres were centrifuged and redispersed in nanopure water for further use.

Synthesis of AuNS@Ag nanocubes

For the synthesis of AuNS@Ag core-shell nanocubes with different sizes, different volumes of Au nanospheres (0.15, 0.2, 0.5, 1.0, 2.0, and 3.0 ml) and 20 mM CTAC (4.85, 4.8, 4.5, 4.0, 3.0 and 2.0 ml) were mixed under stirring at 60 °C for 20 min. Subsequently, 5 ml of $AgNO_3$ (2 mM) and 5 ml aqueous solution of 50 mM ascorbic acid in 40 mM CTAC were added under stirring at 60 °C for 4 h. After 4 h, the as-synthesized AuNS@Ag nanocubes solution was cooled by immersing the reaction vial in ice-cold water. The AuNS@Ag nanocube solution was centrifuged and the nanostructures were redispersed in nanopure water for further use.

Synthesis of Au Nanorattles with AuNS cores

Au nanorattles were synthesized by transforming silver shell of AuNS@Ag nanocubes into a porous Au shell via galvanic replacement reaction. The as synthesized AuNS@Ag nanocubes were centrifuged (13,000 rpm for 15 min) and redispersed into a 15 ml aqueous solution comprised of 7.5 ml PVP (1 wt%) and 7.5 ml CTAC (0.2 M) solutions. The solution was heated at 90 °C for 5 min under magnetic stirring. Subsequently, $HAuCl_4$ aqueous solution (0.5 mM) was injected into the AuNS@Ag nanocube solution at a rate of 0.5 ml/min under magnetic stirring until the solution turned to blue color. The Au nanorattles solution were centrifuged at 13,000 rpm for 15 min and dispersed in nanopure water.

Synthesis of Au nanorods

Au nanorods were synthesized by using seed-mediated method.[132,133] Seed solution was synthesized by adding 0.6 ml of an ice-cold $NaBH_4$ (10 mM) solution into 10 ml of $HAuCl_4$ (0.25 mM) and CTAB (0.1 M) solution under vigorous stirring at room temperature. The color of the seed solution changed from yellow to brown. Growth solution was prepared by mixing 5 ml

$HAuCl_4$ (10 mM), 95 ml CTAB (0.1 M), 1 ml $AgNO_3$ (10 mM) and 0.55 ml ascorbic acid (0.1 M), consecutively. The solution was homogenized by gentle stirring. To the colorless solution, 0.12 ml of freshly prepared seed solution was added and kept undisturbed in the dark for 14h. Prior to use, the AuNR solution was centrifuged twice at 8000 rpm for 10 min to remove excess CTAB and redispersed in nanopure water.

Synthesis of AuNR@Ag nanocuboids

2 ml twice-centrifuged AuNR and 4 ml CTAC (20 mM) were mixed at 60 °C under stirring for 20 min. 5 ml $AgNO_3$ (2 mM), 2.5 ml CTAC (80 mM) and 2.5 ml ascorbic acid (0.1 M) were added under stirring at 60 °C for 4 h. Subsequently, the as synthesized AuNR@Ag nanocuboids solution was cooled by immersing the reaction vial in ice-cold water.

Synthesis of Au nanorattles with AuNR cores

Au nanorattles were synthesized by transforming Ag shell of AuNR@Ag nanocuboids into porous shell of Au via galvanic replacement reaction. The as synthesized AuNR@Ag nanocuboids were centrifuged and redispersed in CTAC solution (50 mM), followed by heating at 90 °C for 5 min under magnetic stirring. $HAuCl_4$ aqueous solution (0.5 mM) was injected into the AuNR@Ag solution at a rate of 0.5 ml/min under magnetic stirring.

Spectroscopy Measurements

SERS spectra measurements were preformed by adding 10 µl of 2-NT (100 mM in ethanol) to 90 µl of Au nanorattles. The concentration of cubic nanorattles was estimated to be 1.41×10^{13}/ml (see SI for details). The concentration of cuboidal nanorattles was estimated to be 3.44×10^{12}/ml

(see SI for details). SERS Spectra were collected using a Renishaw inVia confocal Raman spectrometer. Spectra were collected using the 785 nm laser, which was focused on the sample using a 20X objective with 30 sec exposure time. The laser power was measured to be approximately 0.7 mW. Five spectra were collected from different spots across each sample. UV-Vis extinction spectra were collected using Shimadzu UV-1800 UV-Vis spectrophotometer.

Microscopy Characterization

Transmission electron microscopy (TEM) images were collected using a JEOL JEM-2100F field emission microscopy. Scanning electron microscopy (SEM) images were obtained using a FEI Nova 2300 Field Emission SEM at an accelerating voltage of 5 kV.

Finite-difference time-domain (FDTD) simulations

Electromagnetic field distribution around the plasmonic nanorattles with different sizes was simulated by using three-dimensional finite-difference time-domain (FDTD) with a commercially available software (EM Explorer). FDTD simulations exploit the time and position dependence of Maxwell's equations to model the electromagnetic waves in rectangular 3D cells (Yee cells) of a finite volume. A Yee cell size of 0.15 μm is used in the current study, which is about 1/4th of the wavelength. Perfectly Matched Layer (PML) absorbing boundary conditions were applied in all directions of the simulation domain. For cubic nanorattles, the AuNS core was defined as a sphere with a diameter of 8 nm and the edge length of hollow Au shells was defined to be 20, 23, 32, 37, 40, 45 nm and the wall thickness to be 4 nm. The simulation domain was defined to be 150 nm × 150 nm × 150 nm. Dimension of Au nanorattles with AuNR cores was 69.5x 37.9 nm, 74.1x 44.6 nm, 78.9x 50.0 nm and 83.1x 55.2 nm and with a wall

thickness of 5 nm and AuNR (core) with a diameter of 11.3 nm and a length of 51.9 nm were simulated in a 150 nm × 150 nm × 150 nm domain. A high resolution simulation was run at the excitation (λ=785 nm) and Stokes-shifted wavelength (λ= 880 nm) using p-polarized (along the longitudinal direction of the anisotropic Au nanostructure) to obtain the electromagnetic field distribution. The complex refractive index of gold was set to n=0.18 + i4.96 at this frequency, the refractive index of surrounding medium was set to be 1.33 as water.

3.4 Results and Discussion

Figure 3.1A schematically illustrates a two-step process employed in the synthesis of Au nanorattles. The synthesis of plasmonic nanorattles starts with synthesis of Au nanospheres (AuNS), which serve as seeds for Ag coated Au nanospheres. AuNS are in turn synthesized using a seed-mediated method (see experimental section for details).[134] Transmission electron microscopy (TEM) images reveal the narrow size distribution of AuNS with a diameter of 8.5±0.6 nm (Figure 3.1B). Vis-NIR extinction spectrum of AuNS depicts the LSPR wavelength at 521 nm (Figure 3.1C).

AuNS@Ag nanocubes are synthesized by a seed-mediated method using AuNS as seeds, according to a recently reported procedure with slight modification.[131] The growth solution is comprised of silver nitrate ($AgNO_3$) as silver precursor, ascorbic acid as reducing agent and cetyltrimethylammonium chloride (CTAC) as capping agent. Different volumes of AuNS were added to the growth solution to vary the thickness of Ag shell on the surface of AuNS. TEM images reveal uniform size and shape of the Au@Ag nanocubes with varying edge lengths obtained by varying the amount of AuNS (seed) added to the Ag growth solution (Figure 3.2A-F). The AuNS cores were found to be at the center of each Au@Ag nanocube suggesting the

uniform overgrowth of Ag on the surface of the AuNS. The AuNS@Ag nanocubes are dominated (100) facets due to the faster growth of Ag on the (111) facets of cuboctahedral Au nanoparticles.[131] The Ag shell thickness on AuNS and the edge length of resultant Au@Ag nanocubes monotonically decreased with increasing volume of the AuNS added to the growth solution (Figure 3.2G). The seed-mediated method employed here enables facile control over the dimensions of the core-shell nanostructures by simply varying the amount of seed solution added to the growth solution. This is in contrast with the seedless polyol synthesis approach, which requires careful monitoring and quenching of the growth reaction to obtain Ag nanocubes of desired dimensions.[135] Extinction spectra of the Au@Ag nanocubes with different edge lengths reveal a progressive red shift in the dipolar LSPR wavelength with increase in the edge length (Figure 3.2H). The increase in the LSPR wavelength with edge length of the nanocubes was found to be linear over the size range investigated here, which is in agreement with previous reports (Figure 3.2I).[131,135]

As noted above, the galvanic replacement reaction is a powerful and facile method to achieve hollow plasmonic nanostructures.[129,130] Galvanic replacement reaction is an electrochemical reaction which involves the oxidation of one metal with lower reduction potential (which serves as a sacrificial template) by the ions of another metal with higher reduction potential.[59] We employed the galvanic replacement reaction to synthesize Au nanorattles comprised of AuNS cores and porous Au shell. Addition of $HAuCl_4$ to the Ag nanocube solution results in a spontaneous galvanic replacement reaction.[136,137] Galvanic replacement reactions performed on Au@Ag nanocubes with edge lengths of 38 ± 1.6, 33 ± 1.3, 30 ± 1.9, 26 ± 1.4, 20 ± 1.0 and 17 ± 1.2 nm resulted in Au nanorattles with edge lengths of 45 ± 2.2, 40 ± 1.8, 37 ± 1.6, 32 ± 1.4, 23 ±

1.1 and 20 ± 0.6 nm, respectively (Figure 3.3A-F). The increase in the edge length of Au nanorattles compared to the corresponding Au@Ag nanocubes is due to the Au deposition on the external wall of Ag nanocube template during the galvanic replacement reaction. The wall thickness of the Au nanorattles was measured to be around 4 nm from the TEM images (Figure 3.3A-F). AuNS embedded within porous Au shell can be seen in the magnified TEM images of individual Au nanorattles (shown as insets in Figure 3.3A-F). The galvanic replacement reaction employed here involves the titration of $HAuCl_4$ into Au@Ag nanocubes solution. With the addition of $HAuCl_4$ into Au@Ag nanocubes solution, the LSPR band corresponding to Ag nanocubes decreased in intensity with a concomitant rise of a new LSPR band at higher wavelength. The higher wavelength band corresponding to the dipolar LSPR of porous Au shells progressively red shifts with increase in the amount of $HAuCl_4$ titrated into the Au@Ag nanocubes solution.[131,135,59] The titration of Au precursor into the Au@Ag nanocubes of different edge lengths was controlled to obtain Au nanorattles with similar dipolar plasmon resonance wavelength, around 680 nm (Figure 3.3H). For Au nanorattles obtained using the smallest Au@Ag nanocubes (edge length of 17 nm), the maximum LSPR wavelength that could be achieved with galvanic replacement was around 620 nm. Further addition of $HAuCl_4$ into Au@Ag nanocubes solution resulted in a blue shift possibly due to the blocking of pores on the shell, which results in continuous Au deposition on the external wall without oxidizing more Ag.[138,139]

For the synthesis of Au cuboid nanorattles, we used Au nanorods as cores. Figure 3.4A schematically illustrates the two-step process involved in the synthesis of Au cuboid nanorattles. In the first step, seed-mediated method was employed to synthesize AuNR. The length and

diameter of AuNRs were respectively measured to be 51.9 ± 4.2 and 11.3 ± 1.1 nm using TEM (Figure 3.4B). The extinction spectrum of AuNR cores exhibited two characteristic bands at 508 and 822 nm corresponding to the transverse and longitudinal plasmon resonances, respectively (Figure 3.4C).[140]

The uniform growth of Ag shell on AuNRs resulted in rectangular prismatic structures with truncated rectangular/square cross sections (Figure 3.5A-D). The thickness of the Ag shell can be finely tuned by controlling the seed concentration (i.e. AuNR concentration) with respect to the Ag precursor concentration in the shell growth solution. Au@Ag nanocuboids with longitudinal and transverse edge lengths of 62.7×31.2 nm, 67.0×37.0 nm, 70.4×41.8 nm and 72.5×44.7 nm were obtained by varying the Ag precursor concentration (Figure 3.5A-D). The longitudinal and transverse edge lengths increased linearly with increase in the Ag precursor concentration in the solution (Figure 3.5E). The thickness of Ag shell at AuNR ends and sides increased linearly with increase in the Ag precursor concentration in the solution (Figure S2.1). The Ag shell on the sides of the AuNR was found to be thicker than that at the ends. This anisotropic Ag shell formation results in a decrease in the aspect ratio of AuNR@Ag nanocuboids with the increase in the Ag precursor concentration, which is in agreement with previous reports.[141,142] Following the deposition of a thin layer of Ag on AuNRs, the bimetallic nanostructures exhibited four bands in the extinction spectrum (Figure 3.5F). We define these bands as peaks 1 to 4 from higher wavelength to lower wavelength. The extinction bands 1 and 2 correspond to the longitudinal and transverse dipolar resonances and the extinction bands 3 and 4 correspond to the transverse octupolar resonances of the AuNR@Ag nanocuboids.[141,142,143,144] Progressive blue shift in the longitudinal dipolar resonance is observed with increasing

concentration of Ag precursor, which can be ascribed to the reduction of aspect ratio of the Au@Ag nanocuboids. It has been demonstrated that the longitudinal dipolar resonance of the Au@Ag nanocuboids is highly sensitive to the aspect ratio of the AuNRs employed as cores and the optical properties can be finely tuned with by controlling the aspect ratio of AuNRs and the Ag shell thickness.[141, 142] The octupolar resonances remain largely insensitive to the structural changes of Au@Ag nanocuboids.

Similar to Au@Ag nanocubes, galvanic replacement reaction was employed to convert Au@Ag nanocuboids into anisotropic nanorattles comprised of AuNR core and porous cuboid shell. Au cuboid nanorattles with four different dimensions (69.5×37.9 nm, 74.1×44.6 nm, 78.9×50.0 nm and 83.1×55.2 nm) were obtained using Au@Ag nanocuboid templates described above (Figure 3.6A-D). The length and width of Au cuboid nanorattles increased linearly with the increase in the dimensions of Au@Ag nanocuboid templates (Figure 3.6E). Vis-NIR extinction spectra reveal that the formation of Au cuboid nanorattle from Au@Ag nanocuboids is associated with the gradual lowering in the intensity of plasmonic extinction bands corresponding to Ag and the appearance of a higher wavelength band that progressively red-shifts with addition of $HAuCl_4$. During the galvanic replacement reaction, the titration of $HAuCl_4$ into the Au@Ag nanocuboid solution was controlled to achieve a LSPR band at ~650 nm for Au cuboid nanorattles of different dimensions (Figure 3.6F).

Now we turn our attention to the SERS activity of the size-controlled Au nanorattles. To compare the SERS activity of the nanorattles, we employed 2-napthalnethiol (2-NT) as a model analyte, which readily chemisorbs on Au surface.[145] To compare the SERS activity of the Au

nanorattles of different sizes, the concentration of the Au nanorattles was maintained constant. SERS spectra obtained from Au nanorattles of different sizes display most prominent Raman bands at 1066, 1381 and 1625 cm^{-1}, which correspond to the C-H bend and ring stretch vibrations of 2-NT, respectively (Figure 3.7A).[146] We have employed the most intense band at 1381 cm^{-1} to compare the SERS intensity of Au nanorattles. Within the size range tested here, the SERS activity was found to increase with increase in the size of the Au nanorattles (Figure 3.7A, B). We observed a similar trend for both 785 and 514.5 nm excitation sources (see SI, Figure S2.3 for SERS data corresponding to 514.5 nm excitation). The increase in SERS activity with increasing size of the nanorattles was found to be highly non-linear. A rapid increase in the SERS activity was noted as the size of the nanorattles increased from 37 nm to 40 and 45 nm (Figure 3.7B). The increase in the SERS activity of the Au nanorattle can be ascribed to the increase in the extinction corssection and total surface area of these hollow nanostructures with increase in the size. Using discrete dipole approximation (DDA), it has been demonstrated that the extinction crosssection of Au nanocage with 50 nm edge length is more than four times higher than that of Au nanocage with 30 nm edge length.[147] The higher extinction (and scattering) crossection of larger Au nanorattles efficiently lends itself for higher SERS activity observed here. The SERS enhancement factors of Au nanorattles with size of 45, 40, 37, 32, 23 and 20 nm is estimated to be 2.91×10^{8}, 1.91×10^{8}, 2.66×10^{7}, $2.24\times10^{7,}$ 2.30×10^{7}, 2.13×10^{7}, respectively (see SI for details).[55, 148,149]

Three-dimensional finite-difference time-domain (FDTD) simulations were employed to understand the electromagnetic field intensity distibution and SERS enhancement from the plasmanic nanorattles. The spatial maps of electrical field intensity (at 785 nm) around the Au

nanorattles with water as surrounding medium are shown in Figure 3.7C. It is known that the average SERS intensity (I_{SERS}) is proportional to square of the product of the gain in the incident and Raman scattered light.[148] For low frequency Raman modes, the gains of the incident and Raman scattered light can be considered to be nearly equal. This results in the SERS intensity to scale with the fourth power of the gain in the electromagnetic field caused by the nanostructure.[148] For 785 nm excitation, the Stokes-shifted wavelength corresponding to 1381 cm^{-1} Raman band is calculated to be at ~880 nm. We have plotted square of the product of the gain in the incident and Raman scattered light of electric field enhancement ($|E_{785}|^2|E_{880}|^2$) obtained from FDTD simulations, which represents the average SERS intenstiy from the plasmonic nanorattles (Figure 3.7D). The SERS intensity trend obtained from FDTD simulations shows remarkable agreement with our experimental observations (Figure 3.7B, D). Except for the smallest nanorattles tested here, the $|E_{785}|^2|E_{880}|^2$ of plasmonic nanorattles increased with the increase in the edge length of the nanorattles. Nanorattles with an edge length of 23 nm exhibited slightly lower $|E_{785}|^2|E_{880}|^2$ compared to that with 20 nm, which is a deviation from the overall trend of increasing $|E_{785}|^2|E_{880}|^2$ with increase in edge length. This deviation can be understood by considering the two electromagnetic hot regions of the nanorattles. The electromagnetic field enhancement at the internal hotspot formed between the nanosphere (core) and the sidewall (porous shell) increases with the decrese in the edge length of the nanorattles. On the other hand, the field enhancement at the corners of this cubic nanorattles increases with the increase in the edge length of the nanorattles. For nanorattles with edge length of 20 nm, the internal electromagnetic hotspot results in higher $|E_{785}|^2|E_{880}|^2$ compared to the nanorattles with an edge length of 23 nm. With subsequent increase in the size of the Au

nanorattles, a progressive increase in the electromagnetic field intensity was noted. The increase in $|E_{785}|^2|E_{880}|^2$ with the size of the nanorattles exhibited a highly non-linear trend. In excellent agreement with the experimental data a significant increase in $|E_{785}|^2|E_{880}|^2$ was noted as the edge length of the nanorattle increased from 37 nm to 40 nm and to 45 nm (Figure 3.7D).

The SERS activity of the size-controlled Au cuboid nanorattles was measured using the same method described above. The SERS intensity of Au cuboid nanorattles was found to be significantly higher compared to that of Au nanorattles with spherical core (Figure 3.7A and Figure 3.8A). As opposed to Au nanorattles with spherical nanoparticle core, the SERS activity of Au cuboid nanorattles was found to decrease with increase in the size of the Au nanorattles (Figure 3.8A, B). SERS enhancement factors of Au cuboid nanorattles with dimensions of 69.5x37.9 nm 74.1x44.6 nm, 78.9x50.0 nm, 83.1x55.2 nm is 1.17×10^9, 3.21×10^8, 1.47×10^8, 6.59×10^7, respectively (see SI for details). The FDTD simulations were employed to understand the spatial distribution of electrical field intensity around the Au cuboid nanorattles (Figure 3.8C). The electromagnetic field intensity map shows electromagnetic hotspots between the core AuNR and the porous cuboid shell. As the dimensions of porous Au cuboid shell are increased while maintaining the dimensions of AuNR constant, we note a progressive decrease in the electromagnetic field intensity (Figure 3.8C). Rapid decrease in $|E_{785}|^2|E_{880}|^2$ with increase in the size of nanorattles is in agreement with our experimental observations (Figure 3.8B and 3.8D). In the case of nanorattles with spherical core, the influence of the core is rather minimal and the SERS activity is governed by the dimensions of the cubic shell. On other the hand, in the case of cuboid nanorattles, the SERS activity is determined by the electromagentic field intensity of the internal hotspot (gap between the porous shell and AuNR) rather than the size-

dependent extinction coefficient of the nanostructures. Increase in the size of the porous shell leads to a decrease in the electromagnetic field at the hotspot and resultant decrease in the SERS intensity.

3.5 Conclusions

In conclusion, we performed a systematic study of SERS activity of size-controlled Au nanorattles obtained by galvanic replacement of size-controlled AuNS@Ag nanocubes and AuNR@Ag nanocuboids. Within the size range studied here, the SERS activity of the plasmonic nanorattles with spherical cores increased with the increase in the edge length. The increase in the SERS activity of the cubic nanorattles is due the increase in the extinction (and scattering) coefficient of nanostructures with size. On the other hand, the SERS activity of the plasmonic nanorattles with nanorod cores decreased with the increase in the edge length of the porous cuboid shells. In the case of the cuboid nanorattles, the electromagnetic hotspot within the nanostructure, formed between the edge of the AuNR and porous Au shell, governs the SERS activity. FDTD simulations showed excellent agreement with the experimentally determined size-dependent SERS activity of the nanorattles. Highly reproducible and facile synthesis combined with excellent SERS activity makes Au nanorattles an attractive candidate for the fabrication of uniform and highly efficient SERS substrates and molecular bioimaging.

3.6 Supporting Information

Supporting Information for chapter 3 is provided in appendix 2.

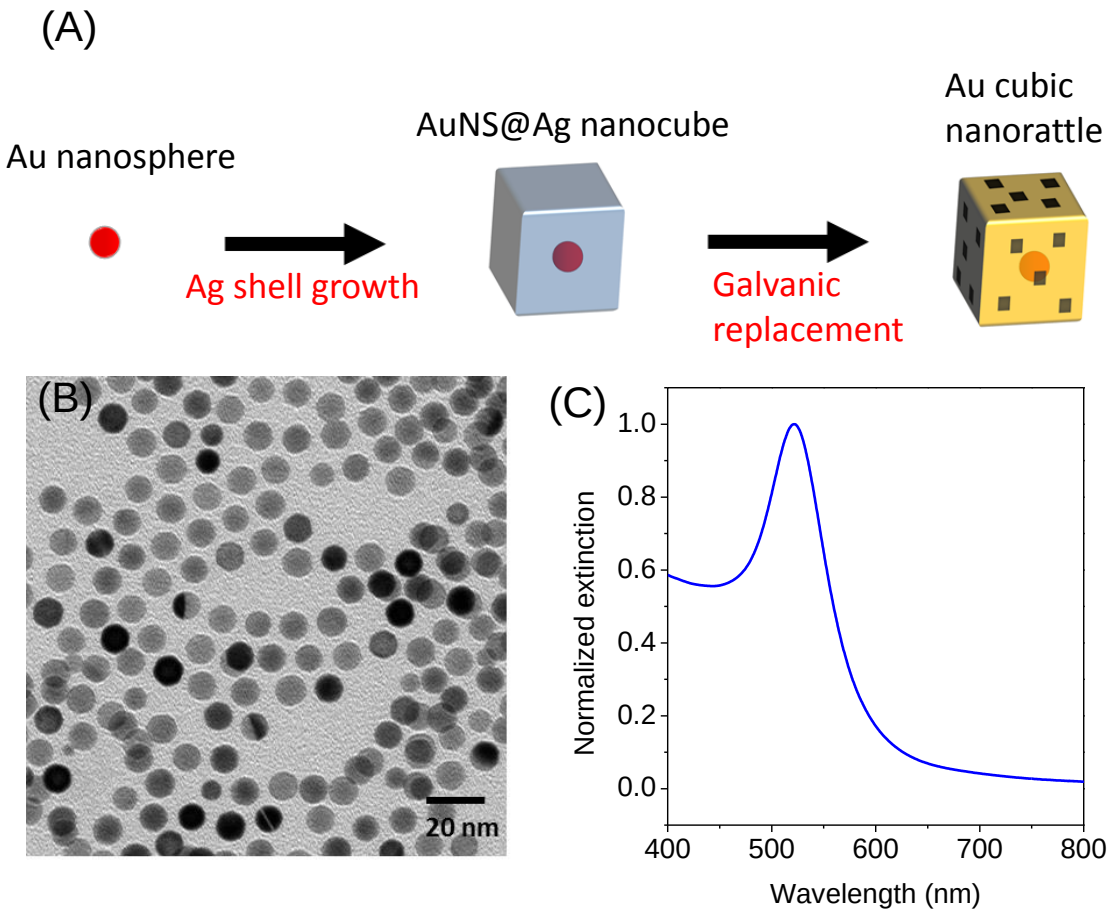

Figure 3. 1 (A) Schematic illustration of the synthesis of Au nanorattle using Au nanosphere as core. (B) TEM image of AuNS employed as cores for the synthesis of Au nanorattles. (C) Vis-NIR extinction spectrum of AuNS.

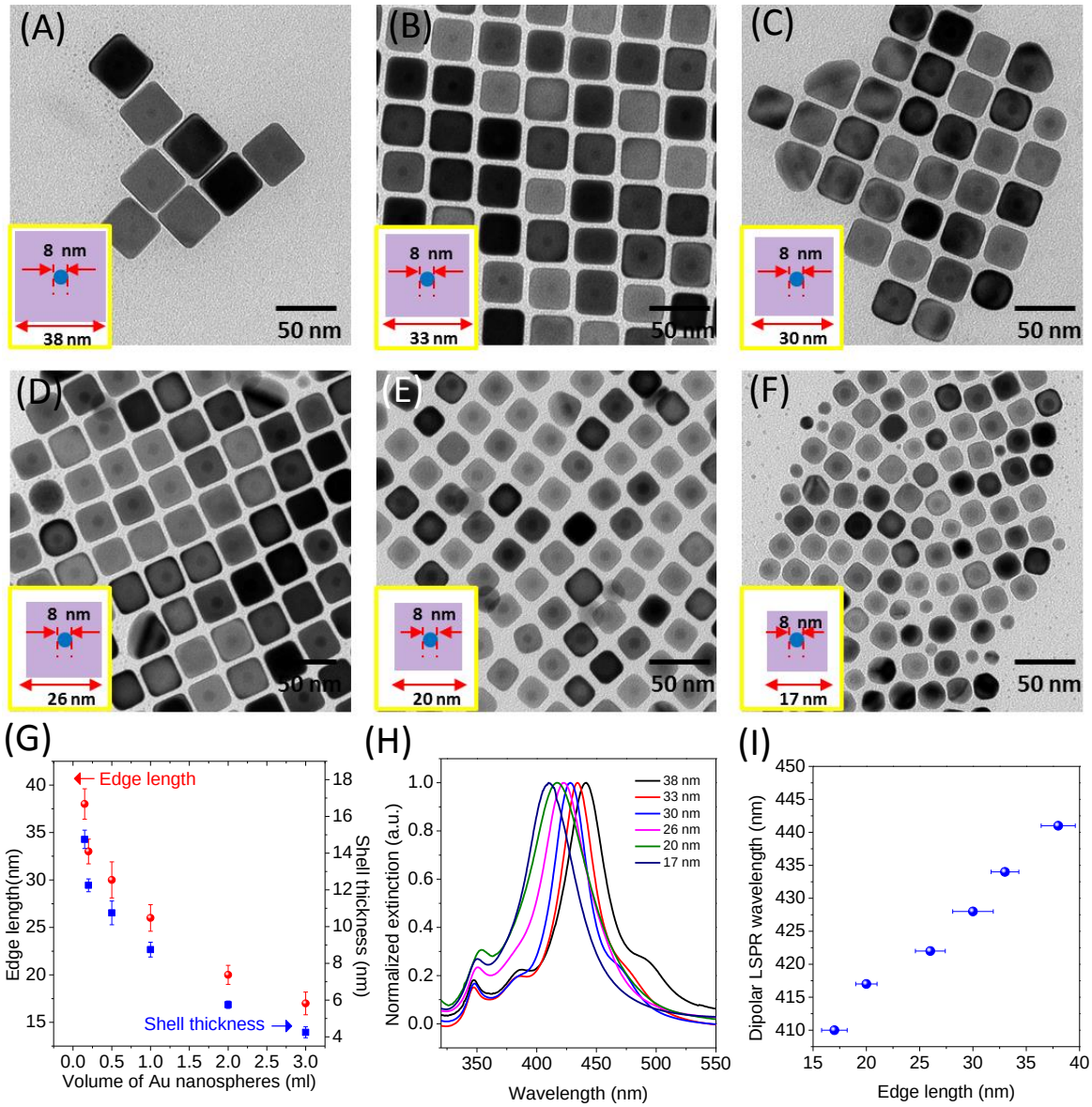

Figure 3. 2 (A)-(F) TEM images of AuNS@Ag nanocubes obtained by adding (A) 0.15 ml, (B) 0.2 ml, (C) 0.5 ml, (D) 1.0 ml, (E) 2.0 ml, (F) 3.0 ml of AuNS into Ag shell growth solution. Inset of (A)-(F) shows schematic illustration of AuNS@Ag nanocube (not to scale). (G) Plot depicting the variation in the edge length and Ag shell thickness of AuNS@Ag nanocube with the volume of AuNS added to the Ag growth solution. (H) Vis-NIR extinction spectra of AuNS@Ag nanocubes with different edge lengths indicated in the plot. (I) Plot depicting the

linear increase in the dipolar LSPR wavelength of AuNS@Ag nanocubes with increase in the edge length.

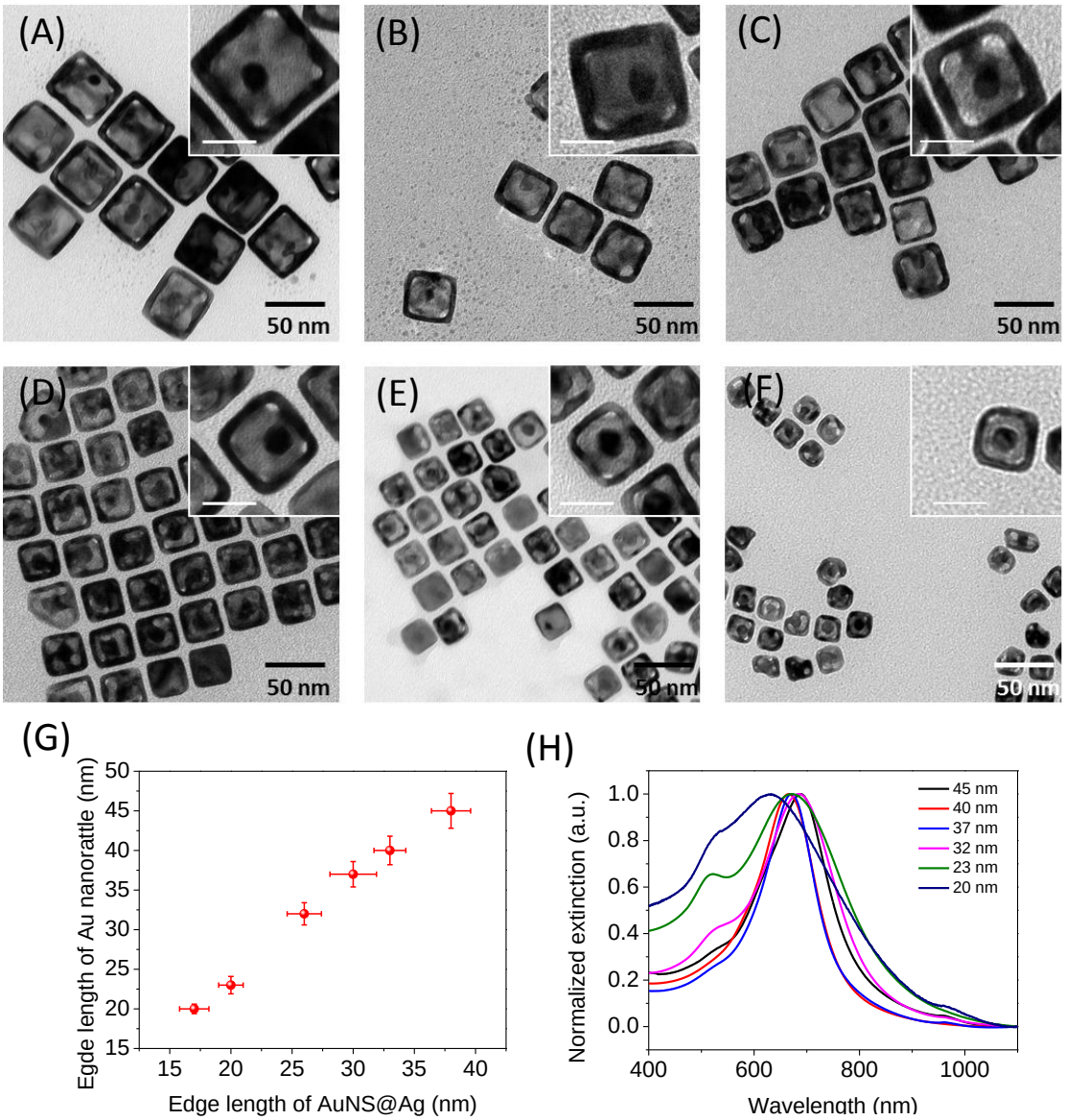

Figure 3. 3 (A)-(F) TEM images of Au nanorattles with edge length of (A) 45±2.2 nm (B) 40±1.8 nm (C) 37±1.6 nm (D) 32±1.4 nm (E) 23±1.1 nm, and (F) 20±0.6 nm obtained by galvanic replacement of AuNS@Au nanocubes. Insets show magnified images of a single Au nanorattles (scale bar in the insets represent 20 nm) (G) Plot showing the linear increase in the edge length of Au nanorattles with increase in the edge length of AuNS@Ag templates. (H) Vis-NIR extinction spectra of Au nanorattles of different sizes indicated in the plot.

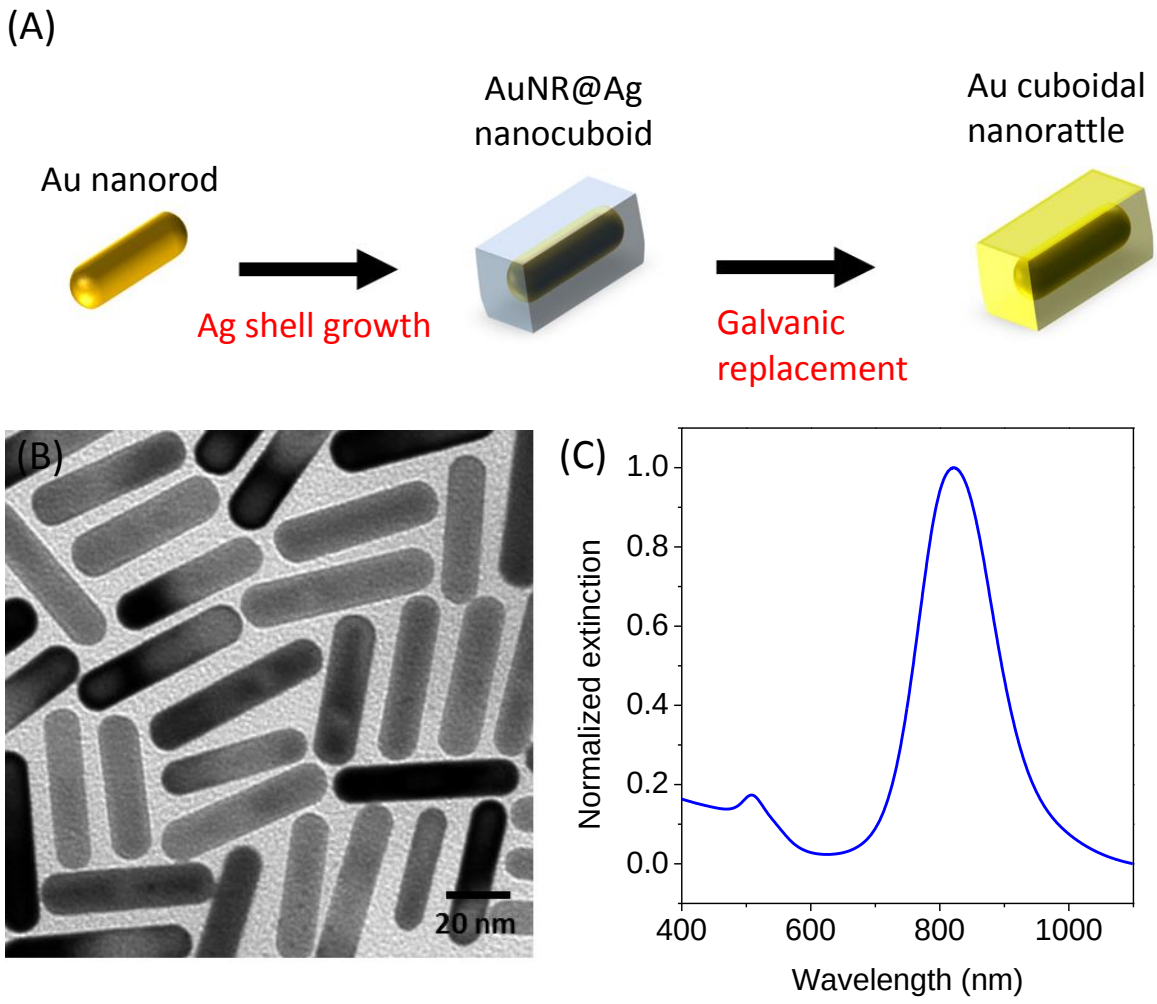

Figure 3. 4 (A) Schematic illustration of the synthesis of Au nanorattle using Au nanorod as core. (B) TEM image of AuNRs. (C) Vis-NIR extinction spectrum of AuNRs.

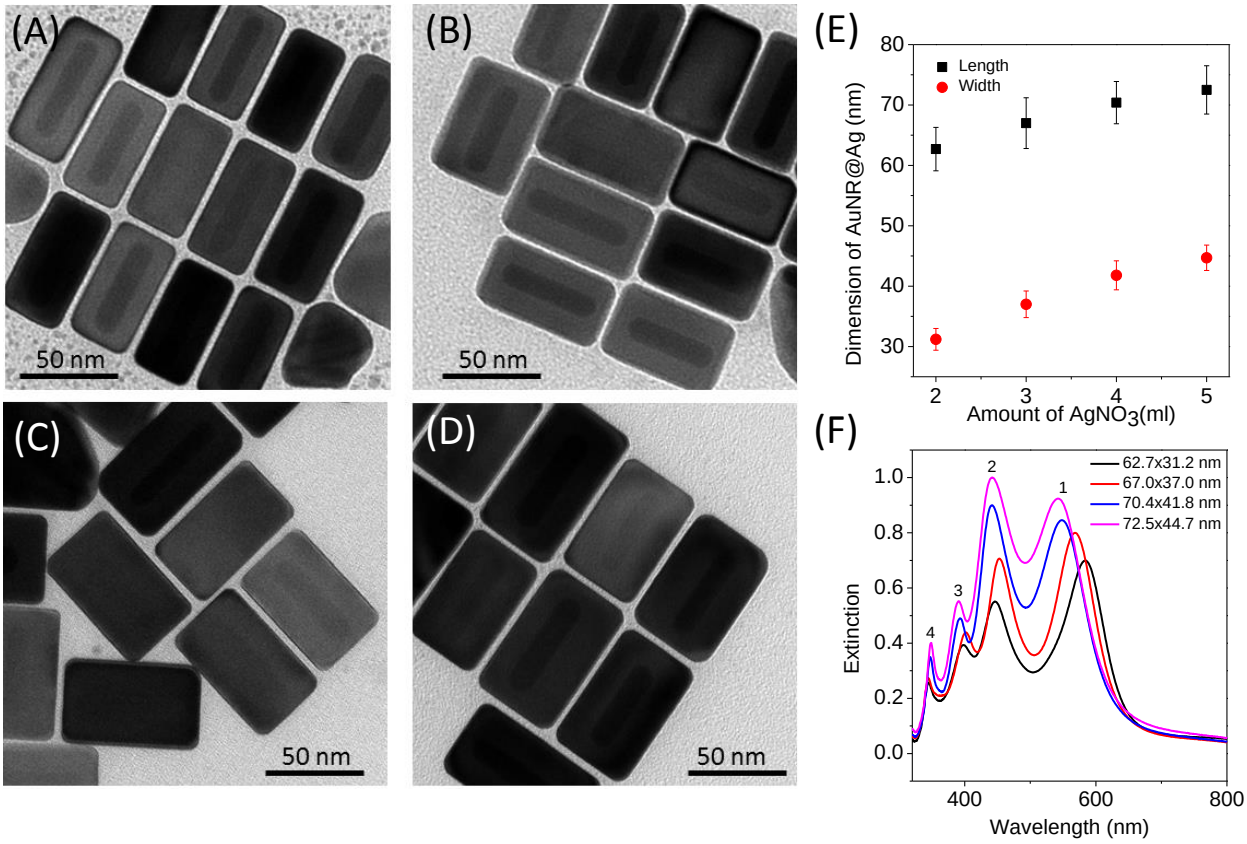

Figure 3. 5 TEM images of AuNR@Ag nanocuboids (A) 62.7×31.2 nm, (B) 67.0×37.0 nm, (C) 70.4×41.8 nm and (D) 72.5×44.7 nm. (E) Plot depicting the length and width of AuNR@Ag cuboids achieved by different amount of $AgNO_3$ in the shell growth solution. (F) Vis-NIR extinction spectra of AuNR@Ag nanocuboids of different dimensions indicated in the plot.

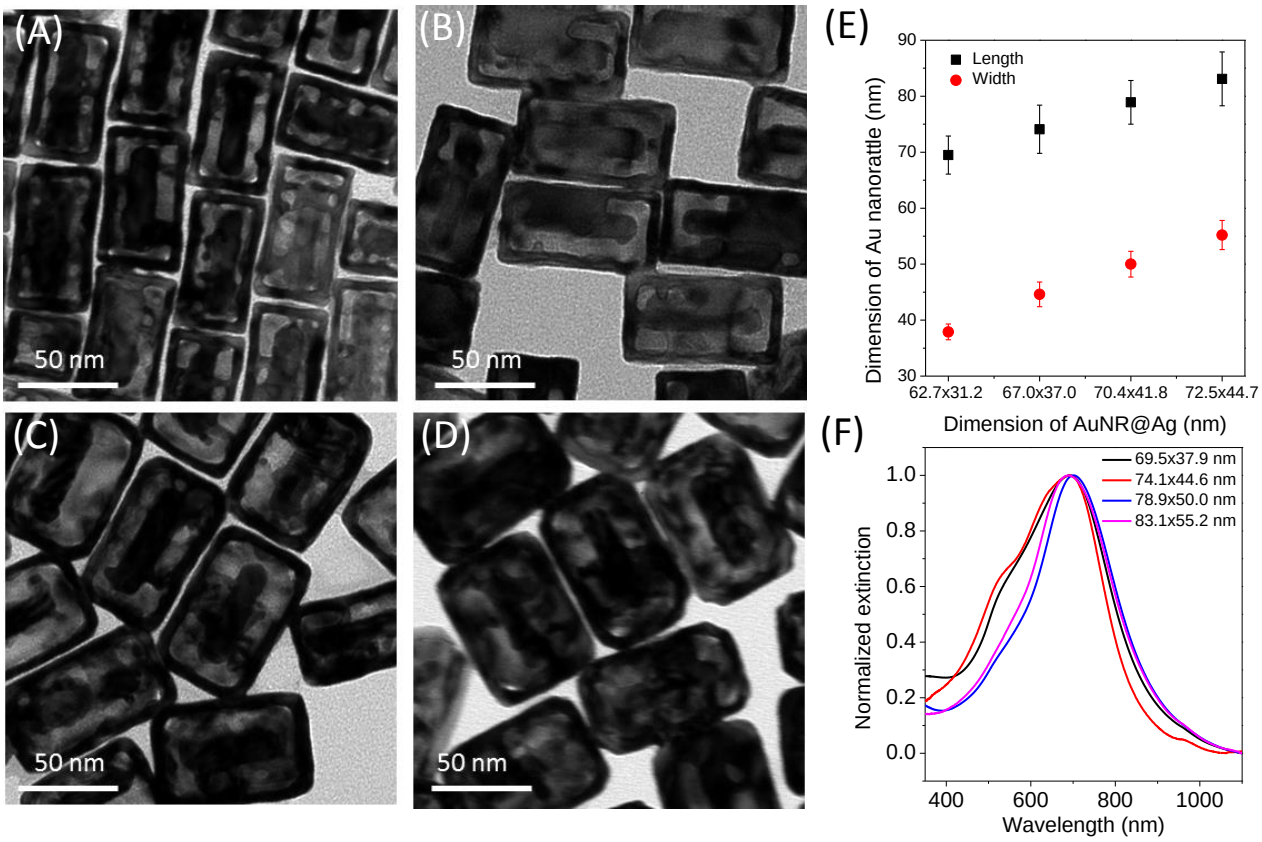

Figure 3. 6 TEM images of Au cuboid nanorattles with dimensions of (A) 69.5×37.9 nm (B) 74.1×44.6 nm, (C) 78.9×50.0 nm and (D) 83.1×55.2 nm obtained by galvanic replacement of AuNR@Au nanocuboids. (E) Plot showing the linear increase in the dimensions of Au cuboid nanorattles with increase in the dimensions of AuNR@Ag nanocuboid templates. (F) Vis-NIR extinction spectra of Au nanorattles of different dimensions indicated in the plot.

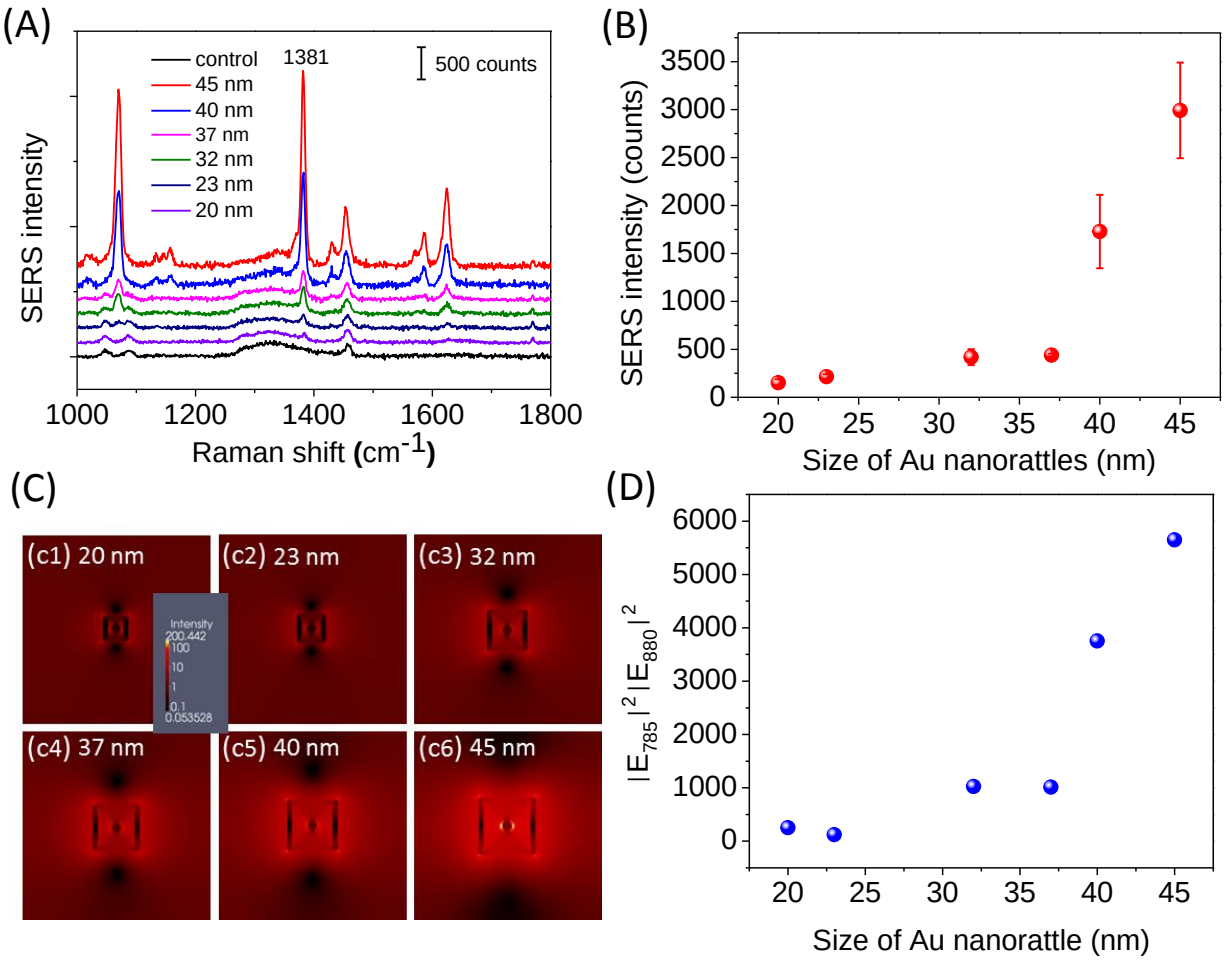

Figure 3. 7 (A) SERS spectra obtained from Au nanorattles of different edge lengths following the adsorption of 2-NT. (B) Plot showing the non-linear increase in the SERS intensity of 1381 cm^{-1} Raman band with increase in the edge length of Au nanorattles. (C) FDTD simulations showing the electric field distribution of Au nanorattles of different sizes using 785 nm excitation wavelength (c1-c6 correspond to electric field distribution of Au nanorattles with edge length of 20, 23, 32, 37, 40 and 45 nm, respectively). (D) Plot showing the non-linear increase in $|E_{785}|^2|E_{880}|^2$ with increase in the edge length of Au nanorattles.

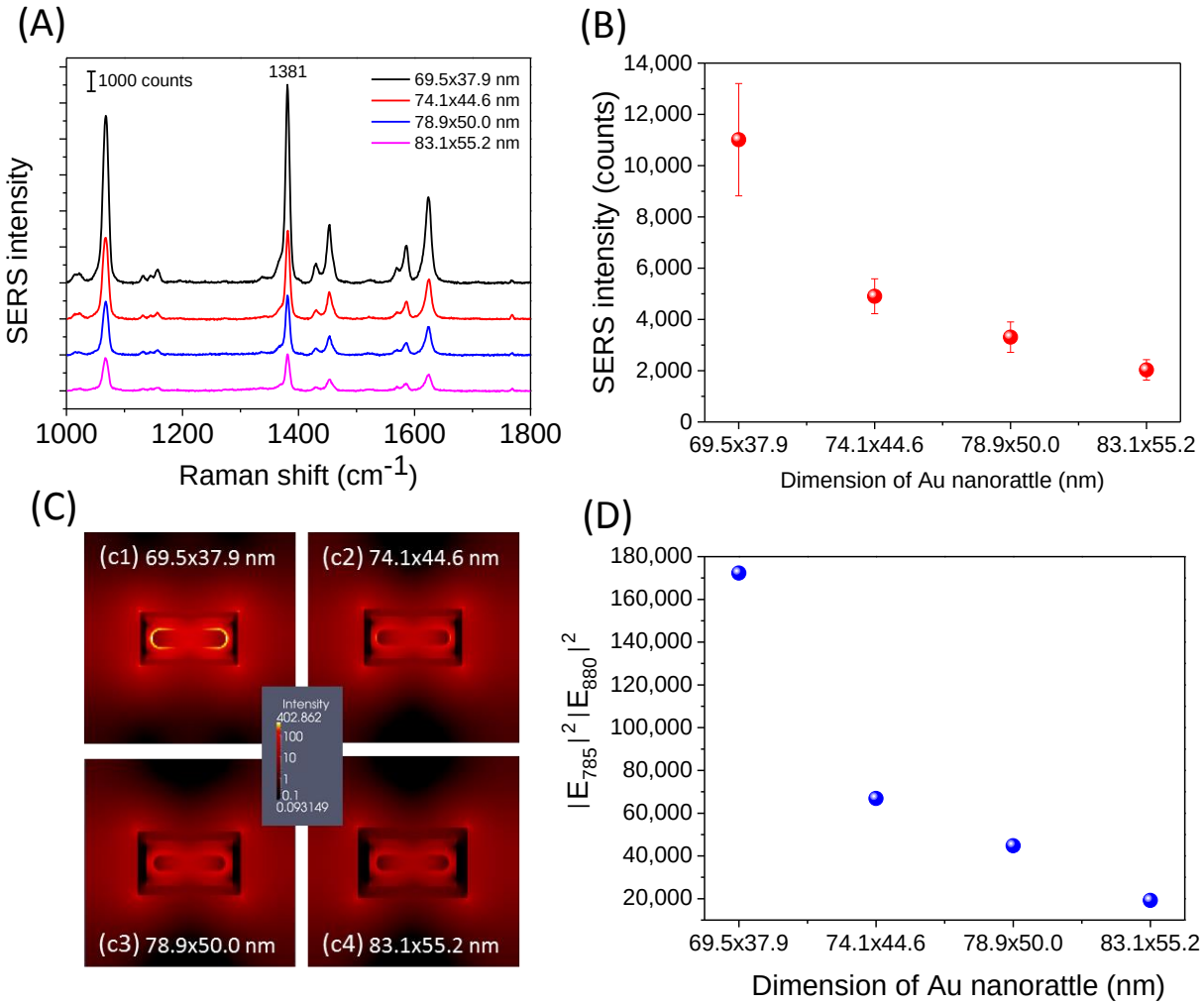

Figure 3. 8 (A) SERS spectra obtained from Au cuboid nanorattles of different dimensions following the adsorption of 2-NT. (B) Plot showing the progressive decrease in the SERS intensity of 1381 cm^{-1} Raman band with increase in the dimensions of Au cuboid nanorattles. (C) FDTD simulations showing the electric field distribution of Au cuboid nanorattles of different sizes (c1-c4 correspond to electric field distribution of Au nanorattles with dimensions 69.5×37.9 nm, 74.1×44.6 nm, 78.9×50.0 nm and 83.1×55.2 nm, respectively using 785 nm excitation wavelength. (D) Plot showing the progressive decrease in $|E_{785}|^2|E_{880}|^2$ with increase in the edge length of Au cuboid nanorattles.

Chapter 4: Polarization-dependent Surface Enhanced Raman Scattering Activity of Anisotropic Plasmonic Nanorattles

The results reported in this chapter were published in The Journal of Physical Chemistry C, 2016, 120, 16899-16906. Reproduced with permission from American Chemical Society.

4.1 Abstract

Plasmonic nanorattles comprised of solid plasmonic core and porous and hollow plasmonic shell are a novel class of nanostructures that are highly attractive for surface enhanced Raman scattering (SERS)-based chemical and biological sensing and bioimaging. In this report, we demonstrate the polarization-dependent SERS activity of cuboidal plasmonic nanorattles comprised of a solid gold nanorod core and porous and hollow cuboidal shell. Plasmonic coupling between the gold nanorod core and porous and hollow cuboidal shell of the nanorattles results in a large electromagnetic (EM) enhancement at the interior of the nanorattles. Owing to the presence of internal electromagnetic hotspots, the polarization dependence of the plasmonic nanorattles was found to be markedly different compared to that of solid AuNR@Ag nanocuboids. Similar to most conventional anisotropic solid nanostructures, the AuNR@Ag nanocuboids exhibited a polarization-dependent SERS activity that is dominated by the sharp corners and edges. Conversely, the internal electromagnetic hotspot formed between the AuNR and porous shell of cuboidal nanorattle dominates the SERS activity of the anisotropic nanorattles. The results further our understanding of the SERS activity of this promising class of

hollow nanostructures with internal electromagnetic hotspots and provide guidelines for the design of highly efficient SERS substrates based on these nanostructures.

4.2 Introduction

Surface enhanced Raman scattering (SERS), which involves the large enhancement of Raman scattering from molecules adsorbed on or in close proximity to the surface of metal nanostructures, is considered to be highly promising for chemical and biological sensing, environmental monitoring, forensics and bioimaging.[106] Over the last decade, remarkable progress has been made in the synthesis of size- and shape-controlled plasmonic nanostructures with a significant fraction of them designed for SERS applications.[15] Assemblies of plasmonic nanostructures with nanoscale gaps, locations of electromagnetic hotspots, exhibit large enhancement of the electromagnetic field and are identified to be responsible for intense SERS, including single molecule SERS.[15, 26, 119, 150, 151] It has been demonstrated that the contribution of a relatively small number of electromagnetic hotspots (63 out of 10^6 active sites) can be quite significant (~25 %) in the overall SERS signal, underscoring the importance of electromagnetic hotspots in the design of SERS substrates and tags.[152] Despite significant efforts focusing on achieving controlled assembly of plasmonic nanostructures, scalable methods that yield nanoparticle assemblies with highly uniform, isotropic and stable SERS enhancement remains challenging. Therefore, it is highly desirable to design and synthesize plasmonic nanostructures with inherent electromagnetic hotspots, which eliminate the need for the assembled or lightly aggregated nanostructures.[68, 128, 153-155]

Porous or hollow metal nanostructures are attracting significant attention due to their unique optical properties such as tunable localized surface plasmon resonance (LSPR) throughout the visible and part of the near-infrared spectrum and the ability to hold and deliver cargo with an

external trigger such as light or ultrasound.[55] These nanostructures have been extensively investigated for various applications including imaging, therapy, and sensing.[156,157,158,58,159] Among the various synthetic methods, galvanic replacement reaction serves as an effective and versatile method to produce bi- or tri-metallic hollow nanostructures with the ability to control the size, shape, morphology, composition, porosity and surface functionality of the resulting nanostructures.[59, 160] Recently, we have demonstrated that plasmonic nanorattles comprised of Au core and porous Au-Ag shell provide significantly higher SERS enhancement owing to the electromagnetic hotspot formed between the core and shell.[128,161] The porous outer shell lends itself for facile diffusion of analytes into the electromagnetic hotspots within the nanostructures. Cuboidal nanorattles comprised of gold nanorod (AuNR) cores and porous cuboidal Ag-Au shells are a particularly promising class of nanostructures for SERS. We have recently demonstrated that the electromagnetic field between the core and shell exhibits a dramatic increase as the gap between the core and shell is reduced.[161]

SERS activity of any anisotropic nanostructure or assembly of nanostructures depends on the polarization of the excitation source with respect to the orientation of the nanostructure or assembly. Polarization-dependent SERS activity of various nanostructures, including Au nanopartices,[162,163] Ag nanocubes,[164] Ag nanobars and nanorice,[165] dimers,[166,167] and single and coupled nanowires has been reported.[168,169] To the best of our knowledge, polarization-dependent SERS activity of anisotropic nanorattles with internal electromagnetic hotspots has not been reported. In this work, we present the polarization-dependent SERS activity of an individual cuboidal plasmonic nanorattle and its solid counterpart *i.e.* Au@Ag nanocuboid. Significantly, the polarization-dependent SERS activity of solid nanocuboid was found to be markedly different from that of the cuboid nanorattle with the nanoantenna effect (*i.e.* enhanced

electromagnetic field at the sharp corners and edges of the nanostructure) dominating the former nanostructure and internal hotspots (*i.e.* enhanced electromagnetic field due to the coupling of AuNR core and porous shell) dominating the latter. Computational simulations based on the finite-difference time-domain (FDTD) method also corroborate our experimental findings.

4.3 Experimental Section

Materials

Gold chloride ($HAuCl_4$), sodium borohydride ($NaBH_4$), silver nitrate ($AgNO_3$), ascorbic acid, cetyltrimethylammonium bromide (CTAB) and 2-naphthalenethiol (2-NT) were purchased from Sigma Aldrich. Hexadecyltrimethylammonium chloride(CTAC) was purchased from Tokyo Chemical Industry(TCI). All the chemicals were used as received without further purification.

Synthesis of Au nanorods

Au nanorods were synthesized by using the seed-mediated method. Seed solution was synthesized by adding 0.6 ml of an ice-cold $NaBH_4$ (10 mM) solution into 0.25 ml of $HAuCl_4$ (10 mM) and 9.75 ml CTAB (0.1 M) solution under vigorous stirring at room temperature. The color of the seed solution changed from yellow to brown. The growth solution was prepared by mixing 5 ml $HAuCl_4$ (10 mM), 95 ml CTAB (0.1 M), 1 ml $AgNO_3$ (10 mM) and 0.55 ml ascorbic acid (0.1 M), consecutively. The solution was homogenized by gentle stirring until the solution became colorless. Then, 0.12 ml of freshly prepared seed solution was added to the colorless solution and kept undisturbed in the dark for 14 h. Prior to use, the AuNR solution was centrifuged twice at 8000 rpm for 10 min to remove excess CTAB and re-dispersed in Nanopure water.

Synthesis of AuNR@Ag nanocuboids

A 2 ml twice-centrifuged AuNR solution and 4 ml CTAC (20 mM) were mixed at 60 °C under stirring for 20 min. 5 ml $AgNO_3$ (2 mM), 2.5 ml CTAC (80 mM) and 2.5 ml ascorbic acid (0.1 M) were added under stirring at 60 °C for 4 h. Subsequently, the synthesized AuNR@Ag nanocuboid solution was cooled by immersing the reaction vial in ice-cold water.

Synthesis of Au nanorattles

Au nanorattles were synthesized by transforming the Ag shell of AuNR@Ag nanocuboids into a porous shell of Au using the galvanic replacement reaction. The synthesized AuNR@Ag nanocuboids were centrifuged (8000 rpm, 10 min) and redispersed in CTAC solution (50 mM), followed by heating at 90 °C for 5 min under magnetic stirring. An aqueous solution of $HAuCl_4$ (0.5 mM) was injected into the solution of AuNR@Ag nanocuboids at a rate of 0.5 ml/min under magnetic stirring until a blue colored solution appeared.

Characterization

Extinction spectra were collected using a Shimadzu UV-1800 UV-Vis spectrophotometer. Transmission electron microscopy (TEM) images were obtained on a JEOL JEM-2100F field emission instrument. Scanning electron microscopy (SEM) images were obtained on a FEI Nova NanoSEM 2300 at an acceleration voltage of 5 kV.

Dark-field scattering spectroscopy

Dark-field scattering spectroscopy was performed using an inverted optical microscope equipped with a dark-field condenser and a grating spectrometer. Samples were prepared as follows.

Cover slips and glass slides were cleaned by heating them in 2 M KOH for 30 min, followed by subsequent washing with deionized water, sodium bicarbonate solution, and Nanopure water. The cover slips and glass slides were sonicated twice in Nanopure water before use. The nanostructure solution was diluted 10-fold in water and drop-casted on the clean dry cover slip. The drop-casted sample was allowed to dry before incorporating the cover slip into a flow cell prepared by a method reported previously.[170] The flow cell was filled with water and mounted with the cover slip face down on the microscope stage. The flow cell was held in place using clips. A drop of oil was put on an Olympus UPlanApo 0.5-1.35 NA 100x oil immersion objective. The objective was raised to touch the bottom surface of the flow cell. Excessive oil was dropped on the top glass slide surface of the flow cell facing an Olympus U-DCW 1.2-1.4 NA oil immersion dark field condenser. The condenser was lowered and brought in contact with the oil. White light from Olympus U-LH100-3 100 W halogen lamp source, focused through the condenser, was used to illuminate the nanostructures. The scattered light was collected by the objective. The objective was focused with the smallest NA setting. Further, the condenser height as well as position were adjusted to get high signal-to-noise (S/N) ratio and wide field of view of the dark-field image. The size of the illumination aperture (placed above condenser) was also adjusted to get high S/N ratio of the image. Select emitters in the wide-field image were aligned with a spectrometer slit mounted on the exit port of the microscope. Dark-field scattering spectra were acquired using a Princeton Instruments Acton SP 2300 spectrograph set at 300 blaze grating and a PyLoN CCD. Typical spectral acquisition time was 10 s. The dark-field scattering spectra reported here are corrected for background and lamp spectrum using an inbuilt routine in the WinSpec software (by Princeton Instruments) that uses the following formula:

$$\text{Scattering spectrum} = (\text{Raw data} - \text{background}) / \text{lamp spectrum}. \quad (1)$$

Spectra were collected with the spectrograph centered at two different wavelengths, 540 and 660 nm. The spectra were merged to obtain spectra in the full range from 400 – 800 nm.

Discrete dipole approximation (DDA) simulations

The DDA method[171-173] was used for simulation of the optical spectra of the AuNR@Ag nanocuboids. The DDA method numerically solves Maxwell's equations for one or a series of arbitrarily shaped objects by discretizing each object into a cubic array of N polarizable point dipoles and self-consistently solving for the polarizability of each dipole interacting with the incident electromagnetic field and all other N-1 dipoles. The DDSCAT code (version 7.3) was implemented by use of the open source nanoDDSCAT+ tool (version 2.0x)[174] available on nanoHUB. The AuNR@Ag nanocuboid target with was generated using the Blender module within nanoDDSCAT+. The configuration of the target along with dimensions are shown in the inset of Figure S3.4. The corners of the target structure were appropriately beveled using options available in Blender. The generated target geometry, which had an effective radius of 37.4 nm, was then converted it into a cubic grid of virtual dipoles, the input for the DDA simulation. An inter-dipole spacing of 1 nm was employed.

Simulated spectra of AuNR@Ag nanocuboid were obtained in two different media. In the first case, the nanostructure was placed in a surrounding medium with a refractive index (R.I.) of 1.33, corresponding to water. In the second case, a medium of R.I. 1.56, corresponding to the placement of the nanostructure on an Si substrate in air, was used. The mixed medium RI in the latter case was calculated on the basis of the contact area between the NS and the surrounding medium. The area of the face of the nanostructure in contact with the Si substrate, was calculated to be ~ 4757 nm^2, the total external surface area of the nanostructure being ~25458 nm^2. The

fraction of area ϕ in contact with Si substrate was thus 0.19. The R.I. of air was taken to be 1 and that of Si was assumed to have a constant value of 4, the reported value at 580 nm in the middle of the visible region. The imaginary part of the R.I. for Si, which is small, was neglected. The mixed medium R.I. is estimated as:

$$eff.n = \varphi.n_{Si}^2 + (1-\varphi).n_{air}^2 \quad (2)$$

which yields a value of 1.96, which was used in the simulations. The bulk experimental dielectric functions of Au and Ag (available as a library option in nanoDDSCAT+) from Johnson and Christy[175] were utilized without any corrections. Extinction spectra (extinction efficiency vs. wavelength) in the 300-1000 nm wavelength range were obtained from each simulation. The nanostructure was excited with a plane wave traveling along the vertical direction (relative to the inset in Figure S3.4) and polarized either along the long axis or the short axis of the nanorod.[176, 177] Spectra simulated for each of these polarizations, where respectively longitudinal and the transverse LSPR modes of the nanorod can be observed, were added to obtain a "polarization-averaged" spectrum.

SERS spectra measurements

Polarization-dependent SERS spectra from an individual anisotropic nanostructure were collected using a Renishaw inVia confocal Raman spectrometer. Nanostructures deposited on a silicon substrate was exposed to 10 mM 2-NT solution in ethanol and rinsed with ethanol. The sample was mounted on a rotation stage and the specific nanostructures were identified using dark-field microscopy and spatially correlated to SEM images obtained before exposure to 2-NT solution. Spectra were collected using 785 nm laser excitation, which was focused on the sample using a 50x objective. A 60 s exposure time was set. The laser power was measured to be ~0.7

mW. For SERS spectra collected in aqueous medium, measurements were preformed by adding 10 µl of 2-NT (10 mM in ethanol) to 100 µl of the Au nanostructure solution. Raman spectra were collected using 514.5 nm and 785 nm laser excitation, focused on the sample using a 20X objective. A 30 s exposure time was used in this case.

Finite-difference time-domain (FDTD) simulations

Modeling of the electromagnetic field distribution around the AuNR@Ag nanocuboid and the Au nanorattle was performed using three-dimensional finite-difference time-domain (FDTD) method implemeted by the commercially available software, EM Explorer. The Au nanorattle structure was simulated with dimensions of 89.3 nm x 60.6 nm x 60.6 nm and a wall thickness of 6.5 nm. The AuNR@Ag nanocuboid was simulated with dimensions of 83.9 nm x 56.7 nm x 56.7 nm and corners truncated with spheres of 24 nm diameter. The AuNR core in both cases had a length of 49.9 nm and a diameter of 14.4 nm. The simulation domain was 150 nm × 150 nm × 150 nm. A high-resolution simulation was run at the extinction wavelength (λ = 785 nm) and the Stokes-shifted wavelength (λ = 880 nm corresponding to a Raman shift of ~1380 cm^{-1}) using an incident plane wave linearly polarized at various angles with respect to the long-axis direction of the anisotropic nanostructure. The complex refractive index of Au was set to n = 0.18 + i4.96 and 0.21+i5.88, corresponding to the values for bulk Au at 785 nm and 880 nm, respectively. The refractive index of surrounding medium was set to a value of 1.00 for air. The field intensities for both 785 nm and 880 nm excitation ($|E_{785}|^2$ and $|E_{880}|^2$) were determined.

4.4 Results and Discussion

Anisotropic plasmonic nanorattles were synthesized using a two-step method involving the formation of a thin Ag shell on Au nanorods (AuNRs) followed by a galvanic replacement

reaction (Figure 4.1). Galvanic replacement reaction performed by the addition of a Au precursor, i.e., $HAuCl_4$, to a solution of AuNR@Ag nanocuboids results in the transformation of the Ag shell into a hollow and porous Ag-Au shell.[161] Plasmon coupling between the core (AuNR) and the cuboidal Ag-Au shell results in internal electromagnetic hotspots, which are accessible to the analytes of interest due to the porous nature of the cuboidal shell.[128]

AuNRs employed as cores were synthesized using a seed-mediated method using cetyltrimethylammonium bromide (CTAB) as a stabilizing agent (see experimental section for details).[133] AuNRs were found to be monodisperse with a length of 49.9 ± 4.3 nm and a diameter of 14.4 ± 1.5 nm, estimated from a particle count > 100 in transmission electron microscopy (TEM) images (Figure 4.2A). A thin Ag shell is formed on the AuNR by introducing the AuNR into a growth solution comprised of silver nitrate ($AgNO_3$) as an Ag precursor, ascorbic acid as a reducing agent, and hexadecyltrimethylammonium chloride (CTAC) as a stabilizing agent (see experimental section). The Ag shell grew epitaxially on the surface of AuNR cores, which resulted in the formation of AuNR@Ag core-shell nanocuboids. The selective adsorption of CTAC on the {100} facets of Ag resulted in the formation of core-shell nanostructures with six {100} facets.[131] The synthesized AuNR@Ag core-shell nanocuboids were found to be monodisperse with a length of 83.9 ± 5.0 nm and width of 56.7 ± 3.1 nm estimated from a particle count > 100 in TEM images (Figure 4.2B). TEM images reveal the occupation of the AuNR at the center of each nanocuboid when viewed along the long-axis and from the sides (insets of Figure 4.2B). The thickness of the Ag shell grown on the sides of AuNR is found to be higher compared to that at the ends indicating the preferential growth of Ag on the sides compared to the ends. The aspect ratio of AuNR@Ag nanocuboids is smaller than

that of the AuNR cores due to the anisotropic Ag shell growth, which is in agreement with a previous report.[141]

Plasmonic nanorattles were synthesized by adding a Au precursor, i.e., $HAuCl_4$ to a solution of AuNR@Ag nanocuboids, which galvanically oxidizes the Ag layer to form a porous Ag-Au alloyed layer physically separated from the AuNR core. A TEM image of the Au nanorattles shows the presence of a porous cuboid Au-Ag shell surrounding the intact AuNR core (Figure 4.2C). From the TEM image, the length and width of the nanorattles was measured to be 89.3 ± 4.9 nm and 60.6 ± 3.0 nm, respectively, and the wall thickness of the shell was measured to be 6.5 ± 0.7 nm (Figure 4.2C). A higher magnification TEM image reveals a sub-10 nm gap between the edge of the AuNR and the porous plasmonic shell. Such a small gap results in strong plasmon coupling between the solid core and porous shell and the formation of electromagnetic hotspots within the nanostructure.[161]

The extinction spectrum of AuNRs employed as cores exhibits characteristic bands at 511 nm and 723 nm, corresponding to the transverse and longitudinal LSPR modes of the nanostructure, respectively (Figure 4.2D). Following the growth of a thin Ag layer on the AuNRs, the AuNR core-Ag shell nanostructures exhibited four LSPR bands in the extinction spectrum. The extinction bands at 495 and 570 nm correspond to transverse and longitudinal dipolar LSPR modes, which are clearly blue-shifted relative to those of the AuNRs. The bands at 342 and 420 nm correspond to the transverse octupolar and quadrupolar LSPR modes of the AuNR core-Ag shell nanocuboids.[141] In the galvanic replacement reaction, with the addition of the Au precursor, the LSPR bands associated with the presence of the Ag shell on the AuNR core disappeared. There was a concomitant emergence of LSPR bands at longer wavelengths that red-shifted with an increase in the Au precursor amount. The Au nanorattles dispersed in

aqueous solution display an LSPR wavelength maximum at 628 nm and a shoulder at 520 nm. Photographs (shown as insets of the TEM images in Figure 4.2) of AuNR, AuNR@Ag nanocuboid and Au nanorattle solutions under ambient light demonstrate the distinct extinction characteristics of the nanostructures.

In addition to the ensemble extinction spectra of nanostructures dispersed in aqueous medium, dark-field scattering spectra of individual nanostructures were also collected. The nanostructures were drop-casted from colloidal solution onto a glass slide, ensuring a low enough area density of coverage such that individual nanostructures could be resolved. The substrate-supported nanostructures were immersed in water and excited by unpolarized white light focused using a dark field condenser. For each sample, an individual emitter was identified from the wide-field of emitters and the scattered light from the emitter was collected using a 100x oil objective, transmitted through a slit, and dispersed onto a grating spectrometer to obtain a scattering spectrum. Figure 4.2E presents the dark-field scattering spectrum of a representative individual AuNR@Ag nanocuboid. The spectrum shows a band peaked at 564 nm and a shoulder around 500 nm, respectively corresponding to the longitudinal and transverse dipolar LSPR modes of the nanostructure. The scattering spectrum of an individual Au nanorattle is shown in Figure 4.2F. The stronger band in the spectrum peaked at 677 nm corresponds to the longitudinal dipolar resonance mode and the weaker one peaked at 612 nm is assigned to the transverse mode. The weak shoulder around 520 nm corresponds to a quadrupolar mode of the Au nanorattle.

Following the synthesis of the nanostructures, we acquired SERS spectra from the nanostructures dispersed in aqueous medium using 514.5 nm and 785 nm laser excitation. To measure the SERS activity, the nanostructures were exposed to a solution of a model analyte 2-

naphthalenethiol which readily chemisorbs on Au and Ag surfaces.[145] The Raman spectrum of bulk 2-NT (powder) is shown in Figure S3.1 in the Supporting Information. The Au nanorattles exhibited significantly higher SERS enhancement compared to the AuNR@Ag nanocuboids for both 514.5 and 785 nm laser excitation (Figures S3.2 and S3.3). The SERS spectra obtained under 514.5 nm laser excitation exhibited significantly higher intensity compared to that obtained using 785 nm excitation, which can be ascribed to the greater proximity of the LSPR bands of the nanostructures in aqueous medium to the 514.5 nm excitation as compared to 785 nm excitation. On the other hand, for isolated nanostructures deposited on silicon substrate, higher SERS intensity was observed for 785 nm laser excitation compared to that under 514.5 nm excitation. In fact, no discernable SERS signal was observed under 514.5 nm laser excitation. This observation can be attributed to a major shift of the LSPR modes of the nanostructures away from the 514.5 nm excitation. It has been demonstrated that the LSPR wavelength maximum of Ag nanoparticles exhibits a red shift of around 100 nm when deposited on a glass substrate due to the effective increase in the refractive index of the surrounding medium.[178] DDA simulations of the extinction spectra of the AuNR@Ag nanocuboid support such an explanation (Figure S3.4). The simulated extinction spectrum of AuNR@Ag nanostructure in water medium shows four LSPR bands around 345 nm, 406 nm, 477 nm, and 582 nm, in close agreement with the experimental extinction spectrum. In addition, the simulations show that a higher R.I. medium (corresponding to the nanocuboid supported on a Si substrate in air) results in a considerable red-shift of the LSPR bands of the nanostructure.[178] Under these conditions, the extinction contribution at 514.5 nm becomes significantly smaller, whereas the strongest (longitudinal dipolar) LSPR band overlaps considerably with the 785 nm laser, making the latter a significantly better excitation source for obtaining SERS enhancement as compared to the 514.5

nm excitation. These considerations rationalize the choice of the 785 nm laser as the excitation source for subsequent polarization-dependent SERS studies.

Next, we turn our attention to the polarization-dependent SERS activity of anisotropic AuNR@Ag nanocuboids and cuboidal Au nanorattles at the individual nanostructure level. To measure the SERS activity, the nanostructures deposited on a silicon substrate were exposed to 2-NT (10 mM in ethanol). Polarization-dependent SERS spectra were collected from individual nanostructures under 785 nm laser excitation at various orientation angles (Figure 4.3A, D). The orientation angle was defined as the angle between the long axis of the nanostructure and the direction of the excitation laser polarization. The orientation of the nanostructure relative to the polarization direction of the excitation laser was identified from SEM images spatially correlated to dark-field images (Figure S3.4 and S3.5). The SERS spectra obtained from an individual AuNR@Ag nanocuboid at various orientation angles are shown in Figure 4.3B. The most prominent peaks were observed at 1066 and 1381 cm^{-1}, which correspond to the C-H bending and ring stretching vibrations of 2-NT.[146] Each spectrum shown is an average of five spectra collected from the nanostructure under the same orientation. It is worth noting that well-resolved SERS spectra were obtained from individual AuNR@Ag nanocuboids, demonstrating the excellent SERS activity of these nanostructures. The SERS spectra collected from a AuNR@Ag nanocuboid (Figure 3C) at different orientations (-90° to 90°) in 15° intervals show a large variation in the intensity of the Raman bands with a change in the orientation. Maximum SERS activity was observed when the polarization of the laser was at an angle of 30° with respect to long-axis of the nanostructure.

The polarization-dependent SERS activity of a cuboid Au nanorattle (Figure 4.3E) was investigated using a similar method described above. It worth noting that the maximum SERS

intensity from the cuboid nanorattle was nearly three-fold higher that from the representative AuNR@Ag nanocuboid (Figure 4.3C and F). The SERS spectra obtained from the cuboid nanorattle at various polarization angles show that the SERS intensity of the most intense Raman band at 1381 cm^{-1} drops monotonically from a maximum value at 0° to a minimum at 90° and -90° (Figure 4.3E and F). This polarization dependence is in stark contrast to that observed in the case of AuNR@Ag nanocuboids. This contrasting behavior can be rationalized by the location of the most intense field hotspots of each of these nanostructures, as discussed below.

We employed FDTD simulations to understand the electromagnetic field distribution and the SERS enhancement from the plasmonic nanostructures. It is known that the SERS intensity scales as the product of electromagnetic field intensity enhancements at the incident and Stokes-shifted wavelength. Considering that we have employed the most intense Raman band of 2-NT at 1381 cm^{-1} for probing the polarization-dependent SERS activity, the corresponding Stokes-shifted wavelength is ~ 880 nm for the 785 nm excitation wavelength. The spatial maps of electrical field intensity around the AuNR@Ag nanocuboid and Au nanorattle under 785 nm excitation and at various polarization angles from 0° to 90° are shown in Figure 4.4A and C. The electric field intensity distribution of AuNR@Ag nanocuboids shows that the highest electric field intensity occurs at the corners of the solid nanostructures (termed the nanoantenna effect) and maximum enhancement is achieved when the polarization of the laser is along the diagonal of the cuboid (i.e. 30°). On the other hand, in the case of cuboidal Au nanorattles, the highest electric field intensity was found to be at the gap between the AuNR core and the cuboidal shell. The maximum electric field enhancement was observed when the polarization of the incident laser matched the long-axis of the nanostructures. Figure 4.4B and D depict the

product of the intensity enhancements at incident and Stokes-shifted wavelengths ($|E_{785}|^2|E_{880}|^2$), which provides a measure of the average SERS enhancement obtained from the AuNR@Ag nanocuboid and the Au nanorattle. The magnitude of $|E_{785}|^2|E_{880}|^2$ for the cuboidal nanorattle decreased with an increase in the polarization angle with respect to the long axis of the anisotropic nanostructure. On the other hand, the magnitude of $|E_{785}|^2|E_{880}|^2$ for the AuNR@Ag nanocuboid exhibited a maximum at a polarization angle of -30° and 30°. Polarization-dependence of the enhancement factor of both nanostructures simulated by FDTD shows excellent agreement with the experimental results.

4.5 Conclusions

In conclusion, we have performed a systematic investigation of the polarization-dependent SERS activity of AuNR@Ag nanocuboids and cuboidal Au nanorattles. Due to the presence of internal electromagnetic hotspots within the nanorattles, they exhibited SERS activity with a significantly different polarization-dependence compared to their solid counterparts i.e. AuNR@Ag nanocuboids. Similar to most conventional anisotropic solid nanostructures, the nanocuboids exhibited a polarization-dependent SERS activity that is dominated by their sharp corners and edges. Conversely, for the cuboidal nanorattles, the internal electromagnetic hotspot formed between the AuNR core and the porous Ag-Au shell dominates the SERS activity of the nanorattles. FDTD simulations confirm that the nature of the electric field distribution and the location of field hotspots are the source of the observed polarization dependence. The results further our understanding of the SERS activity of this promising class of hollow nanostructures with internal electromagnetic hotspots and provide guidelines for the design of highly efficient SERS substrates based on these nanostructures. More importantly, the results provide detailed

insight into the optimal configuration for both solid and hollow anisotropic nanostructures for performing single nanoparticle-based SERS studies.

4.6 Supporting Information

Supporting Information for chapter 4 is provided in appendix 3.

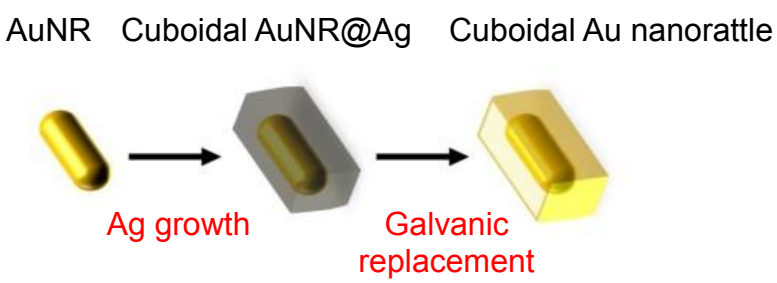

Figure 4. 1 Schematic illustration of the two-step synthesis of cuboidal Au nanorattles.

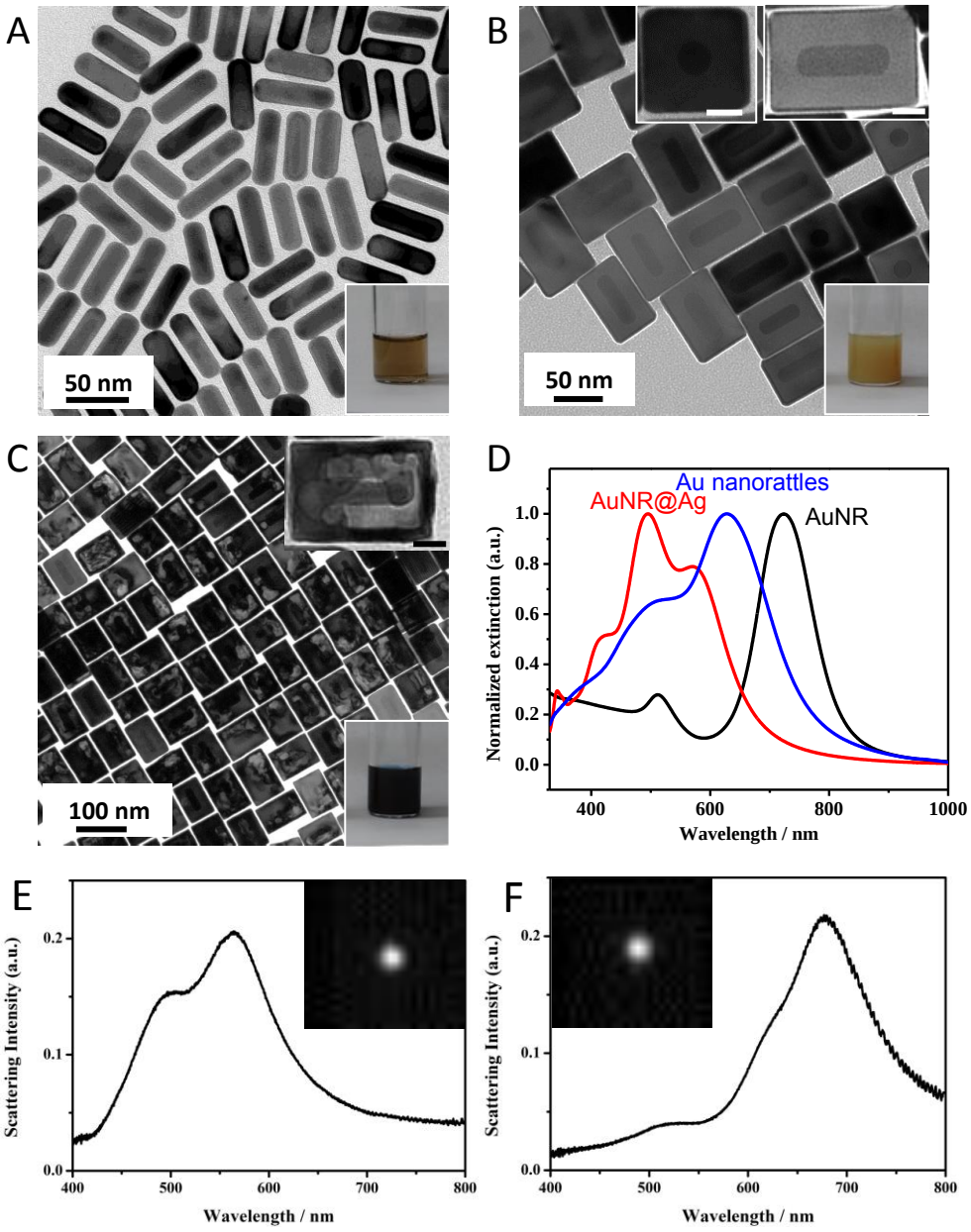

Figure 4. 2 TEM images of (A) AuNR nanostructures (inset shows a photograph of a colloidal solution of AuNR) (B) AuNR@Ag nanocuboids (bottom inset shows photograph of a colloidal solution of AuNR@Ag nanocuboids; top insets show higher magnification images when viewed along the long-axis and from the sides; scale bars represent 20 nm) (C) cuboidal Au nanorattles (bottom inset shows a photograph of a colloidal solution of Au nanorattles; top inset shows a higher magnification image; scale bar represents 20 nm and). (D) Vis-NIR extinction spectra of

AuNR, AuNR@Ag cuboids and cuboidal Au nanorattles in solution. Representative dark-field scattering spectrum of an individual (E) AuNR@Ag nanocuboid and (F) Au nanorattle. The inset in each panel shows a diffraction-limited dark-field optical image of the corresponding nanostructure.

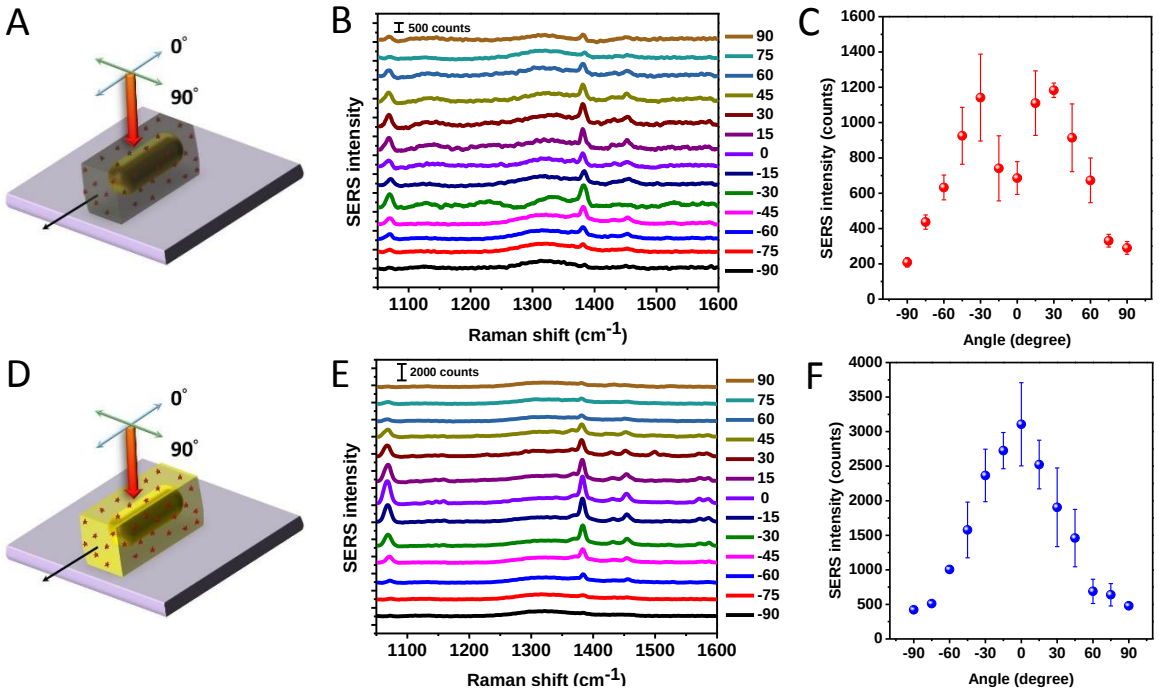

Figure 4. 3 (A) Schematic illustration depicting the measurement of the polarization-dependent SERS from a AuNR@Ag nanocuboid. (B) SERS spectra of 2-NT adsorbed on an individual AuNR@Ag nanocuboid obtained at various incident polarization angles. (C) Plot depicting the variation in the SERS intensity of the characteristic vibrational band at 1381 cm^{-1} as a function of the incident polarization angle from an individual AuNR@Ag nanocuboid. (D) Schematic illustration depicting the measurement of the polarization-dependent SERS from a cuboidal Au nanorattle. (E) SERS spectra of 2-NT adsorbed on an individual cuboidal Au nanorattle obtained at various incident polarization angles. (F) Plot depicting the variation in the SERS intensity of the characteristic vibrational band at 1381 cm^{-1} as a function of the incident polarization angle from an individual cuboidal Au nanorattle. The error bars correspond to the standard deviation of three identical measurements performed at each polarization angle.

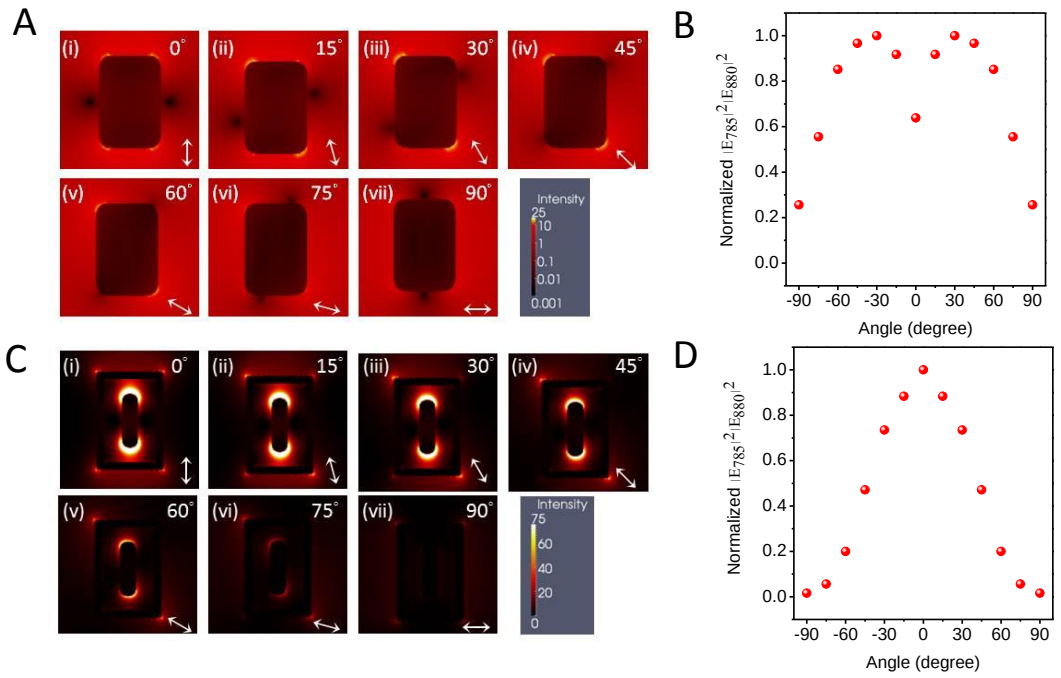

Figure 4. 4 (A) FDTD simulations showing the electric field distribution around a AuNR@Ag nanocuboid excited by 785 nm light with the incident polarization angle varied as 0°, 15°, 30°, 45°, 60°, 75° and 90° from (i)-(vii) respectively. An angle of 0° corresponds to polarization parallel to the long-axis of the nanostructure. The electric field intensity $|E_{785}|^2$ is shown on a log scale. (B) Normalized $|E_{785}|^2|E_{880}|^2$ for a AuNR@Ag nanocuboid as a function of the incident polarization angle. (C) FDTD simulations showing the electric field distribution around a Au nanorattle excited by 785 nm light with the incident polarization angle varied as 0°, 15°, 30°, 45°, 60°, 75° and 90° from (i)-(vii) respectively. An angle of 0° corresponds to polarization parallel to the long-axis of the nanostructure. The electric field intensity $|E_{785}|^2$ is shown on a log scale. (D) Normalized $|E_{785}|^2|E_{880}|^2$ for a Au nanorattle as a function of the incident polarization angle.

Chapter 5: Structure-dependent SERS Activity of Plasmonic Nanorattles with Built-in Electromagnetic Hotspots

The results reported in this chapter were submitted.

5.1 Abstract

Hollow plasmonic nanostructures with built-in and accessible electromagnetic hotpsots such as plasmonic nanorattles obtained through galvanic replacement reaction are highly attractive in surface enhanced Raman scattering (SERS)-based chemical and biological sensors and as contrast agents for SERS-based bioimaging. While their size, shape and orientation-dependent SERS enhancement has been reported, the effect of nanoscale structure, which is determined by the extent of galvanic replacement of the templates, has not been reported. In this study, we investigate the SERS activity of plasmonic nanorattles obtained through different degrees of galvanic replacement of Au@Ag nanocubes. We found that the observed SERS enhancement is governed by the plasmon extinction intensity, LSPR wavelength of the nanostructures with respect to the excitation source and intensity of electromagnetic field at the hotspot, with the latter playing a determining role. Finite-difference time-domain (FDTD) simulations showed excellent agreement with the experimental findings that an optimal degree of galvanic replacement is critical for maximum SERS enhancement. Paper-based SERS substrates fabricated using plasmonic nanorattles with optimal galvanic replacement exhibited an excellent SERS sensitivity and a low limit of detection of a model analyte.

5.2 Introduction

Surface enhanced Raman scattering (SERS) involves the large enhancement of Raman scattering from analytes adsorbed on or in close proximity to nanostructured metal surface. SERS is considered to be highly promising for the detection of trace levels of chemical and biological analytes, environmental monitoring and bioimaging.[16, 26, 108-110, 112, 114, 115, 117, 179, 180] Extensive efforts have been dedicated to the design and fabrication of SERS substrates that provide a large and uniform enhancement. The last decade has witnessed a remarkable progress in the synthesis of size- and shape-controlled plasmonic nanostructures of various noble metals such as gold and silver.[15, 16, 108, 109] These chemical methods (such as seed-mediated, polyol synthesis) led to the synthesis of plasmonic nanostructures with precisely controlled optical properties, which significantly improved our understanding of SERS and take it closer to real-world applications. Electromagnetic hotspots at the nanoscale gaps between assembled or mildly aggregated plasmonic nanostructures are known to be responsible for large SERS enhancement.[26, 181-183] A relatively small number of electromagnetic hotspots (63 out of 10^6 active sites) have been found to result in a significant fraction (~25%) of the overall SERS signal, highlighting the importance of electromagnetic hotspots in the design of SERS probes.[184] Although extensive efforts have been dedicated to achieve controlled assembly of plasmonic nanostructures, scalable nanoparticle assemblies that offer highly uniform, isotropic and stable SERS enhancement remains challenging. An alternate approach involves the design and synthesis of plasmonic nanostructures with built-in electromagnetic hotspots.[185-187] Such nanostructures with built-in hotspots obviate the need for assembly of plasmonic nanostructures greatly simplifying the fabrication of SERS substrates with high and uniform enhancement.

Recently, we have demonstrated that plasmonic nanorattles comprised of Au core and porous Au-Ag shell provide a large SERS enhancement owing to the internal electromagnetic hotspot formed between the core and shell.[128,161] The porous outer shell facilitates facile diffusion of analytes into the electromagnetic hotspots within the nanostructures. The electromagnetic field and the SERS enhancement of the nanorattles were found to be highly dependent on size and shape of the nanorattles and the orientation of the anisotropic nanorattles with respect to the polarization of the incident laser.[161, 188] Apart from size and orientation the nanoscale structure (*i.e.* gap between the core and porous shell) of the Au nanorattles, which is governed by the extent of galvanic replacement, is expected to play a determining role in the observed SERS enhancement. However, there is no systematic study that unveils a correlation between the extent of galvanic replacement and the SERS enhancement of the plasmonic nanorattles.

In this work, we investigate the correlation between structure, optical properties and SERS enhancement of plasmonic nanorattles obtained through controlled galvanic replacement of Au@Ag nanocubes (Figure 5.1). In order to probe the correlation between the extent of galvanic replacement reaction and SERS enhancement, the plasmonic nanorattles were designed with a Raman reporter-coated Au nanosphere as core and porous Ag-Au shell. Galvanic replacement of Au@Ag nanostructures results in the formation of nanorattles in which the core and shell are separated resulting in the formation of an internal electromagnetic hotspot. The SERS enhancement of the plasmonic nanorattles is found to strongly depend on the extent of galvanic replacement reaction. Finite-difference time-domain simulations, employed to estimate the electromagnetic field enhancement within these nanostructures, showed an excellent agreement with the experimental findings.

5.3 Experimental Section

Materials

Cetyltrimethylammonium bromide (CTAB), gold chloride ($HAuCl_4$), sodium borohydride, silver nitrate, ascorbic acid, 2-naphthalenethiol and 4-aminothiophenol were purchased from Sigma-Aldrich. Cetyltrimethylammonium chloride (CTAC) was purchased from Tokyo Chemical Industry (TCI). Filter paper (Whatman #1) was purchased from VWR international. All the chemicals were used as received without further purification. Nanopure water (18.2 MΩ-cm) was used for all the experiments.

Synthesis of Au Nanospheres

Au nanospheres were synthesized using a previously reported procedure.[189-191] Au seeds were synthesized by adding 0.6 ml of ice-cold sodium borohydride solution (10 mM) into a solution containing 0.25 ml of $HAuCl_4$ (10 mM) and 9.75 ml of CTAB (0.1 M) under vigorous stirring at room temperature. The color of seed solution changed from yellow to brown. Seed solution was kept undisturbed at room temperature for 3 h. 0.25 ml of the seed solution is added to a growth solution containing 10 ml of CTAC (0.2 M) and 7.5 ml of ascorbic acid (0.1 M) under stirring. 10 ml solution of $HAuCl_4$ (0.5 mM) is added to the growth solution as a one-shot injection. The resulting solution containing 10 nm Au nanospheres was centrifuged at 13,000 rpm for 30 minutes. For further growth of nanoparticles, 30 ml of CTAC (0.1 M) and 1.95 ml of ascorbic acid (10 mM) are mixed. To the resulting solution 1.2 ml of 10 nm Au nanospheres (extinction 1.0) was added under stirring. A 30 ml solution of $HAuCl_4$ (0.5 mM) is injected into the above mixtre at the rate of 0.5 ml/min under stirring. The reaction is allowed to complete and the resulting solution containing 30 nm Au nanospheres was centrifuged at 8000 rpm for 10 min.

Synthesis of 2-NT-Au@Ag nanocubes

For the synthesis of 2-NT-Au@Ag core-shell nanocubes, 25 µl of 2-NT (10 mM) was added to 5 ml of 30 nm Au nanospheres under vigorous sonication for 10 min. These modified Au nanospheres were centrifuged at 9000 rpm for 10 min to remove the unadsorbed 2-NT, then dispersed in 5 ml of CTAC (10 mM) and centrifuged again. 1 ml of 2-NT-coated Au nanospheres (extinction ~1.2) and 9 ml of CTAC (20 mM) were mixed at 60 °C under stirring for 20 min. 1 ml of $AgNO_3$ (2 mM), 2.5 ml of CTAC (20 mM) and 0.5 ml of ascorbic acid (0.1 M) were added under stirring at 60 °C for 4 h. The 2-NT-Au@Ag nanocube solution was centrifuged and the nanostructures were redispersed in 2 ml of nanopure water. The procedure to synthesize Au@Ag is similar except that the Au nanospheres are not coated with 2-NT.

Synthesis of Au Nanorattles

Au nanorattles were synthesized by transforming the silver shell of 2-NT-Au@Ag nanocubes into a porous Au-Ag alloyed shell via galvanic replacement reaction. Varying amounts of aqueous $HAuCl_4$ solution (0.5 mM) was injected into the 100 µl of 2-NT-Au@Ag nanocube solution. The obtained Au nanorattles solution was centrifuged at 10,000 rpm for 10 min and dispersed in nanopure water.

Spectroscopy Measurements

SERS spectra from nanostructures dispersed in aqueous solution was obtained using a Renishaw inVia confocal Raman spectrometer. Spectra were collected using the 514.5 nm laser excitation wavelength, which was focused on the solution surface using a 20X objective with 30 sec

exposure time. The laser power was measured to be approximately 0.7 mW at the samples surface. UV-Vis extinction spectra were collected using Shimadzu UV-1800 UV-Vis spectrophotometer.

Microscopy Characterization

Transmission electron microscopy (TEM) images were collected using a JEOL JEM-2100F field emission microscopy. Scanning electron microscopy (SEM) images were obtained using a FEI Nova 2300 Field Emission SEM at an accelerating voltage of 10 kV.

Finite-difference time-domain (FDTD) simulations

Electromagnetic field distribution around the plasmonic nanorattles with different sizes was simulated by using three-dimensional finite-difference time-domain (FDTD) with a commercially available software (EM Explorer). FDTD simulations exploit the time and position dependence of Maxwell's equations to model the electromagnetic waves in rectangular 3D cells (Yee cells) of a finite volume. A Yee cell size of 0.15 μm is used in the current study, which is about 1/4th of the wavelength of the excitation wavelength. Perfectly Matched Layer (PML) absorbing boundary conditions were applied in all directions of the simulation domain. The AuNP core was defined as a sphere with a diameter of 31 nm and the edge length of hollow Au shells was defined to be 59 nm and the gap distance between the core and the shell was to be 0, 2, 4, 6, 8, and 10 nm. The simulation domain was defined to be 150 nm × 150 nm × 150 nm. A high-resolution simulation was run at the excitation (λ_{ex}=514 nm) and Stokes-shifted wavelength (λ_{ex}=553 nm) to obtain the electromagnetic field distribution. The complex refractive index was set to be n=0.71＋i1.96 for gold and n=0.14＋i2.91 for silver at the wavelength of 514 nm. At

the wavelength of 553 nm, the complex refractive index was set to be n=0.40＋i2.38 for gold and n=0.15＋i3.21 for silver. The refractive index of surrounding medium was set to be 1.33 (that of water).

5.4 Results and Discussion

The synthesis of plasmonic nanorattles starts with the synthesis of spherical gold nanoparticles using a seed-mediated method.[189-191] The spherical Au nanoparticles serve as a seed for the synthesis Au@Ag nanostructure.[191] Au nanoparticles with a diamater of 30 nm were synthesized using a two-step seed-mediated method. In the first step, Au nanoparticles with a diameter of 10.9±0.6 nm were synthesized using seed-mediated method (Figure S4.1A, see Experimental section). Extinction spectrum revealed the LSPR wavelength of Au nanospheres to be at ~523 nm (Figure S4.1B). In the second step, the ~10 nm Au nanoparticles were employed as the seeds for the synthesis of Au nanospheres with larger diameter (30.8±0.8 nm) (Figure S4.1C). Through ligand-exchange reaction, the Au nanospheres were modified with 2-naphthalenethiol (2-NT), which serves as a Raman reporter. Extinction spectrum revealed a red-shift of ~1 nm in the LSPR wavelength of the Au nanospheres following the ligand exchange (Figure S4.1D).

The synthesis of Au@Ag nanostructures involves the formation of a thin Ag shell by the addition of 2-NT-coated Au nanospheres into a growth solution comprised of silver nitrate as silver precursor, cetyltrimethylammonium chloride (CTAC) as stabilizing agent and ascorbic acid as the reducing agent (see Experimental section for details).[131, 161] Thin silver shell was epitaxially grown on the surface of 2-NT-coated Au nanospheres resulting in the formation of Au@Ag core-shell nanocubes. The edge length of Au@Ag core-shell nanocubes was found to be 58.9± 1.9

nm from TEM images (Figure 5.2D). To synthesize gold nanorattles with different degrees of galvanic replacement, varying amounts (0-100 µl) of $HAuCl_4$ (0.5 mM) was added into 100 µl of Au@Ag nanocubes solution. As expected, extinction spectra revealed a progressive red shift in the LSPR wavelength with an increase in the amounts of $HAuCl_4$ during the galvanic replacement (Figure 5.2A-C).[131, 192, 193] TEM and SEM images show the Au@Ag nanocubes and Au nanorattles at different stages of the galvanic replacement reaction (Figure 5.2D-I and Figure S4.2A-F in supporting information). When an aqueous solution of $HAuCl_4$ is introduced into the Au@Ag nanocube solution, the structural and morphological changes of Au@Ag nanocubes were observed under the following main stages as reported previously.[59, 194, 195] (i) Ag dissolution from defective site on the side face; (ii) dissolution of bulk Ag from the interior of the nanostructure with simultaneous deposition of Au on reminder of the cube; (iii) formation of a hollow and porous Au and Ag alloy shell with uniform wall thickness; and (iv) finally, disintegration of the porous shell resulting in small irregular fragments.

To compare the SERS activity of the nanostructures at different stages of the galvanic replacement process, we acquired Raman spectra from nanostructures dispersed in water using 514.5 nm laser as excitation source. SERS spectra obtained from Au nanostructures at different stages of the galvanic replacement display most prominent Raman bands at 1066 and 1381 cm^{-1}, which correspond to the C-H bend and ring stretch vibrations of 2-NT, respectively (Figure 5.3A and Figure S4.3).[146] These two most intense bands were employed to compare the SERS activity. Maximum SERS intensity was observed for nanorattles obtained by adding 20 µl of 0.5 mM $HAuCl_4$ into 100 µl of 2-NT-Au@Ag nanocubes (called 20-AuNRT henceforth). The SERS intensity of 20-AuNRT was nearly five times higher compared to that obtained from pristine Au@Ag nanocubes (*i.e.* 0-AuNRT) (Figure 5.3A-C). With further addition of $HAuCl_4$, the

SERS intensity of the Au nanorattles rapidly decayed. The variation in the SERS activity of nanostructures with the extent of galvanic replacement can be ascribed to the plasmon extinction intensity, LSPR wavelength with respect to the excitation laser wavelength and the intensity of the electromagnetic hotspots within the nanostructures. At 514.5 nm, the LSPR extinction intensity of 0-AuNRT was found to be higher compared to 20-AuNRT (Figure 5.2A). However, owing to the electromagnetic hotspots within the 20-AuNRT, the SERS intensity obtained from 20-AuNRT was higher compared to 0-AuNRT. Subsequent increase in the amount of titrated $HAuCl_4$ resulted in a decrease in the observed SERS intensity. The observed drop in the SERS intensity emanates from the increase in the gap between core and porous shell, which decreases the intensity of the internal hotspot (discussed in detail below), and a drop in the extinction intensity due to the replacement of Au with Ag with the latter known to have a stronger plasmon compared to the former.

In order to understand the electromagnetic field intensity distribution and SERS enhancement from the Au nanorattles with different extent of galvanic replacement, finite-difference time-domain (FDTD) simulations were employed. To estimate the enhanced electromagnetic field intensity of pristine Au@Ag nanocubes and Au nanorattles, we have calculated the average electromagnetic field intensity for the polarization along the [100] and [110] directions. It is known that the average SERS intensity is proportional to the square of the product of the gain in the incident and Raman scattering light.[148] For 514 nm excitation wavelength, the Stokes-shifted wavelength corresponding to 1381 cm^{-1} Raman band is calculated to be at ~553 nm. The spatial maps of electrical field intensity (λ_{ex}= 514 and 553 nm) around the Au@Ag nanocubes and Au nanorattles (with 0, 2, 6 nm gap and Au core) for polarization parallel to the sidewall ([100] direction) are shown in Figure 5.3D as representative examples. For both excitation wavelengths

(514 and 553 nm) electromagentic field intensity at the internal hotspot (between core and shell) was found decrease with increase in the gap size. Furthermore, the intensity at the corners (the most intense regions) of the prisitne Au@Ag nanocubes was found to be higher for under 514 nm excitation compared to 553 nm excitation due to the proximity of the LSPR wavelength of the Au@Ag nanostructures (495 nm) to 514 nm excitation compared to 553 nm excitation. The spatial maps of electrical field intensity (λ_{ex}=514 nm) around the Au@Ag nanocubes and Au nanorattles along [100] direction and along the diagonal ([110] direction) are shown in Figure S4.4 and Figure S4.5, respectively. The spatial maps of electrical field intensity (λ_{ex}=553 nm) around the Au@Ag nanocubes and Au nanorattles with polarization along [100] and [110] direction are shown in Figure S4.6 and S4.7, respectively. We have plotted the square of the product of the gain in the electric field at incident and Raman scattered wavelengths ($|E_{514}|^2|E_{553}|^2$), which represents the average SERS intensity from the Au@Ag nanocubes and Au nanorattles with different degrees of galvanic replacement (Figure 5.3E). The SERS intensity from the FDTD simulations was found to be highest for a gap size of 2 nm followed by a dramatic decrease with increase in the gap size. Overall, SERS intensity trend obtained from FDTD simulations show an excellent agreement with our experimental observations.

Paper has been demonstrated to be an attractive substrate for implementing various plasmonic sensors owing to its high specific surface area, flexibility, compatibility with conventional printing approaches and low-cost.[114, 115, 128, 196-198] We have employed paper as a platform for the fabrication of SERS substrates based on plasmonic nanorattles with optimal extent of galvanic replacement. The SERS substrates were fabricated by immersing the paper substrates in 20-AuNRT, which exhibited the highest SERS activity. These 20-AuNRT were synthesized using the same procedure except that the 30 nm Au cores were not coated with a Raman reporter.

SEM images demonstrated the uniform adsorption of the nanostructures on a filter paper (Figure 5.4A). The inset of Figure 5.4A shows the filter paper before and after the adsorption of the nanostructures, depicting the intense gray color of the filter paper substrate adsorbed with nanostructures. Vis-NIR spectrum obtained from the plasmonic paper depicts the extinction band corresponding to the 20-AuNRT (Figure S4.8). The Raman spectrum of the pATP molecule is shown in Figure S4.9 (See Supporting Information). SERS spectra obtained from the 20-AuNRT-adsorbed paper substrate after exposure to different concentrations of pATP in ethanol are shown in Figure 5.4B and Figure 5.4C. The most prominent Raman bands appear at 1074, 1141, 1389, 1437 and 1576 cm^{-1}, corresponding to Raman bands from pATP.[199-201] Raman band at 1576 cm^{-1}, corresponding to the aromatic ring vibration mode of pATP[199, 202], was used to determine the trace detection ability of the plasmonic paper substrate. The SERS intensity exhibited a monotonic increase with the increase in the concentration of the analyte (Figure 5.4D). In contrast, plasmonic paper based on pristine Au@Ag nanocubes exhibited significantly lower SERS intensity for identical concentration of the analyte. The limit of detection of the plasmonic paper based on 20-AuNRT was found to be 1 pM, which signifies the excellent sensitivity for the SERS-active plasmonic paper sensor.

5.5 Conclusions

In conclusion, we have demonstrated the synthesis of plasmonic nanorattles comprised of 2-NT coated Au nanosphere as core and porous gold cube as a shell with different degrees of galvanic replacement using Au@Ag nanocubes as templates. The nanoscale structure, optical properties and SERS enhancement of Au nanorattles was found to be highly dependent on the extent of the galvanic replacement. FDTD simulations employed to understand the electromagnetic field

intensity of the Au@Ag nanocubes and nanorattles exhibited excellent agreement with experimental findings. The optimal nanorattles were employed to fabricate a paper-based SERS substrate that exhibited excellent sensitivity and a trace detection limit of 1 pM. Overall, our findings highlight that an optimal degree of galvanic replacement is critical to maximize the SERS enhancement of these nanostructures, which can find numerous applications in chemical and biological sensors, bioimaging and targeted drug delivery.

5.6 Supporting Information

Supporting Information for chapter 5 is provided in appendix 4.

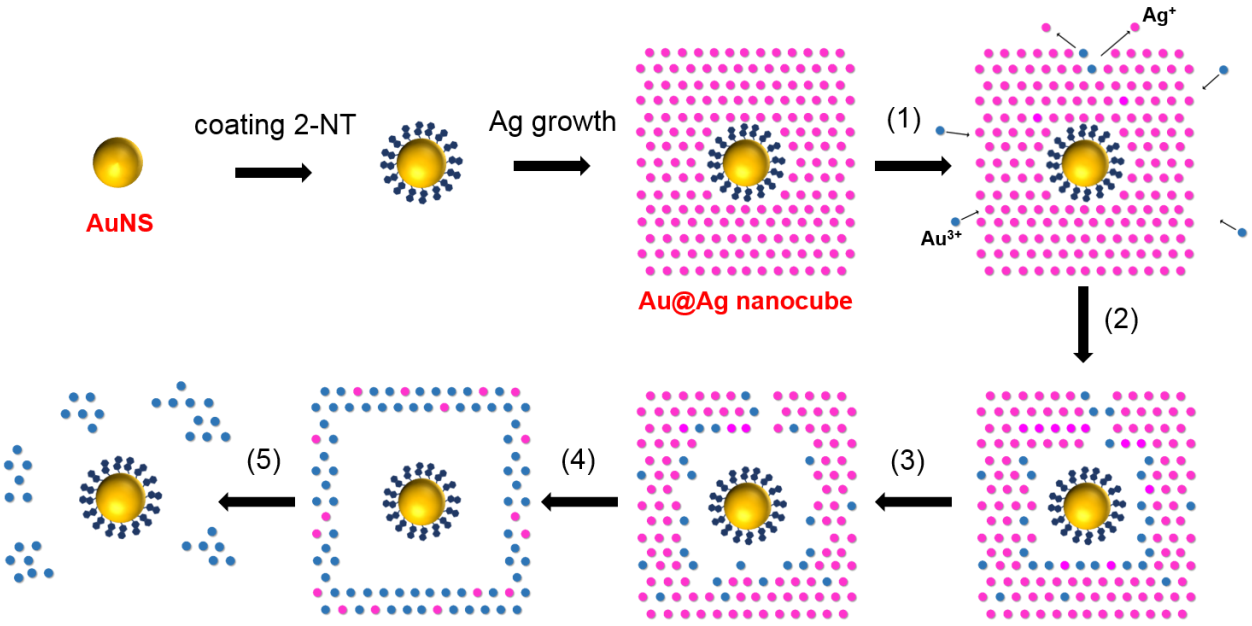

Figure 5. 1 Schematic illustration of the synthesis of 2-naphthalenethiol coated Au nanosphere followed by Ag layer growth and progressive galvanic replacement reaction with Au.

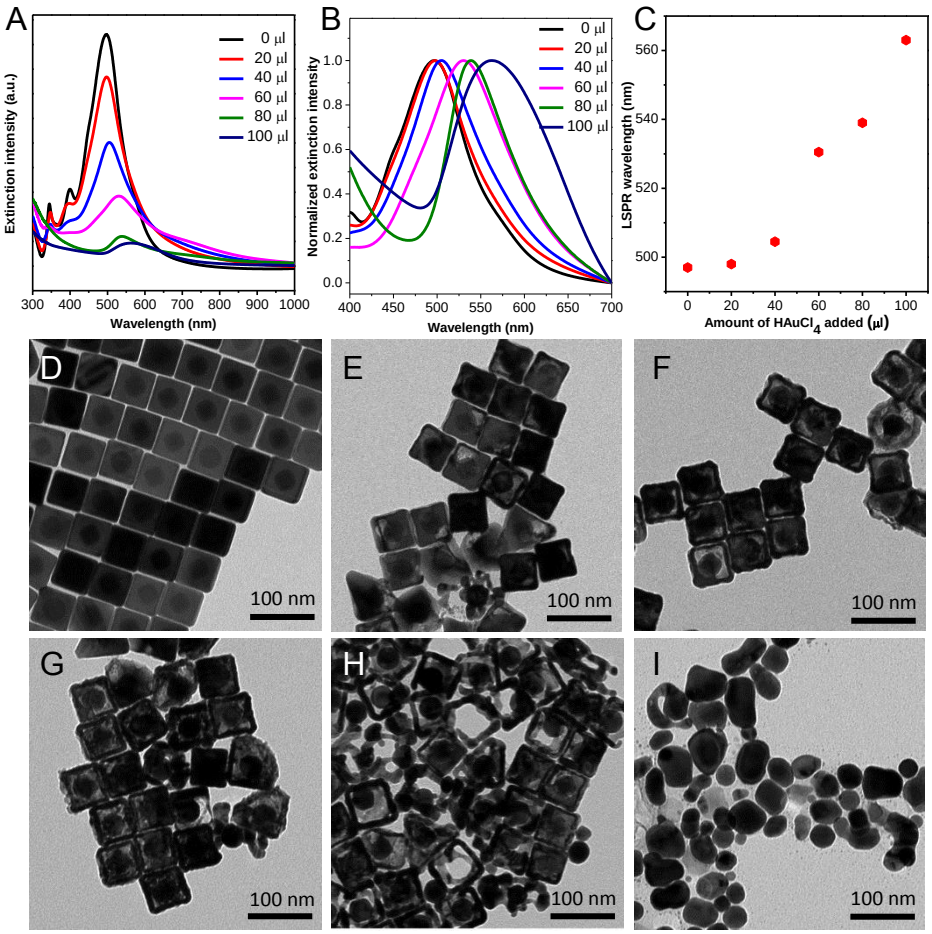

Figure 5. 2 (A) Vis-NIR extinction spectra of 2-NT-Au@Ag following the addition of different amounts of $HAuCl_4$ indicated in the plot. (B) Normalized vis-NIR extinction spectra of 2-NT-Au@Ag from (A) depicting the shift in the LSPR wavelength with the addition of $HAuCl_4$. (C) Plot depicting the LSPR wavelength and the volume of $HAuCl_4$ added. (D)-(I) TEM images of template and nanostructures obtained after adding 0, 20, 40, 60, 80 and 100 µl of $HAuCl_4$ (0.5 mM) into 100 µl of 2-NT-Au@Ag nanocubes.

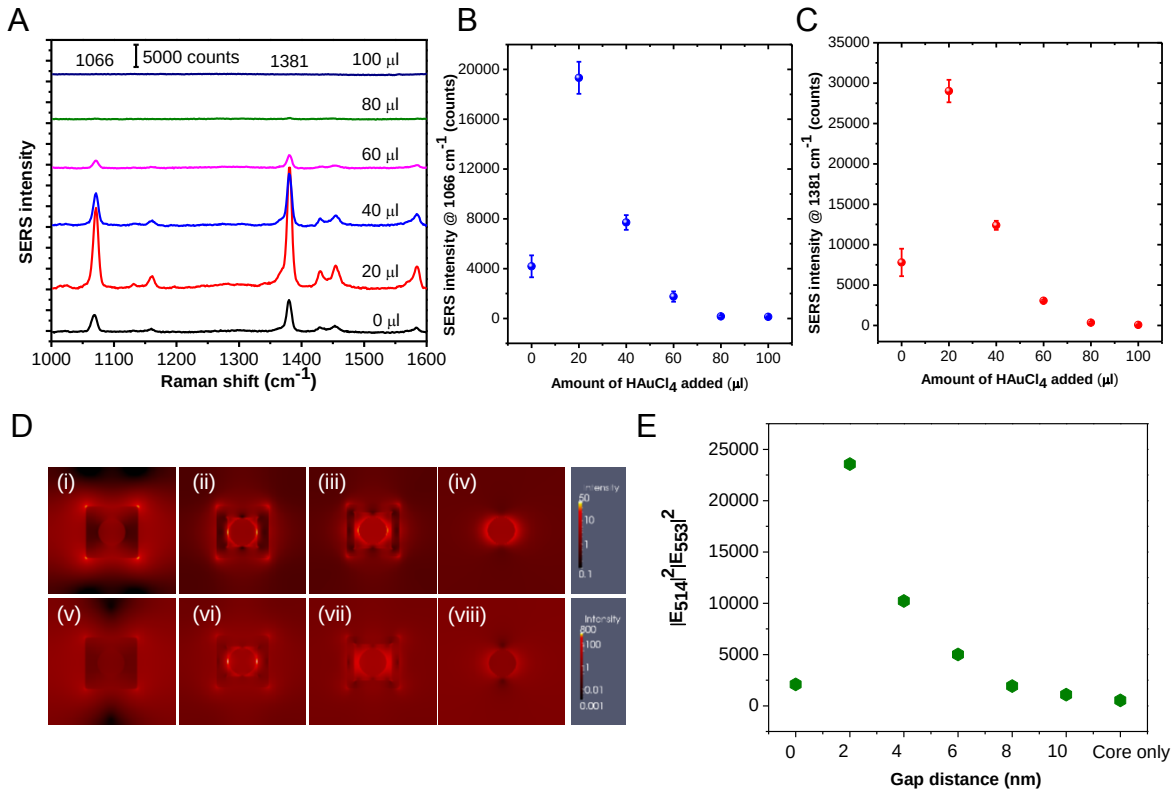

Figure 5. 3 (A) SERS spectra obtained from 2-NT-Au@Ag nanocubes after different degrees of galvanic replacement. SERS intensity at (B) 1066 cm^{-1} (C) 1381 cm^{-1} obtained from 2-NT-Au@Ag nanocubes after different degrees of galvanic replacement. (D) FDTD simulations showing the electric field distribution of Au@Ag nanocubes and Au nanorattles with different gaps between core and shell with electric field polarized along [100] under (i-iv) 514 nm and (v-viii) 553 nm excitation. (i and v), (ii and vi), (iii and vii) and (iv and viii) correspond to Au@Ag nanocubes and Au nanorattles with a gap of 0, 2, 6 nm and core only, respectively. (E) Plot showing the average $|E_{514}|^2|E_{553}|^2$ with electric field polarized along [100] and [110] for Au@Ag nanocubes and Au nanorattles with different gaps between core and shell.

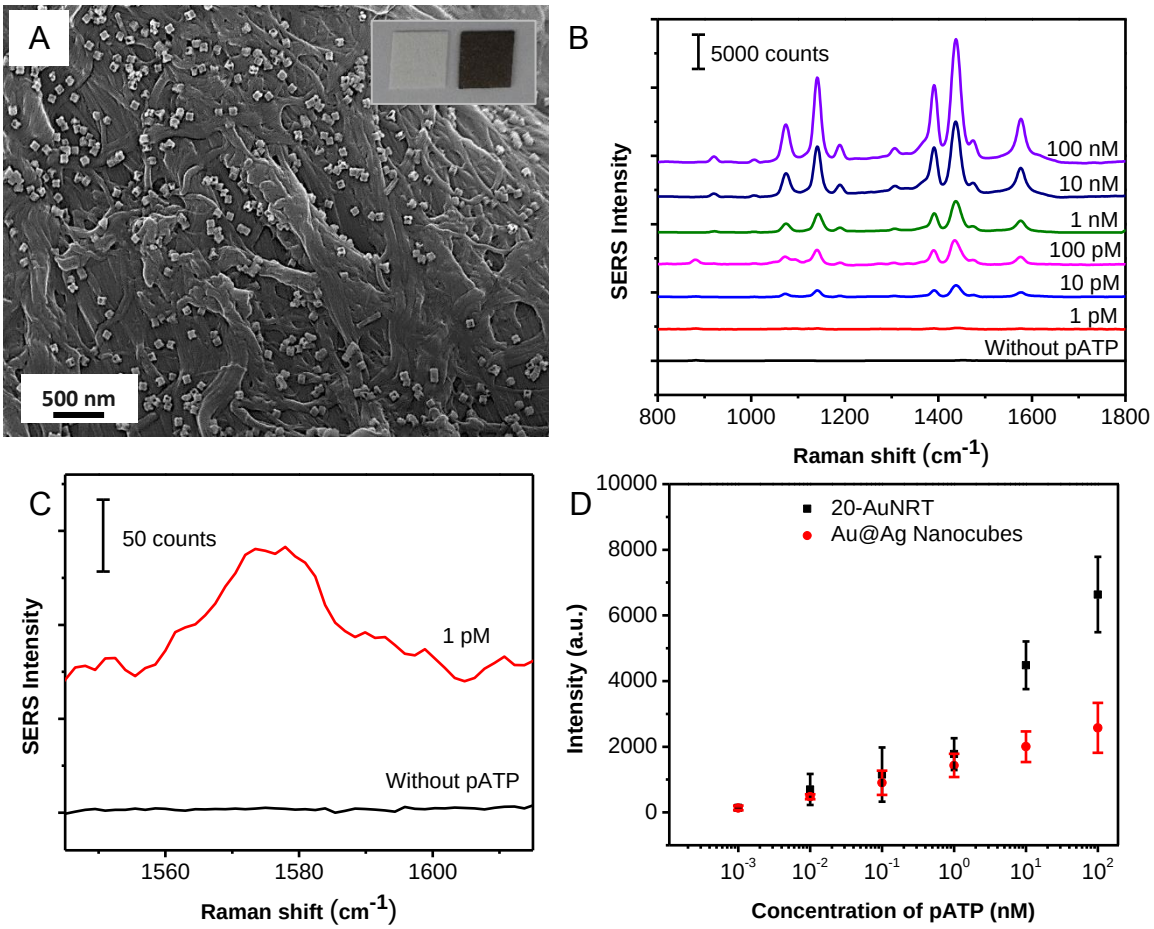

Figure 5. 4 (A) SEM image showing the uniform adsorption of 20-AuNRT on a paper substrate. Inset shows the photograph of the paper substrate before and after the adsorption of 20-AuNRT. (B) SERS spectra obtained from the 20-AuNRT-adsorbed paper substrate after exposing it to varying concentrations of pATP in ethanol. (C) Zoom-in spectra at a low concentration from Fig. 4(B). (D) Semi-log plot showing the concentration vs intensity of the 1576 cm^{-1} Raman band obtained from paper substrates with 20-AuNRT and Au@Ag nanocubes.

Chapter 6: Plasmonic Nanogels for Unclonable Optical Tagging

The results reported in this chapter were published in ACS Applied Materials & Interfaces, 2016, 8, 4031-4041. Reproduced with permission from American Chemical Society.

6.1 Abstract

We demonstrate the fabrication of novel functional gel coatings with randomized physical and chemical patterns that enable dual encoding ability to realize unclonable optical tags. This design is based on swelling-mediated massive reconstruction of an ultrathin responsive gelatinous polymer film uniformly adsorbed with plasmonic nanostructures into a randomized network of interacting folds, resulting in bright electromagnetic hotspots within the folds. We reveal a strong correlation between the topology and near-field electromagnetic field enhancement due to the intimate contact between two plasmonic surfaces within the folds, each of them representing a unique combination of local topography and chemical distribution caused by the formation of electromagnetic hotspots. Owing to the efficient trapping of the Raman reporters within the uniquely distributed electromagnetic hotspots, the surface enhanced Raman scattering enhancement from the morphed plasmonic gel was found to be nearly 40 times higher compared to that from the pristine plasmonic gel. Harnessing the nondeterministic nature of the folds, the folded plasmonic gel can be employed as a multidimensional (with dual topo-chemical encoding) optical taggant for prospective anti-counterfeiting applications. Such novel optical tags based on the spontaneous folding process are virtually impossible to replicate because of the combination of nondeterministic physical patterns and chemical encoding.

6.2 Introduction

There has been significant interest in migrating plasmonics from static substrates to dynamic surfaces, which provide tunability in the structure and properties of plasmonic nanostructures and their assemblies.[203-210] Dynamic surfaces include substrates or intermediate layers (between plasmonic nanostructures and rigid substrates) that bend, stretch, swell, and shrink with external physical or chemical stimuli. Responsive polymers that exhibit large changes in structure over a narrow range of external stimuli (e.g., pH, temperature, solvent quality) are highly attractive for realizing dynamic systems that are ubiquitous in biology.[211, 212] Extensive efforts have been made to harness the large conformational changes in responsive polymer systems such as ultrathin films, adsorbed layers, polymer brushes, micro/nanoparticles, and one-dimensional nanostructures to realize dynamic plasmonics.[206, 213-220] In most of these cases, the change in the polymer chain conformation results in a small change in the distance (a few nanometers) between the nanostructures that dramatically modulates the plasmon coupling between the nanostructures and the optical activity of the plasmonic assemblies. In parallel, there has been a growing interest in harnessing mechanical instabilities such as buckling, wrinkling and folding in soft and responsive materials to realize morphable materials with reversibly tunable structure and properties.[221] While a handful of studies demonstrate the use of mechanical instabilities such as buckling and wrinkling in ultrathin polymer films for assembling and patterning plasmonic nanostructures,[222, 223] their use in realizing dynamic and complex plasmonic systems remains largely unexplored.

Fast-growing counterfeit markets, including medicines, banknotes, and jewelry, pose serious threats to the health and safety of consumers, the economy, and national security.[224-226] These considerations highlight the importance and urgent need of unclonable and universally applicable

anti-counterfeiting strategies, which utilize unpredictable and nondeterministic encoding mechanisms with high coding capacity. Current anti-counterfeiting strategies are mainly focused on developing encoded taggants carrying either graphical or spectral information for strong authentication.[224, 225, 227, 228] Graphically encoded taggants are typically vulnerable to cloning attacks, including ones designed with nondeterministic encoding mechanisms, such as the recently demonstrated wrinkle patterns similar to human fingerprints.[226] Furthermore, most spectrally encoded taggants often suffer from deterministic encoding architectures and practical constraints, such as the lifespan of materials and the narrow product applicability.[229, 230]

Here we demonstrate that spontaneous folding of ultrathin responsive gels integrated with plasmonic nanostructures results in the formation of electromagnetic hotspots within the folded structures. Electromagnetic hotspots formed within the nanoscale gaps between assembled or mildly aggregated plasmonic nanostructures are highly attractive for surface-enhanced optical spectroscopies.[26, 128, 231, 232] Apart from using surface enhanced Raman scattering (SERS) intensity mapping as a facile imaging tool to reveal the spatial distribution of the near-field enhancement within the folded plasmonic gel, we demonstrate that the reconfigurable plasmonic gel film encoded with two different Raman reporters can serve as an excellent optical tag for anti-counterfeiting applications. Unlike the existing anti-counterfeit tags that rely on either physical features or spectroscopic fingerprints, the novel optical tags based on the spontaneous folding process provides a multidimensional anti-counterfeiting strategy that is virtually impossible to be replicated because of the combination of nondeterministic physical and chemical patterns.

6.3 Experimental Section

Materials

Chloroauric acid ($HAuCl_4$), silver nitrate ($AgNO_3$), sodium borohydride ($NaBH_4$), ascorbic acid, tetrahydrofuran (THF), nitromethane, 1,4-diodobutane (DIB), 2-naphthalenethiol (2-NT) and 4-Aminothiophenol (pATP) were purchased from Sigma-Aldrich, St. Louis, MO. Poly(2-vinyl pyridine) (M_w=200,000 g/mol) was obtained from Scientific Polymer Products. Methoxy PEG thiol (SH-PEG, M_w = 5,000 g/mol) was purchased from JenKem Technology. Hexadecyltrimethylammonium chloride (CTAC) was purchased from TCI. All purchased chemicals were used as received without further purification. Nanopure water (18.2 MΩ-cm) was used for all experiments.

Synthesis of Au nanorods (AuNRs) as core

Gold nanorods were synthesized using a seed-mediated approach.[190, 233] Seed solution was prepared by rapidly adding 0.6 ml of an ice-cold solution of $NaBH_4$ (10 mM) into 10 ml of 0.1 M CTAB and 2.5×10^{-4} M $HAuCl_4$ aqueous solution under vigorous stirring at room temperature. The color of the seed solution immediately changed from yellow to brown after $NaBH_4$ addition. Growth solution was prepared by mixing 95 ml of 0.1 M CTAB, 0.6 ml of 10 mM silver nitrate, 5 ml of 10 mM $HAuCl_4$, and 0.55 ml of 0.1 M ascorbic acid in the same order. The solution was homogenized by gentle stirring. To the resulting colorless solution, 0.12 ml of freshly prepared seed solution was added and set aside in dark for 14 h.

Synthesis and PEGylation of Ag coated AuNRs (Ag@AuNRs)

2 ml of twice centrifuged as-synthesized AuNR and 4 ml of 20 mM CTAC aqueous solution were mixed at 60 °C under stirring for 20 min. Subsequently, 5 ml of 2 mM $AgNO_3$, 2.5 ml of 80 mM CTAC and 2.5 ml of 0.1 M ascorbic acid aqueous solution were added to the above mixture. After 4 h of reaction, the Ag@AuNRs solution was cooled in an ice-cold water bath. The resultant AuNR solution was centrifuged at 6,000 rpm for 10 min to remove excess reactants

and redispersed into aqueous CTAC (80 mM) solution. To PEGylate the nanostructures, 100 µl of SH-PEG (2 mM) and 100 µl of NaCl (60 mM) were added to 0.8 ml of the above twice-centrifuged solution, followed by sonication for 1 h. The PEGylated Ag@AuNRs solution was centrifuged and dispersed in water for further use.

Fabrication of plasmonic gel films

P2VP solution was prepared as reported previously, by dissolving 0.1 g of P2VP in a mixture of 4.5 ml of nitromethane, 0.5 ml of THF and 0.1 ml of DIB.[234] The resultant solution was incubated in an oil bath at 60 °C for 2 h under stirring to facilitate the quaternization reaction between P2VP and DIB. The quarternized P2VP solution was deposited on silicon substrates by spin-coating, followed by annealing at 120 °C for 2 h. To achieve highly uniform adsorption of Ag@AuNRs, the P2VP films on silicon substrate was immersed in a high concentration of PEGylated Ag@AuNRs or PEGlated AuNRs solution (extinction intensity ~ 6 per cm light path) for 14 hours, followed by rinsing with nanopure water and drying with a stream of nitrogen. The P2VP film coated with high density of Ag@AuNRs was exposed to saturated pATP vapor for 12 hours, followed by degassing in vacuum. The P2VP film coated with high density of AuNRs was exposed to saturated pATP and 2-NT vapor mixture for 3 hours, followed by degassing in vacuum. Subsequently, the sample was exposed to aqueous pH 2 solution to form the folded pattern.

Spectroscopy

UV−vis extinction spectra of nanoparticle solutions were obtained using a Shimadzu 1800 spectrophotometer. SERS maps were obtained using a confocal InVia Renishaw Raman microscope by collecting a 2D array of Raman spectra with a step size of 0.3 µm. Raman spectra of pATP adsorbed on Ag@AuNRs were collected using 785 nm laser as excitation source (0.07

mW power at the sample surface) and 50× objective with one accumulation and 0.1 s exposure time. Raman spectra of pATP and 2-NT adsorbed on AuNRs were collected using 785 nm laser as excitation source (0.7 mW power at the sample surface) and 50× objective with one accumulation and 0.4 s exposure time. Dark field scattering spectra were collected using a CytoViva Hyperspectral Imaging system with a spectral wavelength range of 420-900 nm and a spectral resolution of 2.8 nm. A 100x objective (NA: 0.90) was used to scan the surface with a 10 nm pixel size scan resolution and a 10 s integration time. Scattering spectra were normalized to a scan of a labsphere diffuse reflectance standard (SRS-99-010) to account for the differences in lamp intensity over the wavelength range. Over 10,000 individual point spectra were averaged for each of the pristine, stretched, and folded regions to obtain final composite spectra (Figure S5.3).

Microscopy

Transmission electron microscope (TEM) images were obtained using a field emission TEM (JEM-2100F, JEOL) at an accelerating voltage of 200 kV. Scanning electron microscope (SEM) images were obtained using a FEI Nova 2300 Field Emission SEM at an accelerating voltage of 10 kV. Atomic force microscopy (AFM) was performed using Dimension 3000 (Bruker) AFM in light tapping mode.[235, 236] Triangular Si cantilevers with tip radius less than 10 nm (MikroMasch) were employed for AFM imaging.

Electromagnetic Modelling

The modeling of the electromagnetic field distribution around a single Ag@AuNR, its dimer, and its trimer were performed using three-dimensional finite-difference time-domain (FDTD) simulations with commercially available software (EM Explorer).[237] FDTD simulations exploit the time and position dependence of Maxwell's equations to model electromagnetic waves in

rectangular 3D cells of finite volume called Yee cells. In a simulation domain of 500 nm × 300 nm × 300 nm, a single Ag@AuNR was modeled with an AuNR core with a length of 54 nm and diameter of 15 nm and an Ag cubical shell with an external length of 74 nm and width of 57 nm according to the dimensions measured from TEM images. Dimers and trimers are composed of two and three Ag@AuNR arranged along the polarization direction with a gap of 2 nm. Perfectly matched layer (PML) absorbing boundary conditions were applied in all directions. A high-resolution simulation (Yee cell size of 1 nm) was run at the excitation wavelength (λ = 785 nm) using p-polarized incident plane wave for illumination to obtain the electromagnetic field distribution. The complex refractive index of gold at this frequency was set to be $n = 0.18+i\ 4.96$ and silver was set to be $n = 0.03+i\ 5.46$,[238] and the refractive index of the surrounding medium was set to be 1.0 for air.

6.4 Results and Discussion

Spontaneous Folding of Plasmonic Gel

An ultrathin film of chemically-crosslinked poly(2-vinyl pyridine) (P2VP) was chosen as a responsive matrix. P2VP is a weak cationic polymer that exhibits a globule-coil transformation below a pH of 4 due to the protonation of the pyridine group.[239] It has been demonstrated that P2VP films exhibit spontaneous self-folding, involving large scale reorganization of the smooth film into lenticular structures, when exposed to acidic aqueous solutions.[234, 240] Here, we harness this mechanical instability to realize externally-triggered complex pattern of electromagnetic hotspots. The experimental approach involves the adsorption of a high density of plasmonic nanostructures onto an ultrathin P2VP film followed by chemisorption of Raman reporters (p-aminothiophenol) that enable the facile mapping of the electromagnetic hotspots. Subsequent exposure of the plasmonic gel to acidic aqueous solution is expected to result in a massive

reorganization of the film surface with a sparser distribution of the plasmonic nanostructures in some locations and folding-mediated electromagnetic hotspots in other locations. We have employed silver-coated gold nanorods (Ag@AuNRs) synthesized using a two-step seed-mediated method as plasmonic nanostructures. Gold nanorods (AuNRs), synthesized using a seed-mediated method, are employed as seeds for Ag@AuNRs.[190, 233] The length and diameter of AuNRs were respectively measured to be 53.5±3.9 and 14.8±2.5 nm using transmission electron microscopy (supporting information, Figure S5A). The thickness of the Ag shell can be finely tuned by controlling the concentration of seeds (*i.e.*, AuNRs) with respect to the Ag precursor concentration in the shell growth solution. The uniform growth of Ag shells on AuNRs resulted in rectangular prismatic structures with truncated rectangular/square cross sections, with a length of 74.3±4.6 nm and a width of 57.0±3.3 nm (Figure 6.1A). The extinction spectrum of AuNR cores exhibited two characteristic bands at 510 and 720 nm, corresponding to the transverse and longitudinal plasmon resonances respectively (Figure 6.1B). Following the deposition of a thin layer of Ag on the AuNRs, the bimetallic nanostructures exhibited four bands in the extinction spectrum. The extinction bands at 540 and 480 nm correspond to the longitudinal and transverse dipolar resonances and the extinction bands at 397 and 344 nm correspond to the transverse octupolar resonances of the Ag@AuNR. It has been demonstrated that the longitudinal dipolar resonance of the Ag@AuNR is highly sensitive to the aspect ratio of the AuNRs employed as cores and the optical properties can be finely tuned by controlling the aspect ratio of the AuNRs and the Ag shell thickness.[141, 142]

Ultrathin films of cross-linked P2VP were formed by spin-coating a silicon substrate with quaternized-P2VP from a mixed solvent comprised of nitromethane and tetrahydrofuran, followed by annealing at an elevated temperature to complete the cross-linking reaction (see

Experimental Section for details). Atomic force microscopy (AFM) scratch testing revealed the thickness of the cross-linked polymer film to be ~130 nm (Figure 6.1C). Following the surface modification of Ag@AuNRs with thiol-terminated poly(ethylene glycol) (SH-PEG), the nanostructures were adsorbed on the P2VP film. The pyridyl groups of P2VP are known to have high affinity to gold, resulting in strong adsorption of Au nanostructures to P2VP gel films.[96] Furthermore, the strong interaction between metal (Au and Ag) and iodide (I^-) of the quaternized P2VP also facilitates the chemisorption of Au nanostructures on the gel film.[241] AFM imaging revealed a highly uniform monolayer of Ag@AuNRs on the P2VP film. The AFM cross-section indicates that the dimensions of the Ag@AuNRs adsorbed on P2VP film closely matched with the dimensions obtained from TEM images (Figure 6.1D). Most of the nanostructures adsorbed on the film were found to be individual nanoparticles or linear clusters with no large scale aggregation or patchiness (Figure 6.1E, S5.1B).

As briefly mentioned above, upon exposure to acidic aqueous solution, cross-linked P2VP films transform from the initial smooth morphology into a network of folds, the dimensions of which are governed by the thickness of the film.[240] The bright-field optical image of the pristine P2VP film exposed to a solution with a pH of 2 reveals the lenticular structures as reported previously (Figure 6.2A). Fast Fourier transform (FFT) of the bright field image exhibits a diffuse ring, indicating the broad size distribution and random orientation of the folds, which can be harnessed to realize unclonable optical tags as described below (Inset of Figure 6.2A). The sharp edges of these folds stand out in the dark-field image owing to the strong light scattering from these polymer edges (Figure 6.2B). AFM characterization reveals regions with three distinct thicknesses that correspond to the stretched base layer tethered to the substrate (thickness of ~35 nm), a single folded region (~165 nm thick), and a region corresponding to double folds (~360

nm thick) (Figure 6.2C). Exposure of P2VP films uniformly adsorbed with Ag@AuNRs resulted in similar lenticular folding patterns (Figure 6.2D). It is worth noting that the adsorption of Ag@AuNRs on the polymer surface does not interfere with the swelling or folding of the ultrathin gel. The large-scale reorganization of the plasmonic gel with an external trigger suggests the strong interactions of the Ag@AuNRs with P2VP even in the highly swollen state of the polymer matrix. The dark-field image reveals strong light scattering from the interior of the folds as opposed to the pristine film in which light scattering was confined to edges (Figure 6.2E). The larger scattering from the interior of the folded regions is due to the high density of plasmonic nanostructures in the folded regions as will be discussed in detail below. Compared to the thickness of the folds in the pristine films, the thickness of the folds in Ag@AuNRs-coated films was found to be higher due to the presence of the additional layers of nanostructures trapped within the folds (Figure 6.2F). For example, in the single folded regions, both of the interior surfaces of folds are coated with plasmonic nanostructures, making the thickness of the single-fold in the plasmonic gel films one particle layer thicker (~60 nm) compared to that in the pristine films.

Spontaneous Folding-induced Electromagnetic Hotspots

Now we turn our attention to the formation of electromagnetic hotspots due to the swelling-induced folding of the P2VP films. Surface enhanced Raman scattering (SERS), which involves the dramatic enhancement of Raman signals from molecules adsorbed on or in proximity to plasmonic nanostructures, is being widely investigated for chemical and biological sensing and molecular bioimaging.[15, 26, 43, 86, 107, 119, 181, 183, 231, 242, 243] We employ SERS to monitor the formation of electromagnetic hotspots upon the folding of the P2VP films. As mentioned above, interstices between touching or closely spaced plasmonic nanostructures result in extremely large

electromagnetic field and SERS enhancements. Hence, SERS intensity mapping can provide a direct insight into the intensity, density, and distribution of electromagnetic hotspots in the folded structure. To obtain a SERS map, prior to exposing the films to acidic solution, Raman reporters were chemisorbed on the surface of nanostructures by exposing the Ag@AuNRs-coated films to p-aminothiophenol (pATP) vapor. A SERS intensity map was obtained from a representative location shown in the optical and AFM images (Figure 6.3A and 6.3B). The mapped region of the film is comprised of stretched layer, single fold, and double fold regions. The intensity map of the 1080 cm^{-1} band, corresponding to C-S stretching of pATP adsorbed on Ag@AuNRs, represents the spatial distribution of SERS activity of the folded plasmonic gel film (Figure 6.3C, intensity scale: 50×10^3 counts/sec (CPS)).[231] The SERS intensity distribution closely matched the topology of the folding pattern of the gel film with the double folds exhibiting higher intensities compared to single folds, which in turn exhibit higher intensities compared to the stretched regions (representative spectra shown in Figure 6.3D). The height profile and SERS intensity along a representative line indicated in the AFM image and SERS intensity map show remarkable similarity (Figure 6.3E). The SERS intensity distribution of the folded film exhibits a trimodal distribution corresponding to the stretched base layer (0-300 CPS), single fold (mean intensity of 18×10^3 CPS), and double fold (mean intensity of 32×10^3 CPS) regions (Figure 6.3F). Whereas the number density of nanostructures in the folded regions is only 3 times higher compared to that in the stretched regions, the SERS intensity from the folded regions is nearly 60 times higher compared to that from the stretched regions. This indicates the formation of electromagnetic hotspots within the folded regions rather than the higher SERS intensity sprouting from the slightly higher density of nanostructures. On the other hand, a pristine P2VP film adsorbed with Ag@AuNRs exhibited uniform SERS activity with randomly

distributed high intensity regions corresponding to the accessible electromagnetic hotspots as discussed in detail below (Figure 6.3G, intensity scale: 50×10^3 CPS). The representative SERS spectra from two different regions of the pristine film exhibit significantly lower intensities compared to those obtained from the folded film (Figure 6.3H). The SERS intensity distribution of the unfolded sample exhibited a unimodal distribution with a mean intensity of around 500 CPS (Figure 6.3I).

Exposure of the plasmonic gel film to an acidic solution results in isotropic swelling of the film in the plane parallel to its surface, which induces an increase in the surface area of the film. Subsequent drying of the film results in lenticular fold patterns that induce an intimate contact of two surfaces adsorbed with plasmonic nanostructures, which results in the formation of electromagnetic hotspots (Figure 6.4A). The isotropic stretching of the film leads to a sparser distribution of the plasmonic nanostructures in the stretched regions of the folded film compared to the pristine film (Figure 6.4B, S5.1C). On the other hand, in the single fold regions, SEM images reveal two distinct layers of nanostructures; a sparse layer of nanostructures at the top and a denser layer of coupled nanostructures resulting from the contact between two surfaces in the folds (Figure 6.4C).

Dark-field scattering spectra obtained from the pristine film depict two strong bands at 510 nm and 720 nm (Figure 6.4D). The strong band at 720 nm corresponding to the plasmon coupling between the Ag@AuNRs stems from the densely packed nanostructures on the P2VP film. Stretched regions of the folded film exhibited a weak scattering band at 510 nm corresponding to the sparsely distributed individual nanostructures in these locations. On the other hand, spectra obtained from single fold exhibit plasmon bands corresponding to the individual and coupled plasmon modes at 510 nm and 720 nm, respectively. The intensity of the coupled mode at 720

nm in the folded regions is significantly stronger compared to that in the stretched regions and weaker compared to that in the pristine film. It is known that assembly or controlled aggregation of plasmonic nanostructures results in the formation of electromagnetic hotspots that provide large SERS enhancements. The larger SERS activity of the folded regions (both single and double folds) can be ascribed to the formation of electromagnetic hotspots during the folding process. The stronger coupled plasmon mode in the scattering spectra of folded regions compared to the stretched regions confirms the electromagnetic hotspot-mediated SERS activity in these regions. It is interesting to note that the SERS activity of the pristine film is significantly lower compared to folded regions despite the presence of a high density and lightly clustered nanostructures on the film, as evidenced by the statistical analysis of nanoparticle distribution on different regions and the strong plasmon coupling band in the scattering spectra (Supp. The poor SERS activity of the pristine film can be explained by the limited access of the reporter molecules (pATP) into the electromagnetic hotspots formed between the closely spaced nanostructures. On the other hand, folding of the film results in clustering of nanostructures pre-adsorbed with pATP, which causes the Raman reporters to be trapped in the electromagnetic hotspots. The formation of electromagnetic hotspots after analyte adsorption is known to be more effective for SERS enhancement compared to adsorption of analytes in pre-formed electromagnetic hotspots, which is in complete agreement with our observations here.[244]

We have employed finite-difference time-domain (FDTD) simulations to estimate the electromagnetic field enhancement of individual and assembled Ag@AuNRs nanostructures (Figure 6.4E).[237] While a variety of cluster configurations can be observed in the folded regions, we have chosen to compare the electromagentic field enhancement of individual nanostructures and face-to-face assembled dimer and trimer structures as representative examples (see

Experimental section for details). The maximum electric field intensity ($|E|^2$) enhancement at the surface of an individual Ag@AuNR was found to be at ~24 times the incident intensity. Owing to the presence of electromagnetic hotspots at the interstices, the maximum electric field intensity in the case of dimers and trimers of Ag@AuNRs (at interstitial sites along the polarization direction) was found to be nearly 200 and 680 times the incident intensity, respectively. Such large enhancement of electromagnetic field intensity in the clusters combined with the formation of clusters after analyte adsorption facilitates the large SERS activity from the folds.

Nondeterministic Physical Patterns as Anti-counterfeit Optical Tag

Now we consider the possibility of harnessing the spontaneous and nondeterministic fold patterns and the associated SERS-active patterns in a responsive polymer film to realize an unclonable optical tag for anti-counterfeiting applications. The spontaneous plasmonic gel folding process can be implemented on any surface that facilitates strong adherence of the pristine gel film. For example, the P2VP film can be deposited and subsequently triggered to fold on an oxygen-plasma treated poly(dimethyl siloxane) (PDMS) microdisk (Figure 6.5A). Such microtaggants can be easily incorporated into a variety of objects for protecting against duplication or counterfeiting. For demonstrating plasmonic gel-based anti-counterfeit taggants, we employed AuNRs rather than Ag@AuNRs as plasmonic nanostructures considering that the former exhibit higher chemical and environmental stability. For deploying the nondeterministic fold patterns as anti-counterfeit taggants, the local feature orientation of the folds in the master image are identified by calculating the intensity gradients in a gray scale image and are recorded as a series of vectors in the image (Figure 6.5B).[245] The vector map revealed high fidelity of the vector distribution and orientation along the boundary of the folds, including along sharp curves

(Figure 6.5C). Before investigating whether these nondeterministic fold patterns can function as unique identifiers, we tested the recovery robustness of the sample image after rotation and rescaling of the sample image with respect to the master image, which is likely to occur during the authentication process. By implementing the speed up robust features (SURF) algorithm, the sample image (outlined in Figure 6.5D) can be robustly recovered and matched to the master image even when the sample is significantly rescaled (0.3-3 times) and rotated (0-360°) with respect to the master image (Figure 6.5E). Such high recovery robustness provides large tolerance in the sampling process, relaxing the hardware requirements (resolution and magnification of the image acquisition device and the orientation) during the authentication process and making it suitable for resource-limited settings.

The uniqueness of the fold patterns was investigated by comparing 100 folds pattern images obtained from different locations, with approximately 1000 folds within each micrograph. After obtaining vector distribution maps of the micrographs in the pool, we calculated cross-correlation between the fold patterns of the micrographs by quantifying the percentage of the matched vector pairs. As shown in the cross-correlation map, the data points along the diagonal line represent the intracorrelation values with a mean value of 98.9% (Inset of Figure 6.5F). On the other hand, the data points representing intercorrelation values (all data points other than the ones along the diagonal) exhibit a very small cross-correlation value with a mean value of 11.9% (Inset in Figure 6.5F, perfect match is defined as 100%). The histogram of the cross-correlation values shows a clear separation between the intracorrelation and intercorrelation, making the fold patterns unique identifiers for anti-counterfeiting applications (Figure 6.5F).

Nondeterministic Chemical Patterns as Optical Tags

As discussed above, spontaneous folding of plasmonic gel results in the formation of electromagnetic hotspots within the folds that result in a unique SERS intensity distribution. Such unique patterns of SERS intensity can be employed as a second layer of authentication, making the plasmonic gel a multi-dimensional taggant (described below). SERS-based chemical patterns encoded into the folded plasmonic gel are orthogonal to the physical encoding, providing an additional layer of security. We have employed two Raman reporters to demonstrate SERS-based chemical encoding in the folded plasmonic gel. We expect the SERS intensity distribution of the two reporters to be different considering their stochastic distribution within the most intense electromagnetic hotspots formed during the folding process. It is known that the SERS signal in the electromagnetic hotspots is dominated by a single or a few molecules that reside in the "hottest" regions, which results in the possibility of a significant fraction of electromagnetic hotspots exhibiting a dominant SERS signal corresponding to one of the two Raman reporters employed.[152, 183]

Thus, we have employed pATP and 2-naphthalenethiol (2-NT) as Raman reporters, which were chemisorbed on AuNRs by exposing the plasmonic gel film to the saturated vapor mixture of pATP and 2-NT. Owing to the excellent spectral multiplexing ability of SERS, Raman bands of pATP and 2-NT can be easily distinguished (Figure S5.6). The most prominent peaks of 2-NT were observed at 1068 and 1381 cm^{-1}, which correspond to the C-H bend and ring stretch vibrations, respectively.[128] SERS intensity maps of pATP at Raman band 1179 cm^{-1} and 2-NT at Raman band 1381 cm^{-1} were obtained from the fold patterns as shown in the optical micrograph (Figure 6.6A-6.6C). While both SERS intensity maps share similarities in that the high intensity regions generally correspond to the folds, the SERS maps are not degenerate i.e., not duplicates in terms of intensity distribution. The differences in the SERS maps corresponding to the two

reporters can be easily visualized by the well-developed features in the intensity ratio map scaling from 0.1 to 2 (Figure 6.6D). To further illustrate the differences in the SERS intensity distribution of the two Raman reporters, three representative spectra corresponding to pATP-dominated (a"), 2-NT-dominated (c"), and pATP and 2-NT comparable (b") are shown in Figure 6E (locations identified in the intensity ratio map).

The unique patterns of the SERS intensity distributions corresponding to the two Raman reporters in the folded plasmonic gel film can be employed as chemical taggants as described below. Similar to bright field optical images, the features in the SERS intensity maps can be represented as vector map according to the procedure described above (Figure 6.6F and 6.6G). To demonstrate that the SERS maps of folded plasmonic gel are indeed unique chemical patterns, we calculated the cross-correlation between vector distributions of 32 SERS intensity maps collected from 16 different regions of fold patterns, comprised of 16 SERS intensity maps corresponding to the 1179 cm^{-1} band and 16 SERS intensity maps corresponding to the 1381 cm^{-1} band (Figure 6.6H). The high cross-correlation values with a mean value of 98.6% along the diagonal line of the cross-correlation map correspond to intracorrelation cases *i.e.*, correlation between maps corresponding to the same Raman reporter at the same location of the fold patterns. In contrast, the intercorrelation (all the other data points) of vector distribution of SERS intensity maps showed extremely low correlation (mean value of 17.2%). A histogram plotted from the cross-correlation map demonstrates a clear separation between the intracorrelation and intercorrelation cases, making this structure ideally suited for unique chemical encoding (Figure 6.6I).

To highlight the importance of chemical encoding on top of topographical encoding in the anticounterfeiting taggants, we demonstrate that the nondeterministically formed physical

patterns can be replicated with advanced techniques. For example, soft lithographic techniques such as nanoimprinting can be employed to replicate the nondeterministic lenticular patterns of the folded plasmonic gel or any other encoding solely based on topographical features (Supplementary Information, Figure S5.8). The bright-field optical micrograph of the master graphical pattern exhibits a strong color contrast between the folded and stretched regions due to differential thin film interference (Figure S5.8A). In contrast, although the replicated pattern preserved the physical features of the master, the color contrast in the optical micrograph is lower due to a smaller difference in the thickness of the imprinted polymer film in different locations (Figure S8B). Vector distribution of the master and replicated patterns showed a strong correlation with ~70% matching vectors (Inset of Figure S5.8A and inset of Figure S5.8B). Such high correlation values suggest that graphical tags, such as buckling and wrinkling patterns and randomly distributed nanowires, although nondeterministic, are still vulnerable to counterfeit attacks using advanced duplication methods.[226, 246]

On the other hand, the chemical patterns encoded into the folded film are virtually impossible to replicate. We obtained SERS maps following the adsorption of AuNRs on the replicated pattern and their exposure to saturated vapor mixture of pATP and 2-NT. AFM images revealed the uniform distribution of AuNRs on the lenticular patterns (Figure S5.8C and S5.8D). As expected, SERS intensity maps of the Raman band at 1179 cm^{-1} corresponding to pATP and the Raman band at 1381 cm^{-1} corresponding to 2-NT exhibited a uniform distribution of SERS intensity without any physical features (Figure S5.8E and Figure S5.9). Furthermore, the SERS intensity ratio maps of the 1179 cm^{-1} and 1381 cm^{-1} bands also showed uniform and featureless distributions due to the uniformly adsorbed nanostructures as opposed to the stochastic distribution of Raman reporters in the electromagnetic hotpots of the folded films (Figure S5.8F).

6.5 Conclusions

We have demonstrated spontaneous self-folding of a plasmonic gel, comprised of an ultrathin polymer film uniformly adsorbed with plasmonic nanostructures, in response to a pH change. The large scale reconfiguration of the responsive plasmonic gel into lenticular folding patterns under external chemical stimulus resulted in the formation of complex patterns of electromagnetic hotspots in the film. While most of the earlier studies involving the integration of responsive polymers with plasmonic nanostructures are limited to rather small changes in the distance between the plasmonic nanostructures with external stimuli, we demonstrated a massive reconstruction of the responsive gelatinous plamonic surface, resulting in pronounced changes in the density and distribution of nanostructures and their optical activity. We showed the folded plasmonic gel film composed of nondeterministic physical and chemical patterns can serve as an unclonable multidimensional anti-counterfeiting taggant. While any anti-counterfeit optical tag solely relying on graphical features can, in theory, be replicated, the integration of nondeterministic topography patterns with stochastic chemical patterns determined by the fine details of the nanoscale structure and distribution of molecules within such nanostructures makes the anti-counterfeiting approach suggested here unbreachable.

6.6 Supporting Information

Supporting Information for chapter 6 is provided in appendix 5.

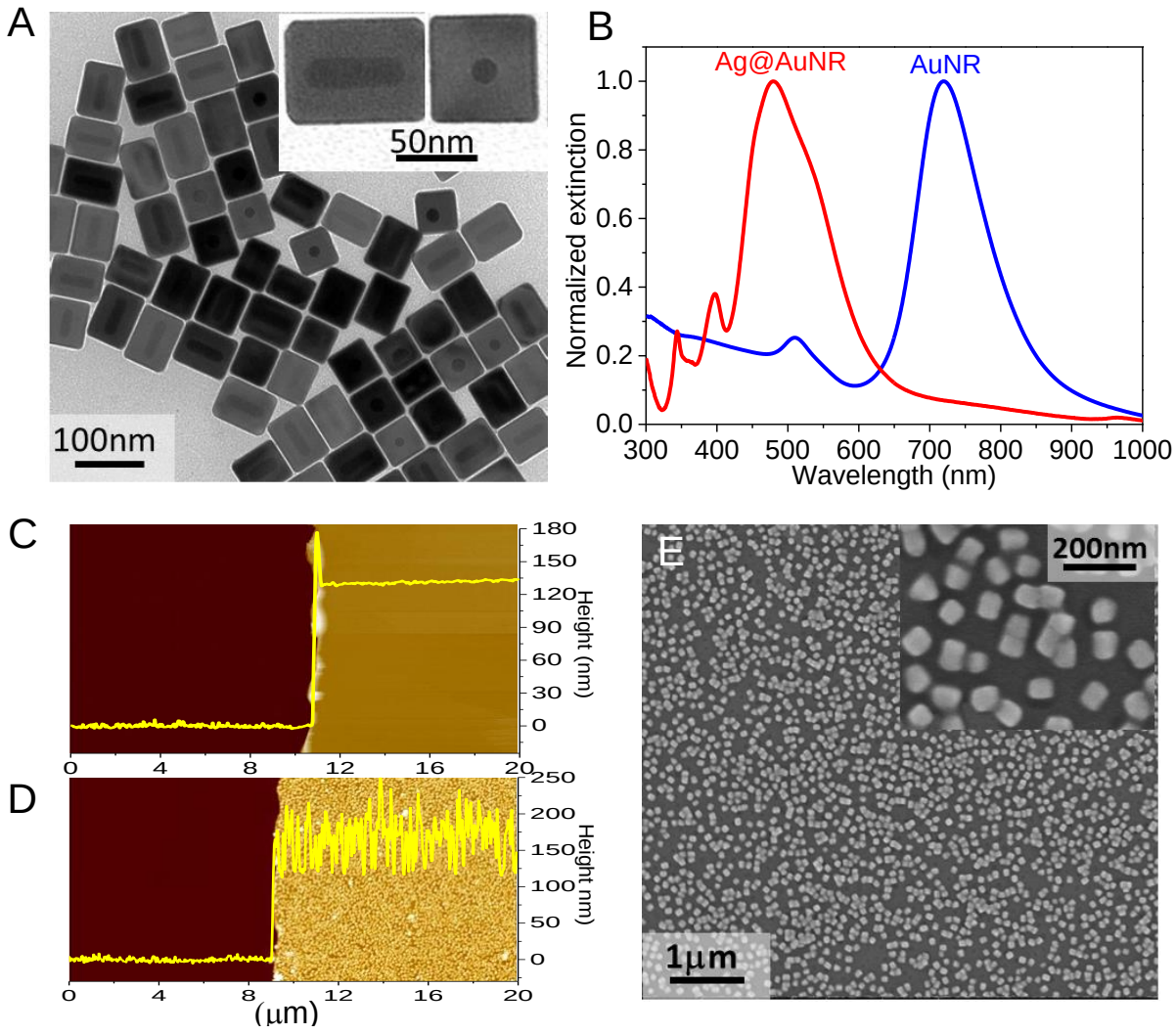

Figure 6. 1 (A) Representative TEM image of Ag coated Au nanorods (Ag@AuNRs). Inset shows higher magnification image of the nanostructures as viewed from the longitudinal and transverse directions. (B) Extinction spectra of AuNR and Ag@AuNR aqueous solutions. AFM image along the edge of an intentional scratch in (C) P2VP film and (D) P2VP film uniformly adsorbed with Ag@AuNRs. The representative height profile perpendicular to the scratch edge is shown in the image. (E) SEM image of P2VP film uniformly adsorbed with Ag@AuNRs showing the lightly clustered nanostructures on the film (inset shows a higher magnification image).

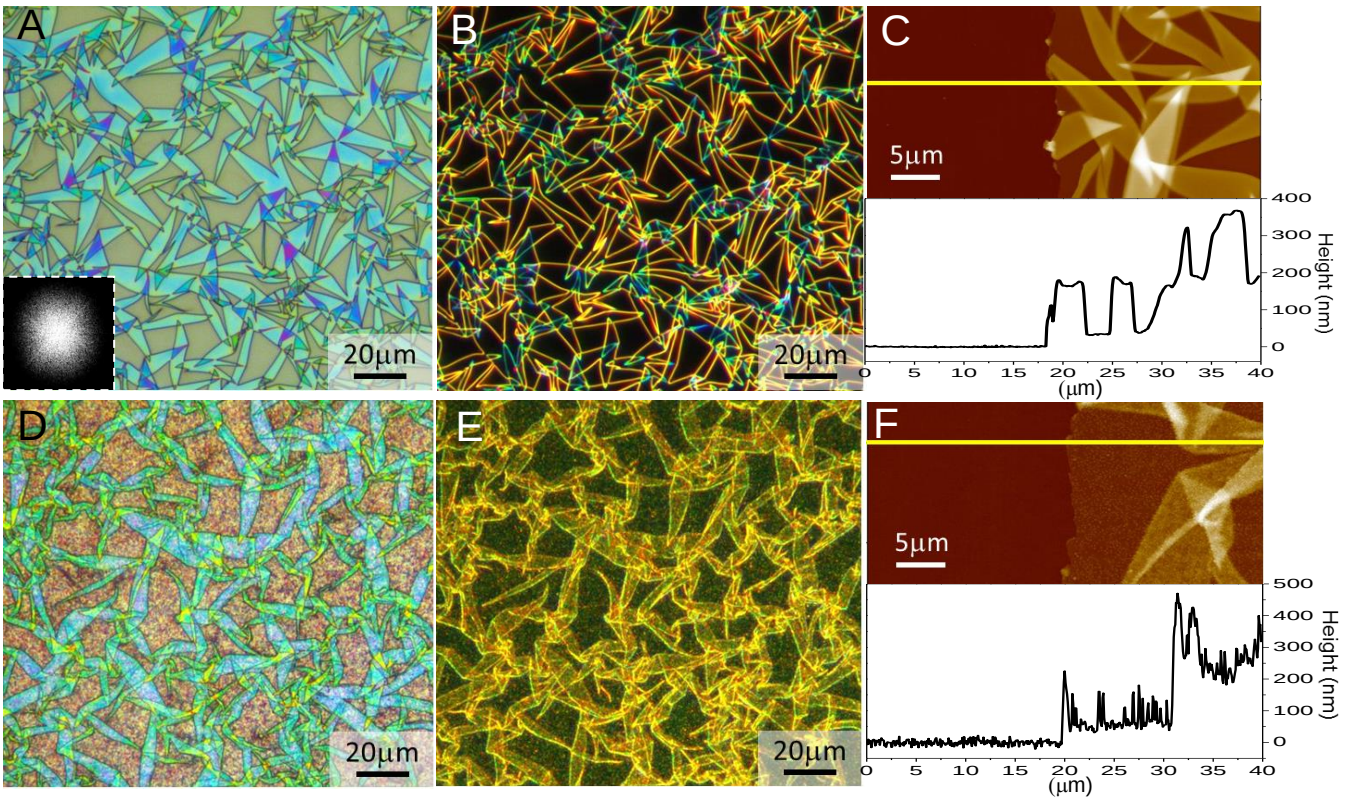

Figure 6. 2 (A) Bright-field and (B) dark-field (showing scattering from edges of folds) optical microscopy images of a P2VP film exposed to a pH 2 solution showing the lenticular pattern of folds. Inset of (A) shows the fast Fourier transform (FFT) of the bright-field image. (C) AFM image along the edge of an intentional scratch showing the three distinct regions corresponding to the stretched base layer, single folds and double folds. The height profile along the line shown in the image depicts the thickness of the three distinct regions. (D) Bright-field and (E) dark-field (showing plasmonic scattering from nanoparticles in the folded regions) optical microscopy images of P2VP film adsorbed with Ag@AuNRs upon exposure to pH 2 solution showing the lenticular folding pattern. (F) AFM image along the edge of an intentional scratch in P2VP film adsorbed with Ag@AuNRs showing the three distinct regions corresponding to the stretched base layer, single folds and double folds. The height profile along the line shown in the image depicts the thickness of the three distinct regions.

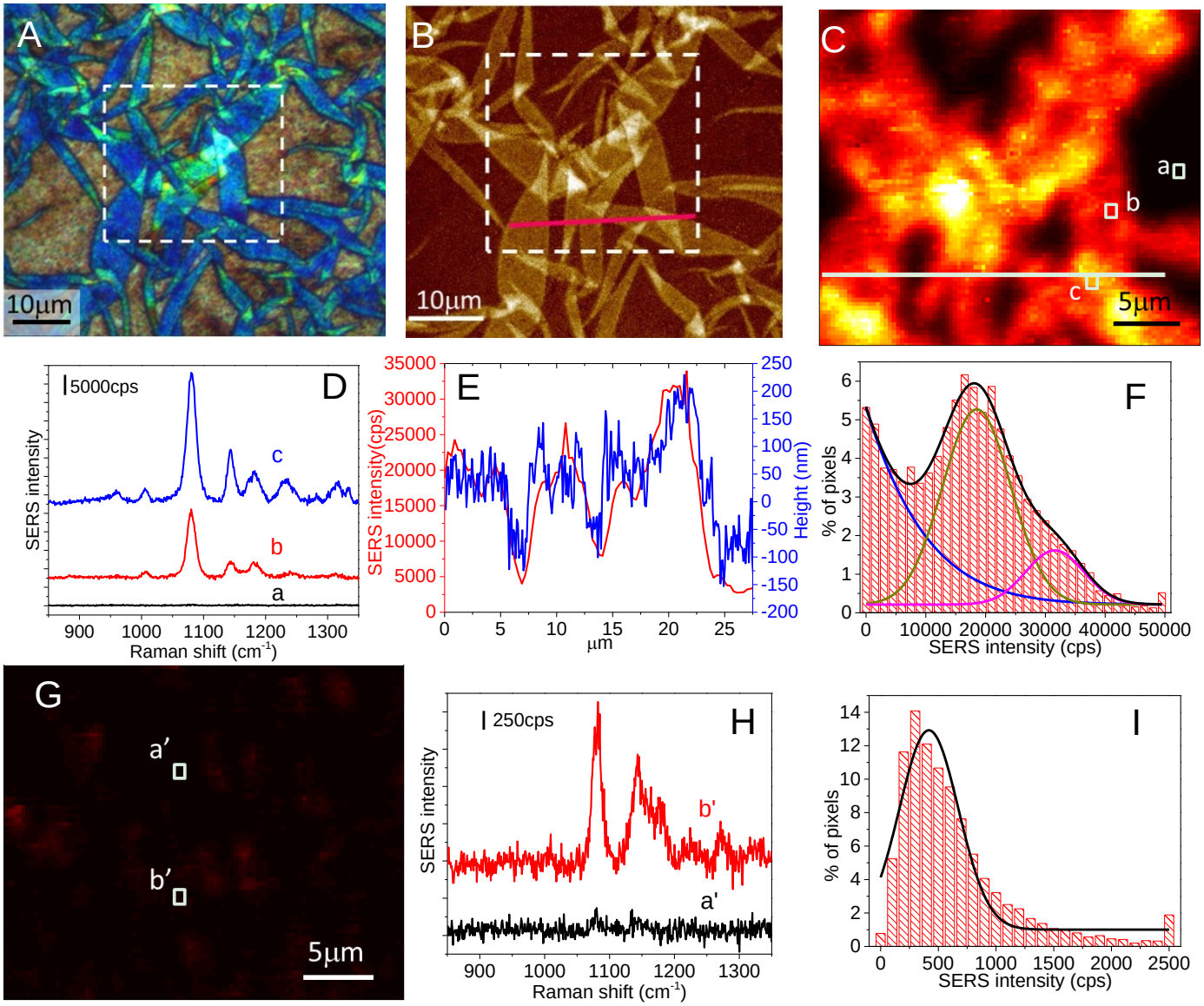

Figure 6. 3 (A) Optical and (B) AFM images showing the region from which SERS intensity map (C) was obtained. SERS intensity map (intensity scale: 50×10^3 CPS) in (C) shows a lenticular pattern that is remarkably similar to the lenticular pattern in the AFM height image in (B). The squares in the optical (A) and AFM (B) images correspond to the mapped region shown in (C). (D) Representative SERS spectra from three regions marked in the SERS map shown in (C). (E) Height and corresponding SERS intensity profile along a line shown in the AFM image and a SERS map depicting the remarkable similarity of the cross-sectional profiles.

(F) Histogram of the SERS intensity of the folded film showing a trimodal distribution corresponding to a stretched layer, single folds, and double folds. (G) SERS intensity map (intensity scale: 50×10^3 CPS) from a pristine film, showing significantly lower intensity compared to that from a folded film (SERS intensity with smaller intensity scale shown in Figure S5.2). (H) Representative SERS spectra from two regions marked in the SERS map shown in (G). (I) Histogram of the SERS intensity of the pristine film showing a unimodal distribution, which is in stark contrast to that of the folded film.

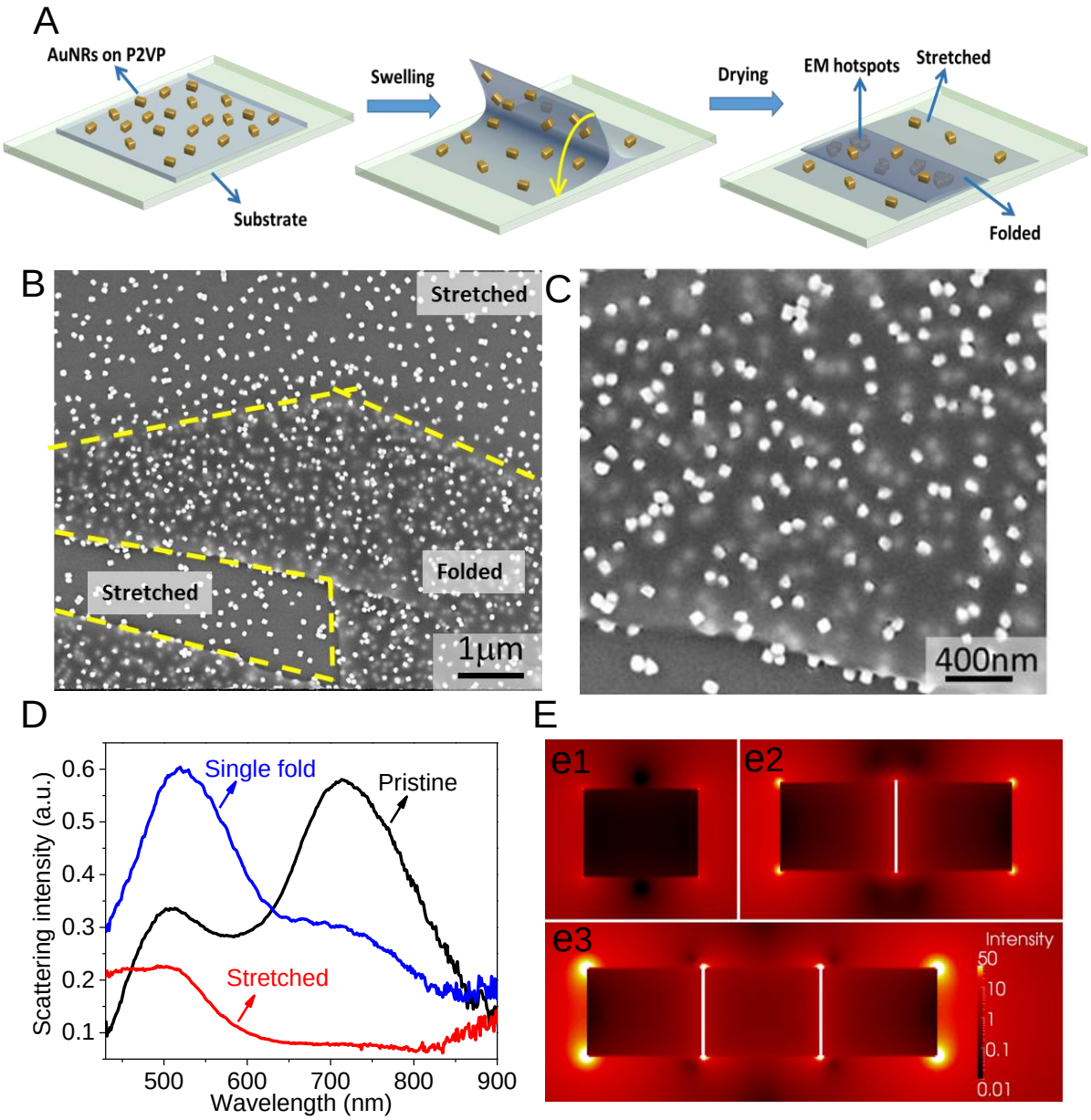

Figure 6. 4 (A) Schematic illustration showing the reorganization of the nanostructures adsorbed on the plasmonic gel during the swelling-mediated folding process. (B) SEM image of the folded film showing a sparser distribution of the nanostructures in the stretched regions compared to pristine film and multilayers of nanostructures in the folded regions. (C) Higher magnification SEM image of the folded region showing the lightly clustered nanostructures in the interior of the folds, which serve as SERS-active EM hotspots. (D) Scattering spectra obtained from pristine

film and folded film (stretched and single fold regions). (E) FDTD simulations showing the EM field intensity around individual, dimer, and trimer Ag@AuNR structures.

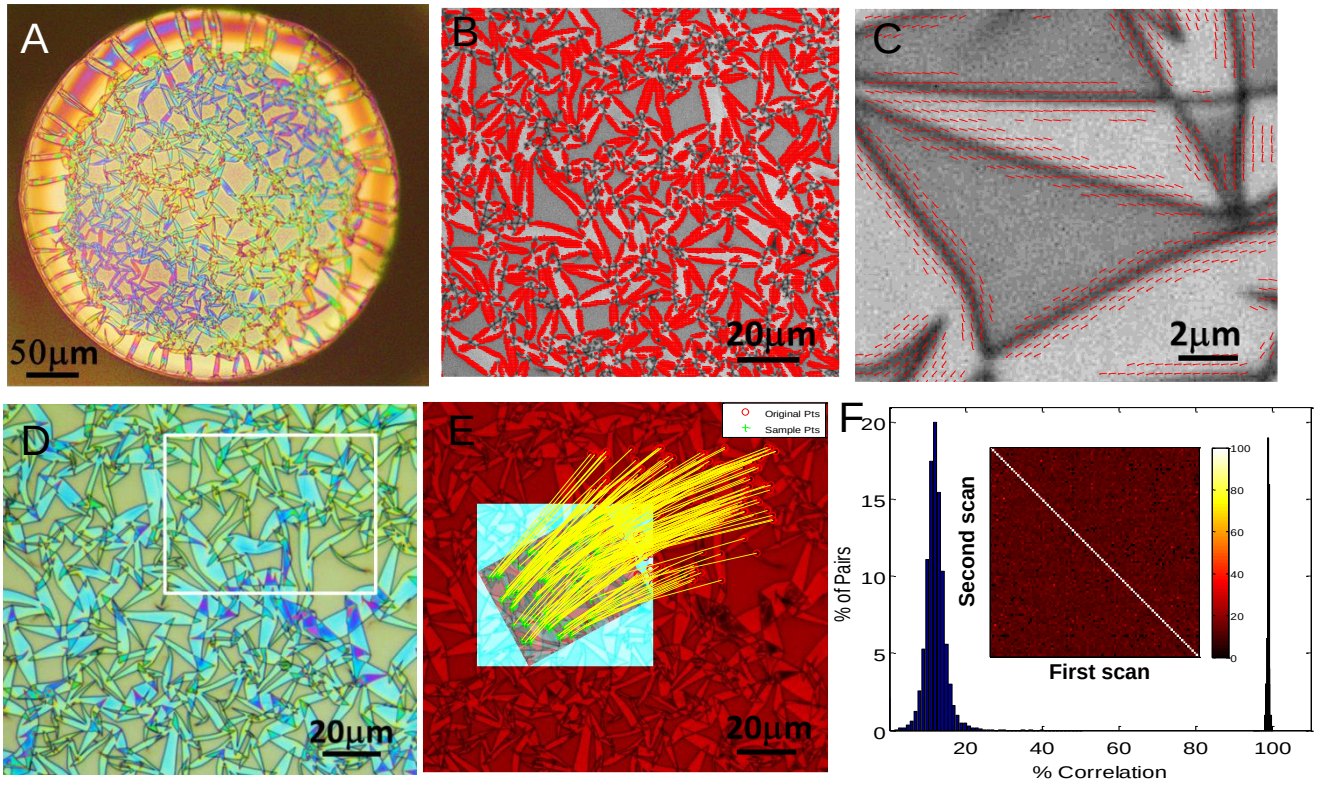

Figure 6. 5 (A) Optical image of a multidimensional microtaggant comprised of folded plasmonic gel on a PDMS microdisk. (B) Vector distribution map obtained from a grey scale image of the fold patterns. (C) Magnified vector distribution image showing highly fidelity of the vector distribution and orientation with the boundary of the folds. (D) A representative bright-field optical micrograph of folded plasmonic gel as an original image. The part of the image within the white outline is rotated and rescaled to demonstrate the authentication process. (E) Recovery of the sample image (rotated and rescaled image shown in white outline of (D)) by mapping the speeded up robust features (SURF) of the sample image to the original image. (F) Histogram showing the distribution of cross-correlation values obtained by comparing the vector distribution maps of 100 micrographs of fold patterns obtained from different locations. Corresponding heat map of the cross-correlation is shown as inset. The data points along the diagonal line of cross-correlation map represent intracorrelation calculations with a mean value

of 98.9%, while the others represent intercorrelation calculations with a mean value of 11.9% (perfect match is defined as 100%).

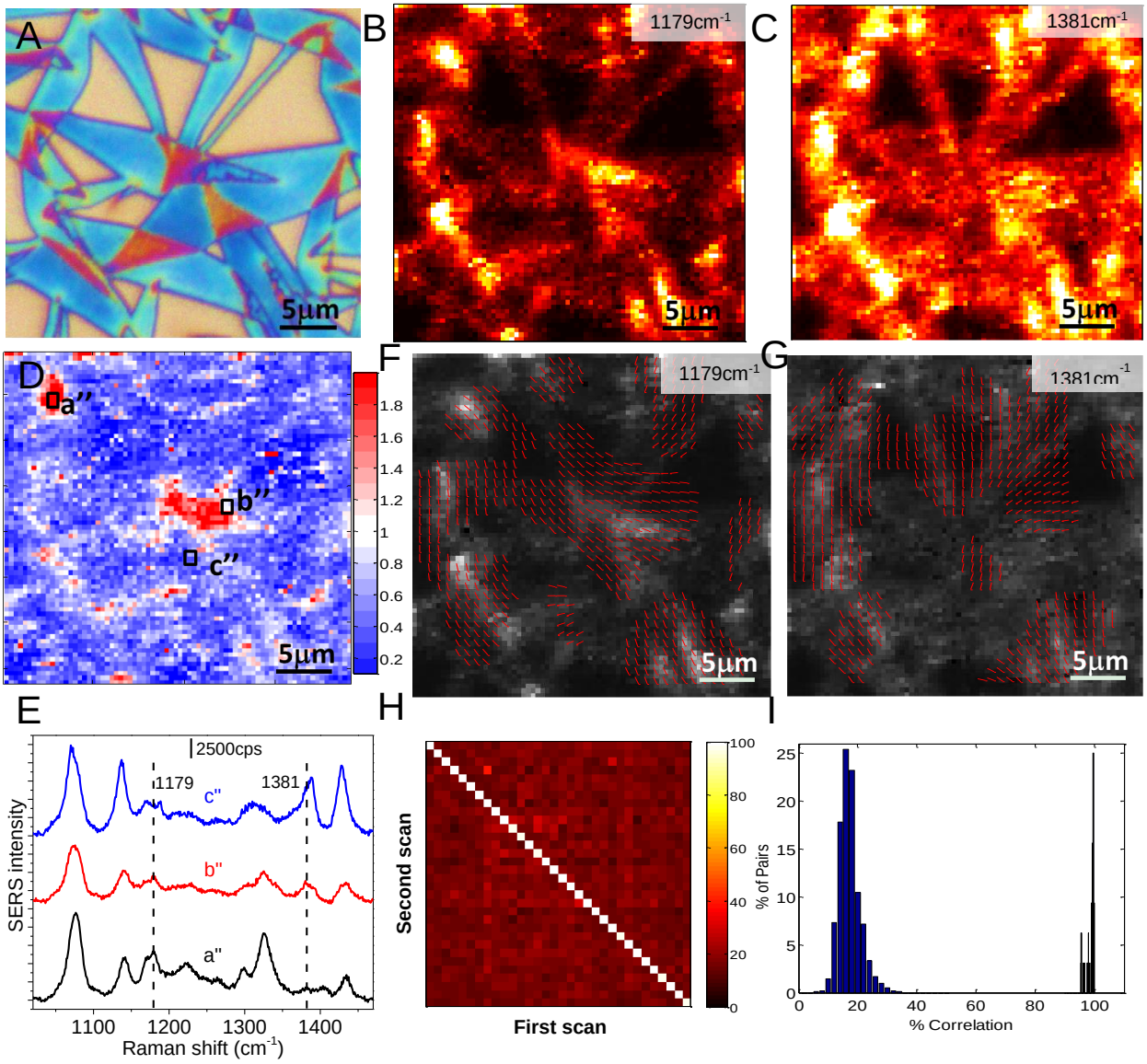

Figure 6. 6 (A) Optical image showing the region from which SERS intensity maps of (B) pATP at Raman band 1179 cm^{-1} and (C) 2-NT at Raman band 1381 cm^{-1} were collected. SERS map intensity scale: 5×10^3 CPS. (D) SERS intensity ratio map of 1179 cm^{-1}/1381 cm^{-1} showing a well-developed 2D map indicating a high level of spectral encoding owing to the two Raman reporters. (E) Representative SERS spectra from three regions marked in the SERS intensity ratio map shown in (D) showing the location-dependent intensity ratio of the two Raman bands corresponding to pATP and 2-NT. (F), (G) Vector distribution maps obtained from normalized

grayscale SERS intensity maps shown in (B) and (C) respectively. (H) Heat map showing the cross-correlation values obtained by comparing the vector distribution maps of 32 SERS intensity maps (16 SERS intensity maps at Raman band 1179 cm^{-1} and 16 SERS intensity maps at Raman band 1381 cm^{-1}) collected from different regions of fold patterns. The data points along the diagonal line of cross-correlation map represent intracorrelation calculations with a mean value of 98.6%, while the others represent intercorrelation calculations with a mean value of 17.2% with a narrow distribution (perfect match is defined as 100%). (I) Histogram showing the distribution of cross-correlation values obtained from the heat map shown in (H).

Chapter 7: Conclusions

7.1 Conclusions

Owing to the higher surface to volume ratio and facile tunability of LSPR wavelength over a broad range from visible to parts of near infrared, hollow and porous metal nanostructures exhibit extraordinary optical and catalytic properties compared to their solid counterparts. In the work presented in this dissertation, we designed and demonstrated a novel class of hollow and porous plasmonic nanostructures for highly efficient detection of trace amounts of chemical and biological analytes based on the localized surface plasmon resonance (LSPR) and surface enhanced Raman scattering (SERS). We have successfully demonstrated the synthesis of hollow and porous metal nanostructures of different sizes and shapes through a combination of template-mediated synthesis and galvanic replacement reaction.

We have demonstrated Au nanocages (AuNCs) exhibit significantly higher refractive index sensitivity and lower electromagnetic decay length, both of which make it an excellent candidate for plasmonic biosensing. AuNCs with built-in artificial antibodies achieved by molecular imprinting approach enabled the detection of a kidney injury biomarker (NGAL) down to a concentration of 25 ng/ml. The limit of detection achieved with AuNCs as nanotransducers is more than an order of magnitude lower compared to that obtained with Au nanorods (AuNRs). In addition to the excellent sensitivity, AuNCs with built-in artificial antibodies for neutrophil gelatinase-associated lipocalin (NGAL) exhibit excellent selectivity against numerous interfering urinary proteins and remarkable stability across pH ranging from 4.5 to 8.5 and specific gravities from 1.005 to 1.030. AuNCs with built-in artificial antibodies can be potentially employed for

rapid urinalysis in point-of-care settings for identifying patients that can progress to acute kidney injury (AKI), allowing early therapeutic intervention.

We have also investigated the influence of size, shape, polarization, and structure of plasmonic nanostructures on the SERS activity. Within the size range studied, the SERS activity of the plasmonic nanorattles with spherical cores increased with the increase in the edge length. The increase in the SERS activity of the cubic nanorattles is due to the increase in the extinction (and scattering) coefficient of nanostructures with size. On the other hand, the SERS activity of the plasmonic nanorattles with nanorod cores decreased with the increase in the edge length of the porous cuboid shells. In the case of the cuboid nanorattles, the electromagnetic hotspot within the nanostructure, formed between the edge of the AuNR and porous Au shell, governs the SERS activity.

We have also investigated the polarization-dependent SERS properties of anisotropic plasmonic nanorttles. The SERS activity of Au nanorattles exhibited significantly different polarization-dependence compared to their solid counterparts i.e. AuNR@Ag nanocuboids. For the cuboidal nanorattles, the internal electromagnetic hotspot dominates the SERS activity of the nanorattles. Conversely, the nanocuboids exhibited a polarization-dependent SERS activity that is dominated by their sharp corners and edges, which is similar to most conventional anisotropic solid nanostructures. Furthermore, we have investigated the correlation between the extent of galvanic replacement and the SERS enhancement of plasmonic nanorattles. We synthesized plasmonic nanorattles comprised of 2-NT coated Au nanosphere as core and porous gold cube as a shell with different degrees of galvanic replacement using Au@Ag nanocubes as templates. The nanoscale structure, optical properties and SERS enhancement of Au nanorattles were found to be highly dependent on the extent of the galvanic replacement. The finite difference time

domain electromagnetic simulations were employed to understand the electromagnetic field intensity distribution and size-, shape-, polarization-, and structure-dependent SERS enhancement from the plasmonic nanostructures. Overall, the SERS intensity trend obtained from the FDTD simulations showed excellent agreement with our experimental results. Comprehensive understanding of the size-, shape-, polarization-, and structure-dependent SERS activity of this novel class of nanostructures can lead to the rational design and fabrication of highly efficient SERS substrates for chemical and biological sensing.

Finally, we demonstrated the spontaneous self-folding of a plasmonic gel, comprised of an ultrathin polymer film uniformly adsorbed with plasmonic nanostructures, in response to a pH change. The large-scale reconfiguration of the responsive plasmonic gel into lenticular folding patterns under external chemical stimulus resulted in the formation of complex patterns of electromagnetic hotspots within the folds. We demonstrated a massive reconstruction of the responsive gelatinous plasmonic surface, resulting in pronounced changes in the density and distribution of nanostructures and their optical activity. We showed the folded plasmonic gel film composed of nondeterministic physical and chemical patterns can serve as an unclonable multidimensional anti-counterfeiting taggant. The integration of nondeterministic topography patterns with stochastic chemical patterns determined by the fine details of the nanoscale structure and distribution of molecules within such nanostructures makes the anti-counterfeiting approach suggested here unbreachable.

The principles established in this study for the design of hollow and solid plasmonic nanostructures can have far reaching implications in the real-world applications of plasmonic nanostructures. Especially, hollow plasmonic nanostructures, if optimally designed, can

outperform some of the conventional solid nanostructures such as Au nanorods in chemical and biological sensing applications.

References

1. Maier, S. A. *Springer: New York* **2007,** 1st ed.
2. Ozbay, E. *Science* **2006,** 311, (5758), 189-193.
3. Nikolajsen, T.; Leosson, K.; Bozhevolnyi, S. I. *Applied Physics Letters* **2004,** 85, (24), 5833-5835.
4. Cai, W.; White, J. S.; Brongersma, M. L. *Nano Lett.* **2009,** 9, (12), 4403-4411.
5. Srituravanich, W.; Pan, L.; Wang, Y.; Sun, C.; Bogy, D. B.; Zhang, X. *Nat Nano* **2008,** 3, (12), 733-737.
6. Röntzsch, L.; Heinig, K.-H.; Schuller, J. A.; Brongersma, M. L. *Applied Physics Letters* **2007,** 90, (4), 044105.
7. Stenzel, O.; Stendal, A.; Voigtsberger, K.; von Borczyskowski, C. *Solar Energy Materials and Solar Cells* **1995,** 37, (3–4), 337-348.
8. Atwater, H. A.; Polman, A. *Nat Mater* **2010,** 9, (3), 205-213.
9. Anker, J. N.; Hall, W. P.; Lyandres, O.; Shah, N. C.; Zhao, J.; Van Duyne, R. P. *Nat Mater* **2008,** 7, (6), 442-453.
10. Dickerson, E. B.; Dreaden, E. C.; Huang, X.; El-Sayed, I. H.; Chu, H.; Pushpanketh, S.; McDonald, J. F.; El-Sayed, M. A. *Cancer Letters* 269, (1), 57-66.
11. Abbas, A.; Linman, M. J.; Cheng, Q. *Analytical Chemistry* **2011,** 83, (8), 3147-3152.
12. Rosi, N. L.; Mirkin, C. A. *Chemical Reviews* **2005,** 105, (4), 1547-1562.
13. Sepúlveda, B.; Angelomé, P. C.; Lechuga, L. M.; Liz-Marzán, L. M. *Nano Today* **2009,** 4, (3), 244-251.
14. Mayer, K. M.; Hafner, J. H. *Chemical Reviews* **2011,** 111, (6), 3828-3857.
15. Ko, H.; Singamaneni, S.; Tsukruk, V. V. *Small* **2008,** 4, (10), 1576-1599.
16. Homola, J. *Chemical Reviews* **2008,** 108, (2), 462-493.
17. Homola, J. *Analytical and Bioanalytical Chemistry* **2003,** 377, (3), 528-539.
18. Reinhard, B. M.; Siu, M.; Agarwal, H.; Alivisatos, A. P.; Liphardt, J. *Nano Lett.* **2005,** 5, (11), 2246-2252.
19. Zhang, D.-F.; Zhang, Q.; Niu, L.-Y.; Jiang, L.; Yin, P.-G.; Guo, L. *J Nanopart Res* **2011,** 13, (9), 3923-3928.
20. Yap, F. L.; Thoniyot, P.; Krishnan, S.; Krishnamoorthy, S. *ACS Nano* **2012,** 6, (3), 2056-2070.
21. Haes, A. J.; Van Duyne, R. P. *J. Am. Chem. Soc.* **2002,** 124, (35), 10596-10604.
22. Riboh, J. C.; Haes, A. J.; McFarland, A. D.; Ranjit Yonzon, C.; Van Duyne, R. P. *J. Phys. Chem. B* **2003,** 107, (8), 1772-1780.
23. Yonzon, C. R.; Jeoung, E.; Zou, S.; Schatz, G. C.; Mrksich, M.; Van Duyne, R. P. *J. Am. Chem. Soc.* **2004,** 126, (39), 12669-12676.
24. Haes, A. J.; Chang, L.; Klein, W. L.; Van Duyne, R. P. *J. Am. Chem. Soc.* **2005,** 127, (7), 2264-2271.
25. Svedendahl, M.; Chen, S.; Dmitriev, A.; Käll, M. *Nano Lett.* **2009,** 9, (12), 4428-4433.
26. Nie, S.; Emory, S. R. *Science* **1997,** 275, (5303), 1102-1106.
27. Kathryn, M. M.; Feng, H.; Seunghyun, L.; Peter, N.; Jason, H. H. *Nanotechnology* **2010,** 21, (25), 255503.
28. Bingham, J. M.; Anker, J. N.; Kreno, L. E.; Van Duyne, R. P. *J. Am. Chem. Soc.* **2010,** 132, (49), 17358-17359.
29. Hall, W. P.; Modica, J.; Anker, J.; Lin, Y.; Mrksich, M.; Van Duyne, R. P. *Nano Lett.* **2011,** 11, (3), 1098-1105.
30. Novo, C.; Funston, A. M.; Gooding, A. K.; Mulvaney, P. *J. Am. Chem. Soc.* **2009,** 131, (41), 14664-14666.
31. Novo, C.; Funston, A. M.; Mulvaney, P. *Nat Nano* **2008,** 3, (10), 598-602.

32. Mathiowitz, E.; Jacob, J. S.; Jong, Y. S.; Carino, G. P.; Chickering, D. E.; Chaturvedi, P.; Santos, C. A.; Vijayaraghavan, K.; Montgomery, S.; Bassett, M.; Morrell, C. *Nature* **1997,** 386, (6623), 410-414.
33. McCreery, R. L., Raman Spectroscopy for Chemical Analysis. John Wiley & Sons, Inc.: 2005.
34. Jeanmaire, D. L.; Van Duyne, R. P. *Journal of Electroanalytical Chemistry and Interfacial Electrochemistry* **1977,** 84, (1), 1-20.
35. Fang, X.; Ahmad, S. R. *Appl. Phys. B* **2009,** 97, (3), 723-726.
36. Xu, H.; Aizpurua, J.; Käll, M.; Apell, P. *Physical Review E* **2000,** 62, (3), 4318-4324.
37. Xu, H.; Käll, M. *ChemPhysChem* **2003,** 4, (9), 1001-1005.
38. Su, K. H.; Wei, Q. H.; Zhang, X.; Mock, J. J.; Smith, D. R.; Schultz, S. *Nano Lett.* **2003,** 3, (8), 1087-1090.
39. Gunnarsson, L.; Rindzevicius, T.; Prikulis, J.; Kasemo, B.; Käll, M.; Zou, S.; Schatz, G. C. *J. Phys. Chem. B* **2005,** 109, (3), 1079-1087.
40. Jain, P. K.; Huang, W.; El-Sayed, M. A. *Nano Lett.* **2007,** 7, (7), 2080-2088.
41. Maier, S. A.; Brongersma, M. L.; Kik, P. G.; Atwater, H. A. *Phys. Rev. B* **2002,** 65, (19), 193408.
42. Huang, W.; Qian, W.; Jain, P. K.; El-Sayed, M. A. *Nano Lett.* **2007,** 7, (10), 3227-3234.
43. Camden, J. P.; Dieringer, J. A.; Zhao, J.; Van Duyne, R. P. *Accounts of Chemical Research* **2008,** 41, (12), 1653-1661.
44. Banholzer, M. J.; Millstone, J. E.; Qin, L.; Mirkin, C. A. *Chemical Society Reviews* **2008,** 37, (5), 885-897.
45. Im, H.; Bantz, K. C.; Lindquist, N. C.; Haynes, C. L.; Oh, S.-H. *Nano Lett.* **2010,** 10, (6), 2231-2236.
46. McFarland, A. D.; Young, M. A.; Dieringer, J. A.; Van Duyne, R. P. *J. Phys. Chem. B* **2005,** 109, (22), 11279-11285.
47. Tessier, P. M.; Velev, O. D.; Kalambur, A. T.; Lenhoff, A. M.; Rabolt, J. F.; Kaler, E. W. *Adv. Mater.* **2001,** 13, (6), 396-400.
48. Tao, A.; Kim, F.; Hess, C.; Goldberger, J.; He, R.; Sun, Y.; Xia, Y.; Yang, P. *Nano Lett.* **2003,** 3, (9), 1229-1233.
49. Qin, L.; Zou, S.; Xue, C.; Atkinson, A.; Schatz, G. C.; Mirkin, C. A. *Proceedings of the National Academy of Sciences* **2006,** 103, (36), 13300-13303.
50. Brolo, A. G.; Arctander, E.; Gordon, R.; Leathem, B.; Kavanagh, K. L. *Nano Lett.* **2004,** 4, (10), 2015-2018.
51. Ko, H.; Chang, S.; Tsukruk, V. V. *ACS Nano* **2009,** 3, (1), 181-188.
52. Chang, S.; Ko, H.; Singamaneni, S.; Gunawidjaja, R.; Tsukruk, V. V. *Analytical Chemistry* **2009,** 81, (14), 5740-5748.
53. Han, Y.; Oo, M. K.; Zhu, Y.; Sukhishvili, S.; Xiao, L.; Demokan, M. S.; Jin, W.; Du, H. In *Liquid-core photonic crystal fiber platform for raman scattering measurements of microliter analyte solutions*, 2007; pp 67670G-67670G-9.
54. Peer, D.; Karp, J. M.; Hong, S.; Farokhzad, O. C.; Margalit, R.; Langer, R. *Nat Nano* **2007,** 2, (12), 751-760.
55. Tian, L.; Gandra, N.; Singamaneni, S. *ACS Nano* **2013,** 7, (5), 4252-4260.
56. Chen, J.; Saeki, F.; Wiley, B. J.; Cang, H.; Cobb, M. J.; Li, Z.-Y.; Au, L.; Zhang, H.; Kimmey, M. B.; Li; Xia, Y. *Nano Lett.* **2005,** 5, (3), 473-477.
57. Cobley, C. M.; Campbell, D. J.; Xia, Y. *Adv. Mater.* **2008,** 20, (4), 748-752.
58. Tian, L.; Liu, K.-K.; Morrissey, J. J.; Gandra, N.; Kharasch, E. D.; Singamaneni, S. *Journal of Materials Chemistry B* **2014,** 2, (2), 167-170.
59. Xia, X.; Wang, Y.; Ruditskiy, A.; Xia, Y. *Adv. Mater.* **2013,** 25, (44), 6313-6333.
60. Liu, H. W.; Zhang, L.; Lang, X. Y.; Yamaguchi, Y.; Iwasaki, H. S.; Inouye, Y. S.; Xue, Q. K.; Chen, M. W. *Sci Rep-Uk* **2011,** 1.
61. Li, L.; Hutter, T.; Steiner, U.; Mahajan, S. *Analyst* **2013,** 138, (16), 4574-4578.

62. Le Ru, E. C.; Etchegoin, P. G. *Annu Rev Phys Chem* **2012,** 63, 65-87.
63. Lee, C. H.; Tian, L. M.; Abbas, A.; Kattumenu, R.; Singamaneni, S. *Nanotechnology* **2011,** 22, (27).
64. Gandra, N.; Abbas, A.; Tian, L.; Singamaneni, S. *Nano Lett.* **2012,** 12, (5), 2645-2651.
65. Ye, J.; Wen, F.; Sobhani, H.; Lassiter, J. B.; Dorpe, P. V.; Nordlander, P.; Halas, N. J. *Nano Lett.* **2012,** 12, (3), 1660-1667.
66. Li, Y.; Duan, G. T.; Liu, G. Q.; Cai, W. P. *Chemical Society Reviews* **2013,** 42, (8), 3614-3627.
67. Li, Y.; Koshizaki, N.; Wang, H. Q.; Shimizu, Y. *Acs Nano* **2011,** 5, (12), 9403-9412.
68. Gandra, N.; Singamaneni, S. *Adv. Mater.* **2013,** 25, (7), 1022-1027.
69. Murugan, R.; Kellum, J. A. *Nat Rev Nephrol* **2011,** 7, (4), 209-217.
70. Singbartl, K.; Kellum, J. A. *Kidney Int* **2012,** 81, (9), 819-825.
71. Bonventre, J. V.; Yang, L. *The Journal of Clinical Investigation* 121, (11), 4210-4221.
72. Hsu, R. K.; McCulloch, C. E.; Dudley, R. A.; Lo, L. J.; Hsu, C.-y. *Journal of the American Society of Nephrology* **2013,** 24, (1), 37-42.
73. Coca, S. G.; Yalavarthy, R.; Concato, J.; Parikh, C. R. *Kidney Int* **2007,** 73, (9), 1008-1016.
74. Haase, M.; Bellomo, R.; Devarajan, P.; Schlattmann, P.; Haase-Fielitz, A. *American Journal of Kidney Diseases* **2009,** 54, (6), 1012-1024.
75. Zimmerman, S. C.; Lemcoff, N. G. *Chemical Communications* **2004**, (1), 5-14.
76. Lassiter, J. B.; Sobhani, H.; Fan, J. A.; Kundu, J.; Capasso, F.; Nordlander, P.; Halas, N. J. *Nano Lett.* **2010,** 10, (8), 3184-3189.
77. Haes, A. J.; Van Duyne, R. P. *J. Am. Chem. Soc.* **2002,** 124, (35), 10596-10604.
78. Haes, A. J.; Chang, L.; Klein, W. L.; Van Duyne, R. P. *J. Am. Chem. Soc.* **2005,** 127, (7), 2264-2271.
79. Riboh, J. C.; Haes, A. J.; McFarland, A. D.; Ranjit Yonzon, C.; Van Duyne, R. P. *J. Phys. Chem. B* **2003,** 107, (8), 1772-1780.
80. Svedendahl, M.; Chen, S.; Dmitriev, A.; Käll, M. *Nano Lett.* **2009,** 9, (12), 4428-4433.
81. Yonzon, C. R.; Jeoung, E.; Zou, S.; Schatz, G. C.; Mrksich, M.; Van Duyne, R. P. *J. Am. Chem. Soc.* **2004,** 126, (39), 12669-12676.
82. Rosi, N. L.; Mirkin, C. A. *Chem. Rev.* **2005,** 105, (4), 1547-1562.
83. Mayer, K. M.; Hafner, J. H. *Chem. Rev.* **2011,** 111, (6), 3828-3857.
84. Maier, S. A.; Atwater, H. A. *J Appl Phys* **2005,** 98, (1).
85. Anker, J. N.; Hall, W. P.; Lyandres, O.; Shah, N. C.; Zhao, J.; Van Duyne, R. P. *Nat. Mater.* **2008,** 7, (6), 442-453.
86. Halas, N. J.; Lal, S.; Chang, W.-S.; Link, S.; Nordlander, P. *Chem. Rev.* **2011,** 111, (6), 3913-3961.
87. Xia, Y.; Li, W.; Cobley, C. M.; Chen, J.; Xia, X.; Zhang, Q.; Yang, M.; Cho, E. C.; Brown, P. K. *Acc. Chem. Res.* **2011,** 44, (10), 914-924.
88. Kim, C.; Cho, E. C.; Chen, J.; Song, K. H.; Au, L.; Favazza, C.; Zhang, Q.; Cobley, C. M.; Gao, F.; Xia, Y.; Wang, L. V. *ACS Nano* **2010,** 4, (8), 4559-4564.
89. Yang, X.; Skrabalak, S. E.; Li, Z.-Y.; Xia, Y.; Wang, L. V. *Nano Lett.* **2007,** 7, (12), 3798-3802.
90. Song, K. H.; Kim, C.; Cobley, C. M.; Xia, Y.; Wang, L. V. *Nano Lett.* **2008,** 9, (1), 183-188.
91. Wang, W.; Yan, T.; Cui, S.; Wan, J. *Chemical Communications* **2012,** 48, (82), 10228-10230.
92. Kwon, M. J.; Lee, J.; Wark, A. W.; Lee, H. J. *Analytical Chemistry* **2012,** 84, (3), 1702-1707.
93. Mahmoud, M. A.; El-Sayed, M. A. *J. Am. Chem. Soc.* **2010,** 132, (36), 12704-12710.
94. Sun, Y.; Xia, Y. *Anal. Chem.* **2002,** 74, (20), 5297-5305.
95. Skrabalak, S. E.; Au, L.; Li, X. D.; Xia, Y. N. *Nat. Protoc.* **2007,** 2, (9), 2182-2190.
96. Malynych, S.; Luzinov, I.; Chumanov, G. *J. Phys. Chem. B* **2002,** 106, (6), 1280-1285.
97. Tian, L. M.; Chen, E.; Gandra, N.; Abbas, A.; Singamaneni, S. *Langmuir* **2012,** 28, (50), 17435-17442.
98. Ansar, S. M.; Ameer, F. S.; Hu, W.; Zou, S.; Pittman, C. U.; Zhang, D. *Nano Lett.* **2013,** 13, (3), 1226-1229.

99. Mayer, K. M.; Lee, S.; Liao, H.; Rostro, B. C.; Fuentes, A.; Scully, P. T.; Nehl, C. L.; Hafner, J. H. *ACS Nano* **2008,** 2, (4), 687-692.
100. Chen, H.; Kou, X.; Yang, Z.; Ni, W.; Wang, J. *Langmuir* **2008,** 24, (10), 5233-5237.
101. Abbas, A.; Tian, L.; Morrissey, J. J.; Kharasch, E. D.; Singamaneni, S. *Advanced Functional Materials* **2013,** 23, (14), 1789-1797.
102. Chen, L.; Xu, S.; Li, J. *Chem. Soc. Rev.* **2011,** 40, (5), 2922-2942.
103. Shiomi, T.; Matsui, M.; Mizukami, F.; Sakaguchi, K. *Biomaterials* **2005,** 26, (27), 5564-5571.
104. Singer, E.; Elger, A.; Elitok, S.; Kettritz, R.; Nickolas, T. L.; Barasch, J.; Luft, F. C.; Schmidt-Ott, K. M. *Kidney Int.* **2011,** 80, (4), 405-414.
105. Koyner, J. L.; Parikh, C. R.; Consortium, T.-A. *J. Am. Soc. Nephrol.* **2012,** 23, (7), 1271-1271.
106. Freeman, R. G.; Grabar, K. C.; Allison, K. J.; Bright, R. M.; Davis, J. A.; Guthrie, A. P.; Hommer, M. B.; Jackson, M. A.; Smith, P. C.; Walter, D. G.; Natan, M. J. *Science* **1995,** 267, (5204), 1629-1632.
107. Campion, A.; Kambhampati, P. *Chemical Society Reviews* **1998,** 27, (4), 241-250.
108. Jarvis, R. M.; Goodacre, R. *Chemical Society Reviews* **2008,** 37, (5), 931-936.
109. Golightly, R. S.; Doering, W. E.; Natan, M. J. *ACS Nano* **2009,** 3, (10), 2859-2869.
110. Li, J.-M.; Yang, Y.; Qin, D. *J. Mater. Chem. C* **2014,** 2, (46), 9934-9940.
111. Katrin, K.; Harald, K.; Irving, I.; Ramachandra, R. D.; Michael, S. F. *Journal of Physics: Condensed Matter* **2002,** 14, (18), R597.
112. Schlücker, S. *Angew. Chem. Int. Ed.* **2014,** 53, (19), 4756-4795.
113. Vo-Dinh, T.; Wang, H.-N.; Scaffidi, J. *Journal of biophotonics* **2010,** 3, (0), 89-102.
114. Lee, C. H.; Tian, L.; Singamaneni, S. *ACS Applied Materials & Interfaces* **2010,** 2, (12), 3429-3435.
115. Lee, C. H.; Hankus, M. E.; Tian, L.; Pellegrino, P. M.; Singamaneni, S. *Analytical Chemistry* **2011,** 83, (23), 8953-8958.
116. Moskovits, M. *Journal of Raman Spectroscopy* **2005,** 36, (6-7), 485-496.
117. Hering, K.; Cialla, D.; Ackermann, K.; Dörfer, T.; Möller, R.; Schneidewind, H.; Mattheis, R.; Fritzsche, W.; Rösch, P.; Popp, J. *Analytical and Bioanalytical Chemistry* **2008,** 390, (1), 113-124.
118. Liu, H.; Zhang, L.; Lang, X.; Yamaguchi, Y.; Iwasaki, H.; Inouye, Y.; Xue, Q.; Chen, M. *Scientific Reports* **2011,** 1, 112.
119. Le Ru, E. C.; Etchegoin, P. G. *Annu. Rev. Phys. Chem.* **2012,** 63, (1), 65-87.
120. Yamamoto, Y. S.; Hasegawa, K.; Hasegawa, Y.; Takahashi, N.; Kitahama, Y.; Fukuoka, S.; Murase, N.; Baba, Y.; Ozaki, Y.; Itoh, T. *Phys. Chem. Chem. Phys.* **2013,** 15, (35), 14611-14615.
121. Maxwell, D. J.; Emory, S. R.; Nie, S. *Chem. Mater.* **2001,** 13, (3), 1082-1088.
122. Michaels, A. M.; Nirmal, M.; Brus, L. E. *J. Am. Chem. Soc.* **1999,** 121, (43), 9932-9939.
123. Chang, H. L.; Limei, T.; Abdennour, A.; Ramesh, K.; Srikanth, S. *Nanotechnology* **2011,** 22, (27), 275311.
124. Li, Y.; Duan, G.; Liu, G.; Cai, W. *Chemical Society Reviews* **2013,** 42, (8), 3614-3627.
125. Li, Y.; Koshizaki, N.; Wang, H.; Shimizu, Y. *ACS Nano* **2011,** 5, (12), 9403-9412.
126. Skrabalak, S. E.; Chen, J. Y.; Sun, Y. G.; Lu, X. M.; Au, L.; Cobley, C. M.; Xia, Y. N. *Accounts Chem Res* **2008,** 41, (12), 1587-1595.
127. Hirsch, L.; Gobin, A.; Lowery, A.; Tam, F.; Drezek, R.; Halas, N.; West, J. *Ann Biomed Eng* **2006,** 34, (1), 15-22.
128. Jaiswal, A.; Tian, L.; Tadepalli, S.; Liu, K.-k.; Fei, M.; Farrell, M. E.; Pellegrino, P. M.; Singamaneni, S. *Small* **2014,** 10, (21), 4287-4292.
129. Zhang, Q.; Cobley, C. M.; Zeng, J.; Wen, L.-P.; Chen, J.; Xia, Y. *J. Phys. Chem. C* **2010,** 114, (14), 6396-6400.
130. Chen, J.; Wiley, B.; McLellan, J.; Xiong, Y.; Li, Z.-Y.; Xia, Y. *Nano Lett.* **2005,** 5, (10), 2058-2062.
131. Ma, Y.; Li, W.; Cho, E. C.; Li, Z.; Yu, T.; Zeng, J.; Xie, Z.; Xia, Y. *ACS Nano* **2010,** 4, (11), 6725-6734.
132. Gole, A.; Murphy, C. J. *Langmuir* **2008,** 24, (1), 266-272.

133. Huang, X.; Neretina, S.; El-Sayed, M. A. *Adv. Mater.* **2009,** 21, (48), 4880-4910.
134. Zheng, Y.; Ma, Y.; Zeng, J.; Zhong, X.; Jin, M.; Li, Z.-Y.; Xia, Y. *Chemistry – An Asian Journal* **2013,** 8, (4), 792-799.
135. Wang, Y.; Zheng, Y.; Huang, C. Z.; Xia, Y. *J. Am. Chem. Soc.* **2013,** 135, (5), 1941-1951.
136. Sun, Y.; Mayers, B.; Xia, Y. *Adv. Mater.* **2003,** 15, (7-8), 641-646.
137. Gandra, N.; Portz, C.; Singamaneni, S. *Advanced Materials* **2014,** 26, (3), 350-350.
138. Au, L.; Lu, X.; Xia, Y. *Adv. Mater.* **2008,** 20, (13), 2517-2522.
139. Yang, Y.; Liu, J.; Fu, Z.-W.; Qin, D. *J. Am. Chem. Soc.* **2014,** 136, (23), 8153-8156.
140. Huang, X. H.; Neretina, S.; El-Sayed, M. A. *Advanced Materials* **2009,** 21, (48), 4880-4910.
141. Jiang, R.; Chen, H.; Shao, L.; Li, Q.; Wang, J. *Adv. Mater.* **2012,** 24, (35), OP200-OP207.
142. Okuno, Y.; Nishioka, K.; Kiya, A.; Nakashima, N.; Ishibashi, A.; Niidome, Y. *Nanoscale* **2010,** 2, (8), 1489-1493.
143. Xiang, Y.; Wu, X.; Liu, D.; Li, Z.; Chu, W.; Feng, L.; Zhang, K.; Zhou, W.; Xie, S. *Langmuir* **2008,** 24, (7), 3465-3470.
144. Fernanda Cardinal, M.; Rodríguez-González, B.; Alvarez-Puebla, R. A.; Pérez-Juste, J.; Liz-Marzán, L. M. *J. Phys. Chem. C* **2010,** 114, (23), 10417-10423.
145. de Silva, N.; Ha, J.-M.; Solovyov, A.; Nigra, M. M.; Ogino, I.; Yeh, S. W.; Durkin, K. A.; Katz, A. *Nat. Chem.* **2010,** 2, (12), 1062-1068.
146. Alvarez-Puebla, R. A.; Dos Santos Jr, D. S.; Aroca, R. F. *Analyst* **2004,** 129, (12), 1251-1256.
147. Chen, J.; Wiley, B.; Li, Z. Y.; Campbell, D.; Saeki, F.; Cang, H.; Au, L.; Lee, J.; Li, X.; Xia, Y. *Adv. Mater.* **2005,** 17, (18), 2255-2261.
148. Stiles, P. L.; Dieringer, J. A.; Shah, N. C.; Van Duyne, R. P. *Annual Review of Analytical Chemistry* **2008,** 1, (1), 601-626.
149. Itoh, T.; Iga, M.; Tamaru, H.; Yoshida, K.-i.; Biju, V.; Ishikawa, M. *J. Chem. Phys.* **2012,** 136, (2), 024703.
150. Kneipp, K.; Wang, Y.; Kneipp, H.; Perelman, L. T.; Itzkan, I.; Dasari, R. R.; Feld, M. S. *Phys. Rev. Lett.* **1997,** 78, (9), 1667-1670.
151. Kleinman, S. L.; Ringe, E.; Valley, N.; Wustholz, K. L.; Phillips, E.; Scheidt, K. A.; Schatz, G. C.; Van Duyne, R. P. *J. Am. Chem. Soc.* **2011,** 133, (11), 4115-4122.
152. Fang, Y.; Seong, N.-H.; Dlott, D. D. *Science* **2008,** 321, (5887), 388-392.
153. Tian, L.; Fei, M.; Tadepalli, S.; Morrissey, J. J.; Kharasch, E. D.; Singamaneni, S. *Adv. Healthc. Mater* **2015,** 4, (10), 1502-1509.
154. Tian, L.; Tadepalli, S.; Fei, M.; Morrissey, J. J.; Kharasch, E. D.; Singamaneni, S. *Chem. Mater.* **2015,** 27, (16), 5678-5684.
155. Shen, W.; Lin, X.; Jiang, C.; Li, C.; Lin, H.; Huang, J.; Wang, S.; Liu, G.; Yan, X.; Zhong, Q.; Ren, B. *Angew. Chem. Int. Ed.* **2015,** 54, (25), 7308-7312.
156. Huang, X.; El-Sayed, I. H.; Qian, W.; El-Sayed, M. A. *J. Am. Chem. Soc.* **2006,** 128, (6), 2115-2120.
157. Gobin, A. M.; Lee, M. H.; Halas, N. J.; James, W. D.; Drezek, R. A.; West, J. L. *Nano Lett.* **2007,** 7, (7), 1929-1934.
158. Ke, H.; Wang, J.; Dai, Z.; Jin, Y.; Qu, E.; Xing, Z.; Guo, C.; Yue, X.; Liu, J. *Angew. Chem. Int. Ed.* **2011,** 123, (13), 3073-3077.
159. Gandra, N.; Portz, C.; Singamaneni, S. *Adv. Mater.* **2014,** 26, (3), 350-350.
160. Khalavka, Y.; Becker, J.; Sönnichsen, C. *J. Am. Chem. Soc.* **2009,** 131, (5), 1871-1875.
161. Liu, K.-K.; Tadepalli, S.; Tian, L.; Singamaneni, S. *Chem. Mater.* **2015,** 27, (15), 5261-5270.
162. Tao, J.; Lu, Y.; Chen, J.; Lu, D.; Chen, C.; Wang, P.; Ming, H. *Plasmonics* **2011,** 6, (4), 785-789.
163. Le Ru, E. C.; Grand, J.; Félidj, N.; Aubard, J.; Lévi, G.; Hohenau, A.; Krenn, J. R.; Blackie, E.; Etchegoin, P. G. *J. Phys. Chem. C* **2008,** 112, (22), 8117-8121.
164. McLellan, J. M.; Li, Z.-Y.; Siekkinen, A. R.; Xia, Y. *Nano Lett.* **2007,** 7, (4), 1013-1017.

165. Wiley, B. J.; Chen, Y.; McLellan, J. M.; Xiong, Y.; Li, Z.-Y.; Ginger, D.; Xia, Y. *Nano Lett.* **2007,** 7, (4), 1032-1036.
166. Etchegoin, P. G.; Galloway, C.; Le Ru, E. C. *Phys. Chem. Chem. Phys.* **2006,** 8, (22), 2624-2628.
167. Talley, C. E.; Jackson, J. B.; Oubre, C.; Grady, N. K.; Hollars, C. W.; Lane, S. M.; Huser, T. R.; Nordlander, P.; Halas, N. J. *Nano Lett.* **2005,** 5, (8), 1569-1574.
168. Mohanty, P.; Yoon, I.; Kang, T.; Seo, K.; Varadwaj, K. S. K.; Choi, W.; Park, Q. H.; Ahn, J. P.; Suh, Y. D.; Ihee, H.; Kim, B. *J. Am. Chem. Soc.* **2007,** 129, (31), 9576-9577.
169. Wei, H.; Hao, F.; Huang, Y.; Wang, W.; Nordlander, P.; Xu, H. *Nano Lett.* **2008,** 8, (8), 2497-2502.
170. Smith, J. G.; Yang, Q.; Jain, P. K. *Angew. Chem. Int. Ed.* **2014,** 53, (11), 2867-2872.
171. Draine, B. T.; Flatau, P. J. *J. Opt. Soc. Am. A* **1994,** 11, (4), 1491-1499.
172. Draine, B. T.; Flatau, P. J. *J. Opt. Soc. Am. A* **2008,** 25, (11), 2693-2703.
173. Flatau, P. J.; Draine, B. T. *Opt. Express* **2012,** 20, (2), 1247-1252.
174. Sobh, A. N.; White, S.; Smith, J.; Sobh, N.; Jain, P. K. https://nanohub.org/resources/ddaplus. *(DOI: 10.4231/D3MS3K292)* **2016**.
175. Johnson, P. B.; Christy, R. W. *Phys. Rev. B* **1972,** 6, (12), 4370-4379.
176. Jain, P. K.; Lee, K. S.; El-Sayed, I. H.; El-Sayed, M. A. *J. Phys. Chem. B* **2006,** 110, (14), 7238-7248.
177. Jain, P. K. *Ph.D Thesis* **2008**.
178. Hu, M.; Ghoshal, A.; Marquez, M.; Kik, P. G. *J. Phys. Chem. C* **2010,** 114, (16), 7509-7514.
179. Vo-Dinh, T.; Wang, H.-N.; Scaffidi, J. *Journal of biophotonics* **2010,** 3, (1-2), 89-102.
180. Lin, S.; Zhu, W.; Jin, Y.; Crozier, K. B. *Nano Lett.* **2013,** 13, (2), 559-563.
181. Kneipp, K.; Wang, Y.; Kneipp, H.; Perelman, L. T.; Itzkan, I.; Dasari, R. R.; Feld, M. S. *Phys. Rev. Lett.* **1997,** 78, (9), 1667-1670.
182. Le Ru, E. C.; Etchegoin, P. G. *Annu. Rev. Phys. Chem.* **2012,** 63, (1), 65-87.
183. Kleinman, S. L.; Ringe, E.; Valley, N.; Wustholz, K. L.; Phillips, E.; Scheidt, K. A.; Schatz, G. C.; Van Duyne, R. P. *J Am Chem Soc* **2011,** 133, (11), 4115-4122.
184. Fang, Y. *Science* **2008,** 322, (5909), 1790-1790.
185. Gandra, N.; Singamaneni, S. *Adv. Mater.* **2013,** 25, (7), 1022-1027.
186. Lim, D.-K.; Jeon, K.-S.; Hwang, J.-H.; Kim, H.; Kwon, S.; Suh, Y. D.; Nam, J.-M. *Nat Nano* **2011,** 6, (7), 452-460.
187. Yang, M.; Alvarez-Puebla, R. n.; Kim, H.-S.; Aldeanueva-Potel, P.; Liz-Marzán, L. M.; Kotov, N. A. *Nano Lett.* **2010,** 10, (10), 4013-4019.
188. Liu, K.-K.; Tadepalli, S.; Kumari, G.; Banerjee, P.; Tian, L.; Jain, P. K.; Singamaneni, S. *J. Phys. Chem. C* **2016,** 120, (30), 16899-16906.
189. Jana, N. R.; Gearheart, L.; Murphy, C. J. *J. Phys. Chem. B* **2001,** 105, (19), 4065-4067.
190. Nikoobakht, B.; El-Sayed, M. A. *Chem Mater* **2003,** 15, (10), 1957-1962.
191. Zheng, Y.; Zhong, X.; Li, Z.; Xia, Y. *Particle & Particle Systems Characterization* **2014,** 31, (2), 266-273.
192. Skrabalak, S. E.; Au, L.; Li, X.; Xia, Y. *Nat. Protocols* **2007,** 2, (9), 2182-2190.
193. Sun, Y.; Xia, Y. *J. Am. Chem. Soc.* **2004,** 126, (12), 3892-3901.
194. Xia, Y.; Li, W.; Cobley, C. M.; Chen, J.; Xia, X.; Zhang, Q.; Yang, M.; Cho, E. C.; Brown, P. K. *Accounts of Chemical Research* **2011,** 44, (10), 914-924.
195. da Silva, A. G. M.; Rodrigues, T. S.; Haigh, S. J.; Camargo, P. H. C. *Chemical Communications* **2017**.
196. Polavarapu, L.; Porta, A. L.; Novikov, S. M.; Coronado-Puchau, M.; Liz-Marzán, L. M. *Small* **2014,** 10, (15), 3064-3064.
197. Schmucker, A. L.; Tadepalli, S.; Liu, K.-K.; Sullivan, C. J.; Singamaneni, S.; Naik, R. R. *RSC Advances* **2016,** 6, (5), 4136-4144.
198. Tian, L.; Tadepalli, S.; Farrell, M. E.; Liu, K.-K.; Gandra, N.; Pellegrino, P. M.; Singamaneni, S. *J. Mater. Chem. C* **2014,** 2, (27), 5438-5446.

199. Hu, X.; Wang, T.; Wang, L.; Dong, S. *J. Phys. Chem. C* **2007,** 111, (19), 6962-6969.
200. Mao, Z.; Song, W.; Chen, L.; Ji, W.; Xue, X.; Ruan, W.; Li, Z.; Mao, H.; Ma, S.; Lombardi, J. R.; Zhao, B. *J. Phys. Chem. C* **2011,** 115, (37), 18378-18383.
201. Qiu, C.; Zhang, L.; Wang, H.; Jiang, C. *J. Phys. Chem. Lett.* **2012,** 3, (5), 651-657.
202. Pal, J.; Ganguly, M.; Dutta, S.; Mondal, C.; Negishi, Y.; Pal, T. *CrystEngComm* **2014,** 16, (5), 883-893.
203. Aksu, S.; Huang, M.; Artar, A.; Yanik, A. A.; Selvarasah, S.; Dokmeci, M. R.; Altug, H. *Adv. Mater.* **2011,** 23, (38), 4422-4430.
204. Kahraman, M.; Daggumati, P.; Kurtulus, O.; Seker, E.; Wachsmann-Hogiu, S. *Sci. Rep.* **2013,** 3.
205. Lee, C. H.; Tian, L.; Singamaneni, S. *ACS Appl. Mater. Interfaces.* **2010,** 2, (12), 3429-3435.
206. Nergiz, S. Z.; Singamaneni, S. *ACS Appl. Mater. Interfaces.* **2011,** 3, (4), 945-951.
207. Gandra, N.; Tian, L.; Nergiz, S. Z.; Singamaneni, S. *J. Nanosci. Lett.* **2014,** 4, 23.
208. Pryce, I. M.; Aydin, K.; Kelaita, Y. A.; Briggs, R. M.; Atwater, H. A. *Nano Letters* **2010,** 10, (10), 4222-4227.
209. Huang, F.; Baumberg, J. J. *Nano Letters* **2010,** 10, (5), 1787-1792.
210. Kang, H.; Heo, C.-J.; Jeon, H. C.; Lee, S. Y.; Yang, S.-M. *ACS Applied Materials & Interfaces* **2013,** 5, (11), 4569-4574.
211. Stuart, M. A. C.; Huck, W. T. S.; Genzer, J.; Muller, M.; Ober, C.; Stamm, M.; Sukhorukov, G. B.; Szleifer, I.; Tsukruk, V. V.; Urban, M.; Winnik, F.; Zauscher, S.; Luzinov, I.; Minko, S. *Nat Mater* **2010,** 9, (2), 101-113.
212. Luzinov, I.; Minko, S.; Tsukruk, V. V. *Prog. Polym. Sci.* **2004,** 29, (7), 635-698.
213. Tokarev, I.; Tokareva, I.; Minko, S. *Adv. Mater.* **2008,** 20, (14), 2730-2734.
214. Roiter, Y.; Minko, I.; Nykypanchuk, D.; Tokarev, I.; Minko, S. *Nanoscale* **2012,** 4, (1), 284-292.
215. Lupitskyy, R.; Motornov, M.; Minko, S. *Langmuir* **2008,** 24, (16), 8976-8980.
216. Chang, S.; Singamaneni, S.; Kharlampieva, E.; Young, S. L.; Tsukruk, V. V. *Macromolecules* **2009,** 42, (15), 5781-5785.
217. Gupta, M. K.; Chang, S.; Singamaneni, S.; Drummy, L. F.; Gunawidjaja, R.; Naik, R. R.; Tsukruk, V. V. *Small* **2011,** 7, (9), 1192-1198.
218. Qian, X.; Li, J.; Nie, S. *J. Am. Chem. Soc.* **2009,** 131, (22), 7540-7541.
219. Lu, Y.; Liu, G. L.; Lee, L. P. *Nano Lett.* **2005,** 5, (1), 5-9.
220. Geryak, R.; Geldmeier, J.; Wallace, K.; Tsukruk, V. V. *Nano Lett.* **2015**.
221. Na, J.-H.; Evans, A. A.; Bae, J.; Chiappelli, M. C.; Santangelo, C. D.; Lang, R. J.; Hull, T. C.; Hayward, R. C. *Adv. Mater.* **2015,** 27, (1), 79-85.
222. Schweikart, A.; Pazos-Perez, N.; Alvarez-Puebla, R. A.; Fery, A. *Soft Matter* **2011,** 7, (9), 4093-4100.
223. Hanske, C.; Tebbe, M.; Kuttner, C.; Bieber, V.; Tsukruk, V. V.; Chanana, M.; König, T. A. F.; Fery, A. *Nano Lett.* **2014,** 14, (12), 6863-6871.
224. Huang, C.; Lucas, B.; Vervaet, C.; Braeckmans, K.; Van Calenbergh, S.; Karalic, I.; Vandewoestyne, M.; Deforce, D.; Demeester, J.; De Smedt, S. C. *Adv. Mater.* **2010,** 22, (24), 2657-2662.
225. Han, S.; Bae, H. J.; Kim, J.; Shin, S.; Choi, S.-E.; Lee, S. H.; Kwon, S.; Park, W. *Adv. Mater.* **2012,** 24, (44), 5924-5929.
226. Bae, H. J.; Bae, S.; Park, C.; Han, S.; Kim, J.; Kim, L. N.; Kim, K.; Song, S.-H.; Park, W.; Kwon, S. *Adv. Mater.* **2015,** 27, (12), 2083-2089.
227. Braeckmans, K.; De Smedt, S. C.; Roelant, C.; Leblans, M.; Pauwels, R.; Demeester, J. *Nat Mater* **2003,** 2, (3), 169-173.
228. Lee, J.; Bisso, P. W.; Srinivas, R. L.; Kim, J. J.; Swiston, A. J.; Doyle, P. S. *Nat Mater* **2014,** 13, (5), 524-529.

229. Cui, Y.; Phang, I. Y.; Lee, Y. H.; Lee, M. R.; Zhang, Q.; Ling, X. Y. *Chem. Commun.* **2015,** 51, (25), 5363-5366.
230. You, M.; Zhong, J.; Hong, Y.; Duan, Z.; Lin, M.; Xu, F. *Nanoscale* **2015,** 7, (10), 4423-4431.
231. Gandra, N.; Abbas, A.; Tian, L. M.; Singamaneni, S. *Nano Letters* **2012,** 12, (5), 2645-2651.
232. Tian, L.; Fei, M.; Tadepalli, S.; Morrissey, J. J.; Kharasch, E. D.; Singamaneni, S. *Advanced Healthcare Materials* **2015**, n/a-n/a.
233. Jana, N. R.; Gearheart, L.; Murphy, C. J. *J Phys Chem B* **2001,** 105, (19), 4065-4067.
234. Singamaneni, S.; McConney, M. E.; Tsukruk, V. V. *Adv. Mater.* **2010,** 22, (11), 1263-1268.
235. McConney, M. E.; Singamaneni, S.; Tsukruk, V. V. *Polym. Rev.* **2010,** 50, (3), 235-286.
236. Tsukruk, V. V.; Singamaneni, S. *Scanning Probe Microscopy of Soft Matter: Fundamentals and Practices (Wiley-VCH)* **2012**.
237. Yee, K. S. *IEEE Trans. Antennas Propag.* 14, 302-307.
238. Palik, E. D., *Handbook of Optical Constantsof Solids*. MA: Academic: Boston, 1985.
239. Roiter, Y.; Minko, S. *J. Am. Chem. Soc.* **2005,** 127, (45), 15688-15689.
240. Singamaneni, S.; McConney, M. E.; Tsukruk, V. V. *ACS Nano* **2010,** 4, (4), 2327-2337.
241. Magnussen, O. M. *Chem. Rev.* **2002,** 102, (3), 679-726.
242. Anger, P.; Bharadwaj, P.; Novotny, L. *Phys Rev Lett* **2006,** 96, (11).
243. Neubrech, F.; Pucci, A.; Cornelius, T. W.; Karim, S.; Garcia-Etxarri, A.; Aizpurua, J. *Phys Rev Lett* **2008,** 101, (15).
244. Kim, A.; Ou, F. S.; Ohlberg, D. A. A.; Hu, M.; Williams, R. S.; Li, Z. *J. Am. Chem. Soc.* **2011,** 133, (21), 8234-8239.
245. Kovesi, P. http://www.csse.uwa.edu.au/~pk/research/matlabfns/#fingerprints.
246. Kim, J.; Yun, J. M.; Jung, J.; Song, H.; Kim, J.-B.; Ihee, H. *Nanotechnology* **2014,** 25, (15), 155303.
247. Haes, A. J.; Zou, S.; Schatz, G. C.; Van Duyne, R. P. *J. Phys. Chem. B* **2004,** 108, (22), 6961-6968.
248. Haes, A. J.; Zou, S.; Schatz, G. C.; Van Duyne, R. P. *J. Phys. Chem. B* **2003,** 108, (1), 109-116.
249. Whitney, A. V.; Elam, J. W.; Zou, S.; Zinovev, A. V.; Stair, P. C.; Schatz, G. C.; Van Duyne, R. P. *J. Phys. Chem. B* **2005,** 109, (43), 20522-20528.
250. Kedem, O.; Tesler, A. B.; Vaskevich, A.; Rubinstein, I. *Acs Nano* **2011,** 5, (2), 748-760.
251. Decher, G. *Science* **1997,** 277, (5330), 1232-1237.
252. Park, J.; Fouche, L. D.; Hammond, P. T. *Adv. Mater.* **2005,** 17, (21), 2575-+.
253. Antipov, A. A.; Sukhorukov, G. B.; Mohwald, H. *Langmuir* **2003,** 19, (6), 2444-2448.
254. Kharlampieva, E.; Kozlovskaya, V.; Chan, J.; Ankner, J. F.; Tsukruk, V. V. *Langmuir* **2009,** 25, (24), 14017-14024.
255. Tian, L. M.; Fei, M.; Kattumenu, R.; Abbas, A.; Singamaneni, S. *Nanotechnology* **2012,** 23, (25).
256. Nusz, G. J.; Curry, A. C.; Marinakos, S. M.; Wax, A.; Chilkoti, A. *Acs Nano* **2009,** 3, (4), 795-806.
257. Yoshida, K.-i.; Itoh, T.; Tamaru, H.; Biju, V.; Ishikawa, M.; Ozaki, Y. *Phys. Rev. B* **2010,** 81, (11), 115406.
258. Liu, X.; Atwater, M.; Wang, J.; Huo, Q. *Colloids and Surfaces B: Biointerfaces* **2007,** 58, (1), 3-7.
259. Near, R. D.; Hayden, S. C.; Hunter, R. E.; Thackston, D.; El-Sayed, M. A. *J. Phys. Chem. C* **2013,** 117, (45), 23950-23955.

Appendix

Appendix 1

EM decay length calculation

In addition to bulk refractive index sensitivity, EM decay length is yet another important parameter to maximize a LSPR transducer response, which describes the distance-dependent refractive index sensitivity and sensing depth for LSPR sensors.[247-249] We employed layer-by-layer (LbL) assembly of polyelectrolytes for probing the distance-dependent LSPR sensitivity and EM decay length of AuNCs and AuNRs. LbL assembly of polyelectrolyte multilayers (PEM), which involves the alternate adsorption of oppositely charged polyelectrolytes, offers an excellent control over the thickness of the dielectric layer down to ~ 1nm.[250-255] The spectra revealed a progressive red-shift in LSPR wavelength and increase in LSPR intensity with the deposition of each bilayer due to the increase in the refractive index of the medium surrounding the plasmonic nanostructures (from air to polymer layer) (Fig. S2C and Fig. S3B). The cumulative LSPR wavelength shift following the deposition of each polyelectrolyte layer for AuNCs is much higher than AuNRs, especially within the first few nanometers where biomolecule binding events occur (Fig. 2D).

Owing to the evanescent nature of the EM field at the surface of the plasmonic nanostructures, the LSPR wavelength shift exhibits a characteristic decay with increasing distance from the surface of the nanostructures (*i.e.* increasing number of layers), given by [85, 256]

$$R = m\Delta\eta\left(1 - \exp\left(-2d/l\right)\right)$$

Where R is LSPR shift, m is the refractive index sensitivity of nanostructures, $\Delta\eta$ is the change in the refractive index in RIU, d is the adsorbate layer thickness (thickness of the polyelectrolyte layer in this case) and l is the EM decay length.

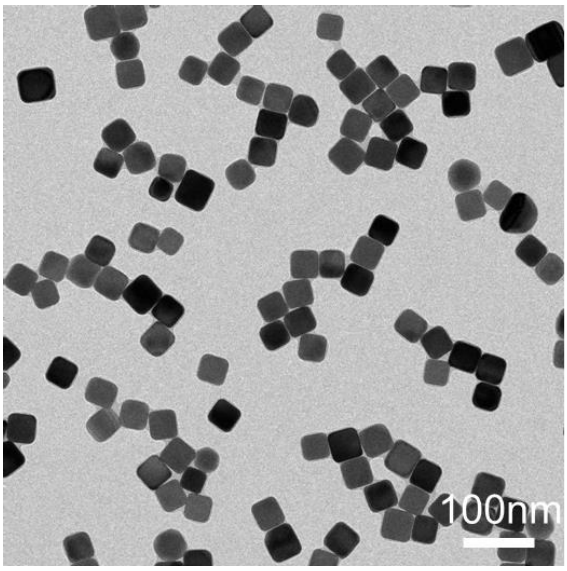

Figure S1. 1 TEM image of silver nanocubes as template for gold nanocages.

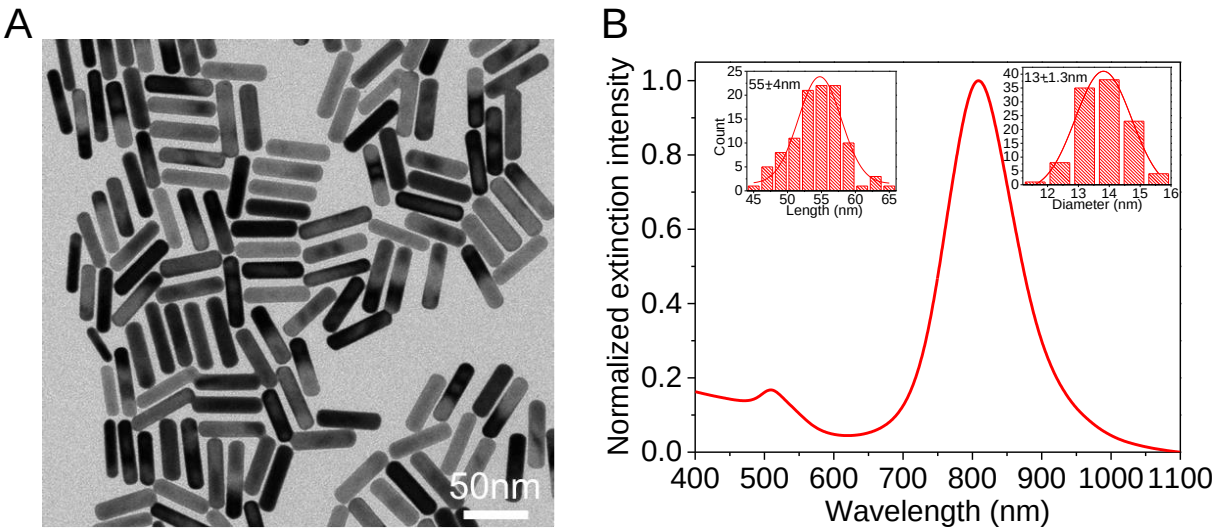

Figure S1. 2 (A) TEM image of Au nanorods. (B) Vis-NIR extinction spectrum of the aqueous suspensions of Au nanorods (inset shows the histogram of the size distribution as measured from TEM images).

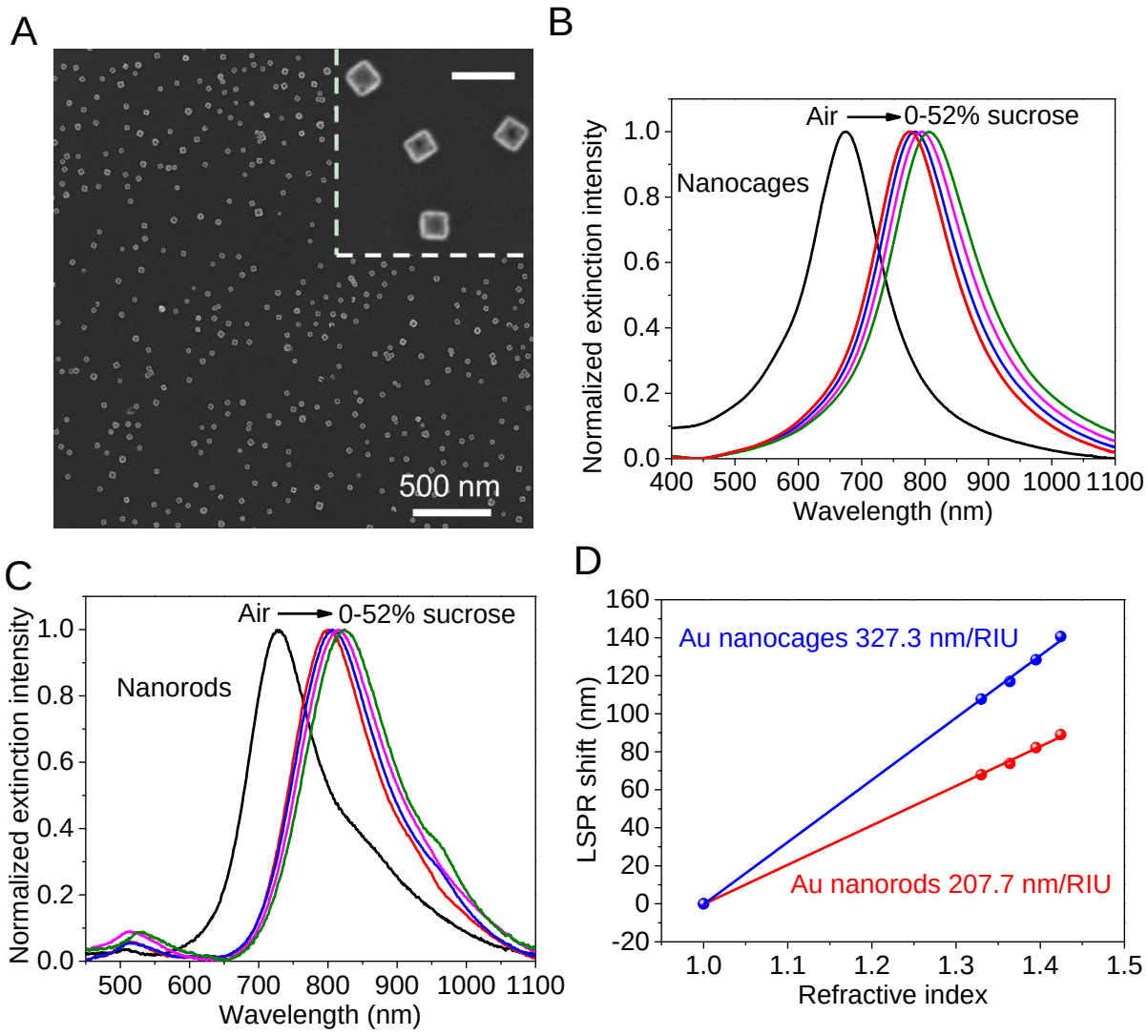

Figure S1. 3 (A) SEM of Au nanocages adsorbed on a glass substrate. Vis-NIR extinction spectra of (B) Au nanocages and (C) Au nanorods in air and different concentrations of sucrose aqueous solution. (D) Comparison of bulk refractive index sensitivity of Au nanocages and nanorods.

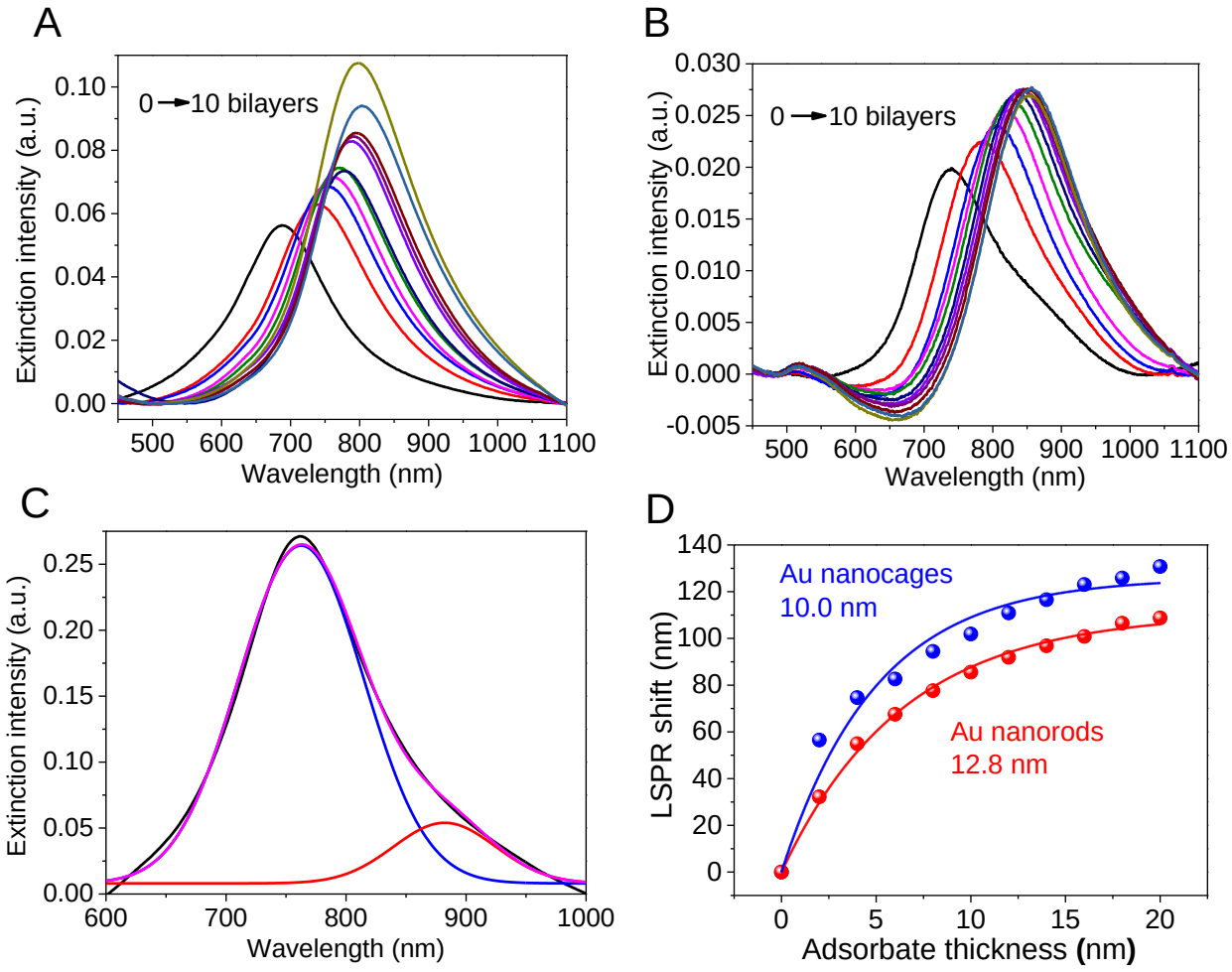

Figure S1. 4 Vis-NIR extinction spectra of (A) AuNCs and (B) AuNRs following the deposition each polyelectrolyte bilayer showing a progressive red-shift and increase in the intensity of the longitudinal plasmon band. (C) Representative LSPR spectrum of AuNCs deconvoluted using two Gaussian peaks. (D) Comparision of distance depndenct refractive index sensitivity of Au nanocages and nanorods.

Appendix 2

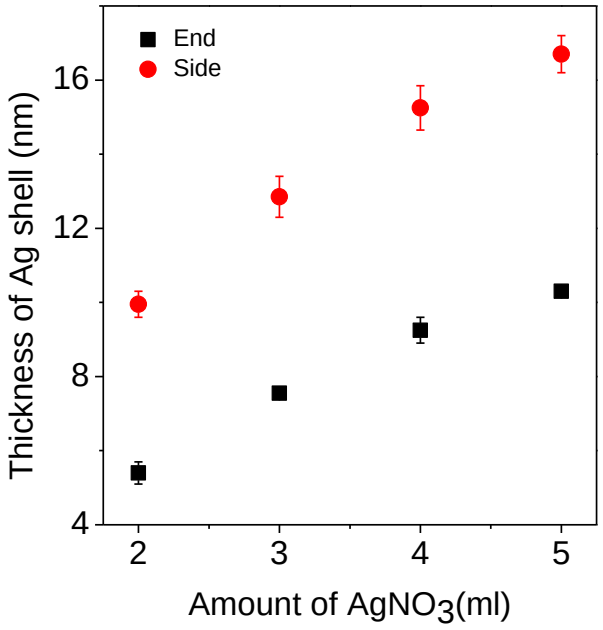

Figure S2. 1 Plot showing the linear increase in the Ag shell thickness at the ends and on the sides of AuNR with increasing amount of $AgNO_3$ in the shell growth solution.

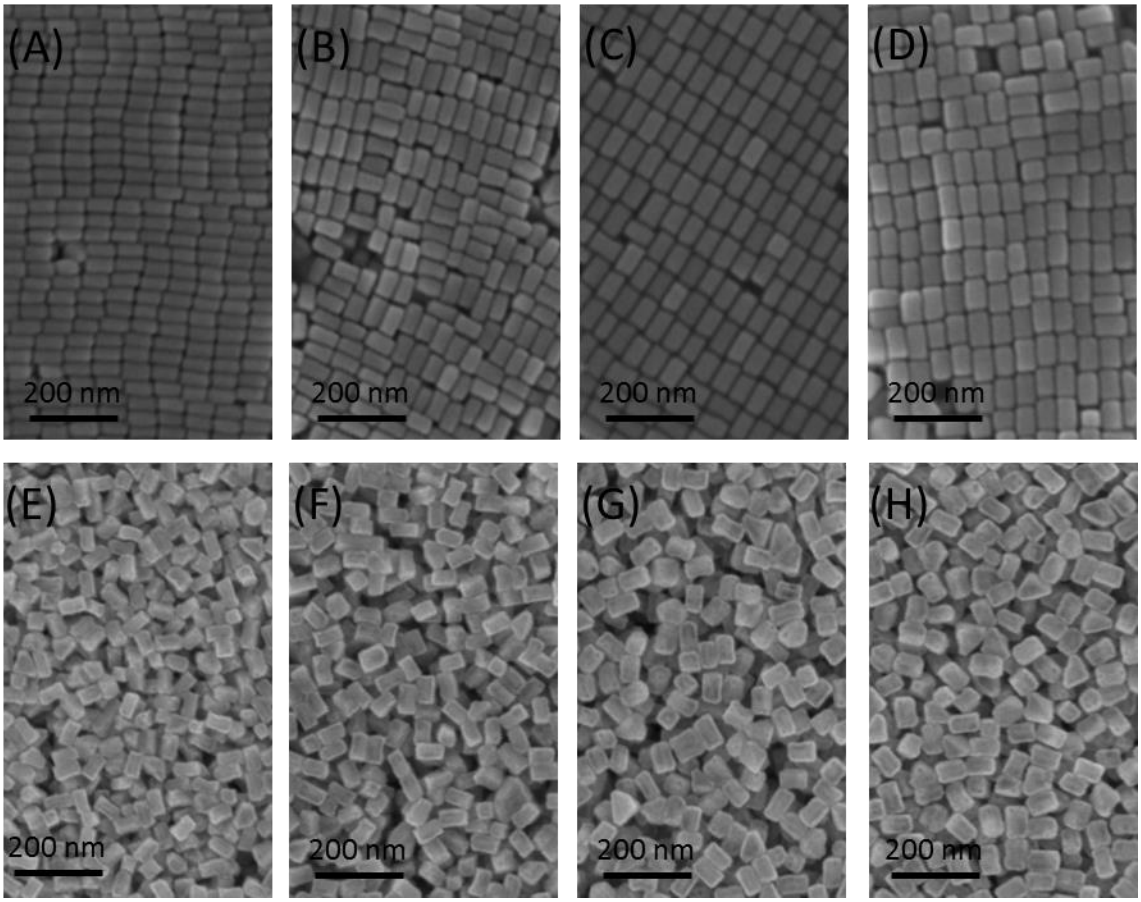

Figure S2. 2 (A)-(D) SEM images of AuNR@Ag nanocuboids with dimensions of (A) 62.7×31.2 nm, (B) 67.0×37.0 nm, (C) 70.4×41.8 nm and (D) 72.5×44.7 nm. (E)-(H) SEM images of Au cuboidal nanorattles with dimensions of (E) 69.5×37.9 nm, (F) 74.1×44.6 nm, (G)78.9×50.0 nm and (H) 83.1×55.2 nm.

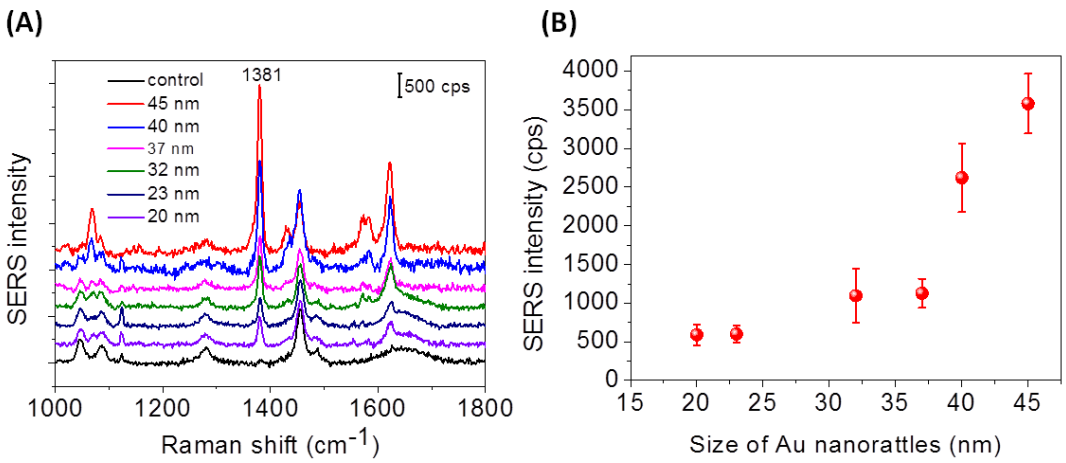

Figure S2. 3 (A) SERS spectra from Au nanorattles with AuNS cores obtained using 514 nm laser. (B) Plot showing the SERS intensity of the 1381 cm^{-1} Raman band of 2-NT vs. size of Au nanorattles.

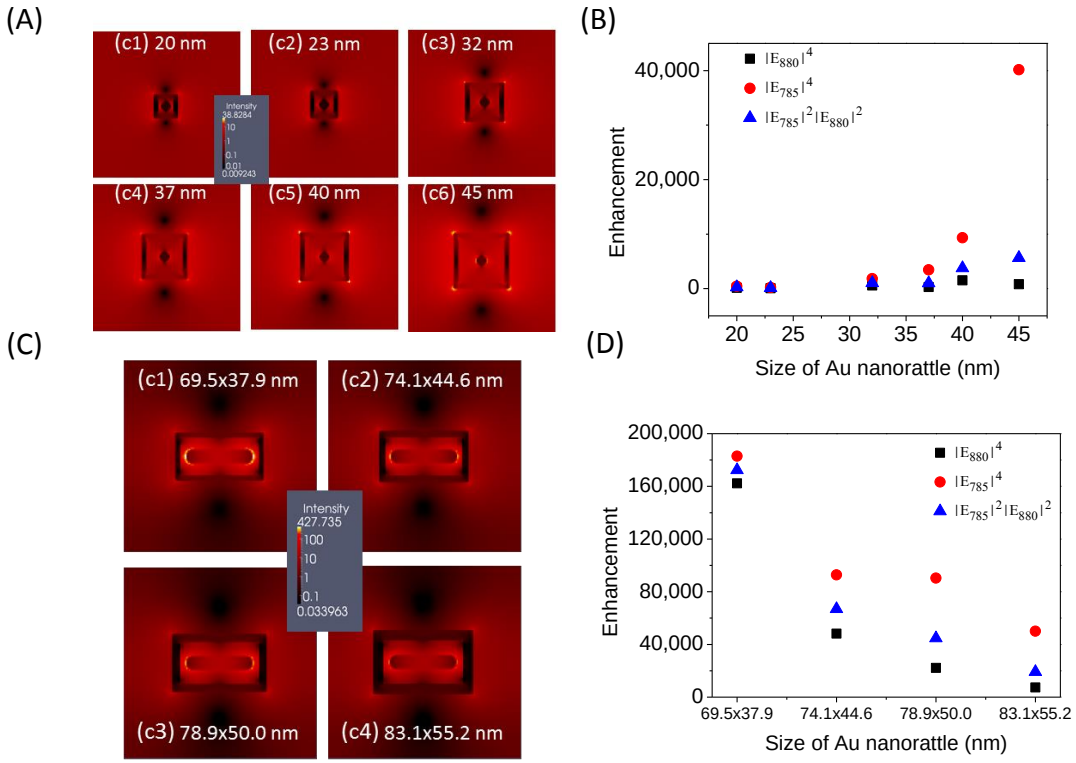

Figure S2. 4 (A) FDTD simulations showing the electric field distribution of Au cubic nanorattles of different sizes using 880 nm excitation wavelength (c1-c6 correspond to electric field distribution of Au nanorattles with edge length of 20, 23, 32, 37, 40 and 45nm, respectively). (B) Plot showing the enhancement with increase in the edge length of Au nanorattles with AuNS cores. (C) FDTD simulations showing the electric field distribution of Au cuboid nanorattles of different sizes using 880 nm excitation wavelength (c1-c4 correspond to electric field distribution of Au nanorattles with dimensions 69.5×37.9 nm, 74.1×44.6 nm, 78.9×50.0 nm and 83.1×55.2 nm, respectively (D) Plot showing the enhancement with increase in the edge length of Au nanorattles with AuNR cores.

Enhancement factor (EF):

The enhancement factor (EF) of each Au nanorattle was calculated by using the following equation[55, 148, 149, 257].

$$\mathrm{EF} = \frac{I_{SERS}/N_{SERS}}{I_{bulk}/N_{bulk}}$$

Where I_{SERS} and I_{bulk} are intensities of the same band for the SERS and bulk spectra, N_{SERS} is the number of the 2-napthalnethiol (2-NT) bound to the surface of Au nanorattles and N_{bulk} is the number of the 2-NT in the excitation volume.

For Au nanorattle with size of 45 nm, I_{SERS} =~3000 counts and I_{bulk}=~125 counts.

Raman spectrum of 2-NT in bulk was collected using 20x microscopy objective (with a numerical aperture (NA) =0.4). The approximate laser spot size of 20X objective can be obtained using the following expression:

$$\omega_0 = 4\lambda/\pi\mathrm{NA}$$

Where ω_0 is the minimum waist diameter for a laser beam of a wavelength λ focused by an objective with a numerical aperture NA. So for 20x objective,

$$\omega_0 = \frac{(4)(0.785)}{\pi(0.4)} = 2.5\ \mu m.$$

$$z_0 = \frac{2\pi{\omega_0}^2}{\lambda} = \frac{2\pi(2.5)^2}{0.785} = 50\ \mu m$$

So, the focal volume $(\tau) = (\frac{\pi}{2})^{1.5}{\omega_0}^2 z_0 = (\frac{\pi}{2})^{1.5}\times 2.5^2\times 50 = 614.75\ \mu m^2$

Density of the 2-NT is 1.55 g/cm^3 , molecular mass of 2-NT is 160.24 (g/mol)

$$N_{bulk} = \frac{(1.55 g/cm^3)(614.75 \mu m^3)}{160.24} = 5.95\times 10^{-12}\ \mathrm{mol}$$

The volume of individual Au nanorattle with AuNS core with edge length of 45 nm is estimated to be $(45-8)^3\ nm^3$

$$N_{SERS} = \frac{(1.55 g/cm^3)(45-8)^3 nm^3}{160.24} = 4.90\times10^{-19}\ \text{mol}$$

$$\text{EF} = \frac{I_{SERS}/N_{SERS}}{I_{bulk}/N_{bulk}} = \frac{3000/4.9\times10^{-19}}{125/5.95\times10^{-12}} = 2.91\times10^{8}$$

The volume ratio of AuNS for the synthesis of Au nanorattle with size of 45:40:37:32:23:20 nm is 0.15:0.2:0.5:1.0:2.0:3.0, so the ratio of N_{SERS} is $\frac{20}{20}:\frac{15}{20}:\frac{6}{20}:\frac{3}{20}:\frac{1.5}{20}:\frac{1}{20}$.

I_{SERS} of Au nanorattle with size of 40, 37, 32, 23 and 20 nm is around 1700, 440, 420, 210 and 150 counts. The SERS enhancement factors of Au nanorattles with size of 40, 37, 32, 23 and 20 nm is $1.91\times10^8, 2.66\times10^7, 2.24\times10^7, 2.30\times10^7, 2.13\times10^7$, respectively. The SERS enhancement factor vs. size of Au nanorattles is shown as below.

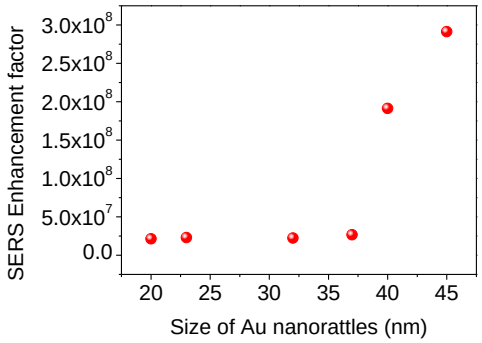

Figure S2. 5 SERS enhancement factor vs. size of Au nanorattles with AuNS core.

The volume of individual Au nanorattle with AuNR core with dimension of 69.5x37.9x37.9 nm is estimated to be $(69.5-10)\times(37.9-10)\times(37.9-10)\ nm^3$

$$N_{SERS} = \frac{(1.55 g/cm^3)(69.5-10)(37.9-10)(37.9-10) nm^3}{160.24} = 4.48\times10^{-19}\ \text{mol}$$

$$\text{EF} = \frac{I_{SERS}/N_{SERS}}{I_{bulk}/N_{bulk}} = \frac{11000/4.48\times10^{-19}}{125/5.95\times10^{-12}} = 1.17\times10^{9}$$

SERS enhancement factors for cuboidal Au nanorattles with dimensions of 74.1x44.6 nm, 78.9x50.0 nm, 83.1x55.2 nm is $3.21\times10^{8}, 1.47\times10^{8}, 6.59\times10^{7}$, respectively. The SERS enhancement factor vs. size of Au nanorattles is shown as below:

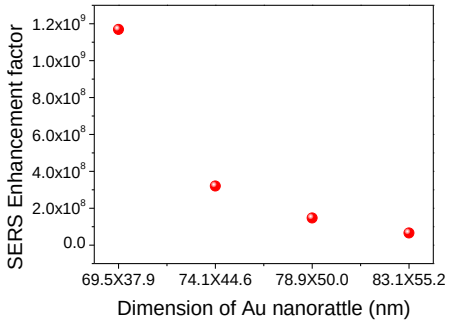

Figure S2. 6 SERS enhancement factor vs. size of Au nanorattles with AuNR core.

Estimation of the concentration of Au nanorattles:

The concentration of Au nanoparticles was calculated using the following expression:

A=εbC where A is absorption, ε is extinction coefficient, for Au nanoparticle with diameter of 8.55 nm ε = $5.14\text{x}10^{7}$ ($M^{-1}cm^{-1}$).[258] Light path in the UV-cuvette (b) is 1 cm. C is molar concentration of nanoparticle solution. Our experimental result shows that extinction of Au nanoparticles is 1.2, so molar concentration of nanoparticle solution is $23.35\text{x}10^{-9}$ M. For 1 ml solution of Au nanoparticles, the concentration is $23.35\times10^{-12}\times6.023\text{x}10^{23}=1.41\times10^{13}$ nanoparticles/ml. The approximate concentration of Au nanorattles with spherical cores is about 1.41×10^{13} nanoparticles/ml.

The ε of AuNR with aspect ratio of 4.6 (length 51.9 nm and diameter 11.3 nm) is about 35×10^{8} $M^{-1}cm^{-1}$.[259] The extinction of AuNR solution in our study is 2.0, so the molar concentration of AuNR solution is 5.71×10^{-9} M. So for 1 ml solution of Au nanorods, the concentration is

$5.71.x10^{-12} \times 6.023 \times 10^{23} = 3.44 \times 10^{12}$ nanorods/ml solution. The approximate concentration of Au nanorattles with nanorod cores is about 3.44×10^{12} nanoparticles/ml.

Appendix 3

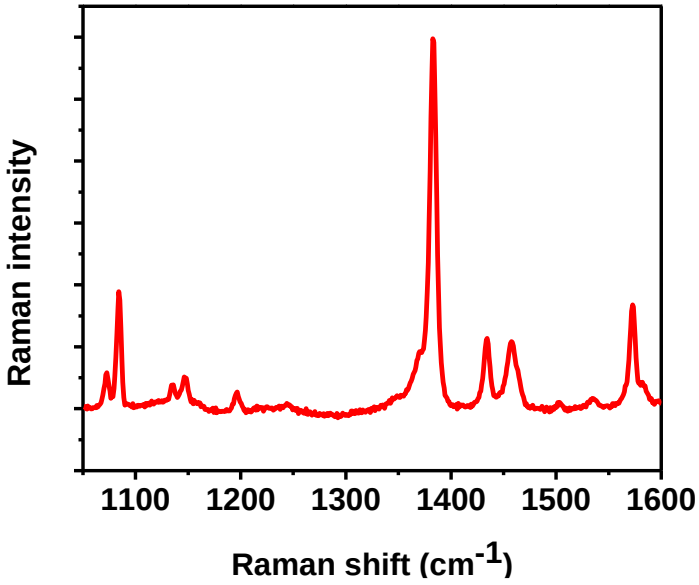

Figure S3. 1 Raman spectrum of bulk 2-NT.

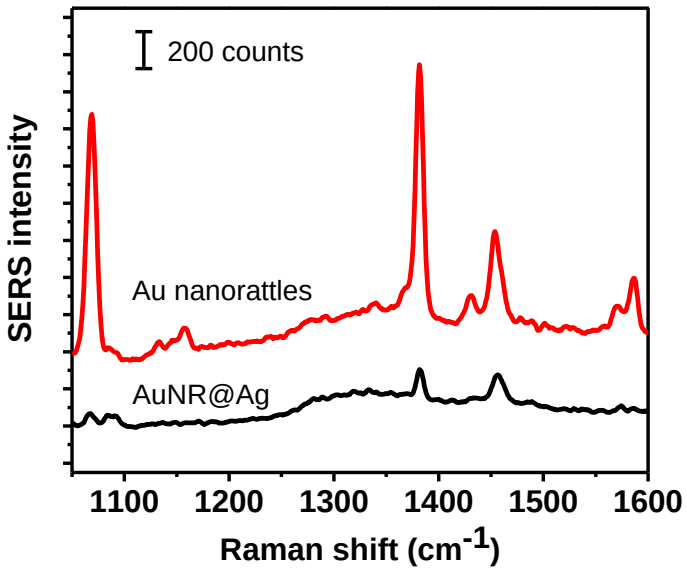

Figure S3. 2 Surface enhanced Raman scattering (SERS) spectra collected from 2-NT adsorbed on Au nanorattles and AuNR@Ag nanocuboids in aqueous media using 785 nm laser excitation.

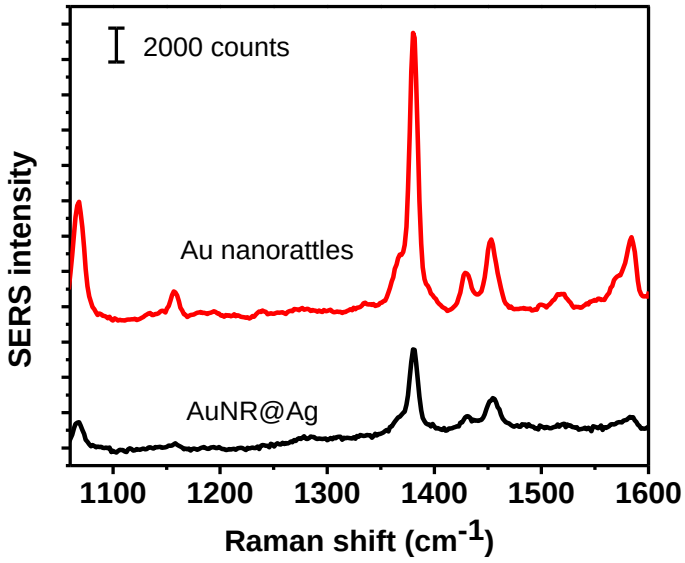

Figure S3. 3 SERS spectra collected from 2-NT adsorbed on Au nanorattles and AuNR@Ag nanocuboids in aqueous media using 514.5 nm laser excitation.

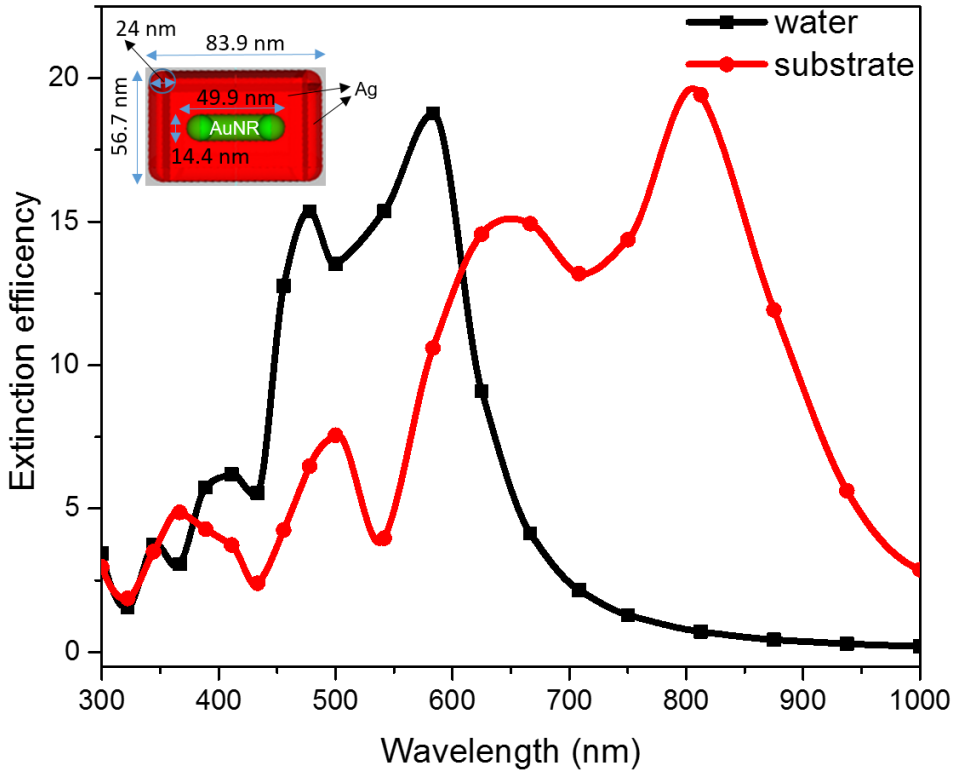

Figure S3. 4 DDA simulated extinction spectra of AuNR@Ag nanocuboids in water (black) and on a Si substrate in air (red). Inset shows schematic of the nanostructure with dimensions. Data points obtained from calculation are connected by a spline curve.

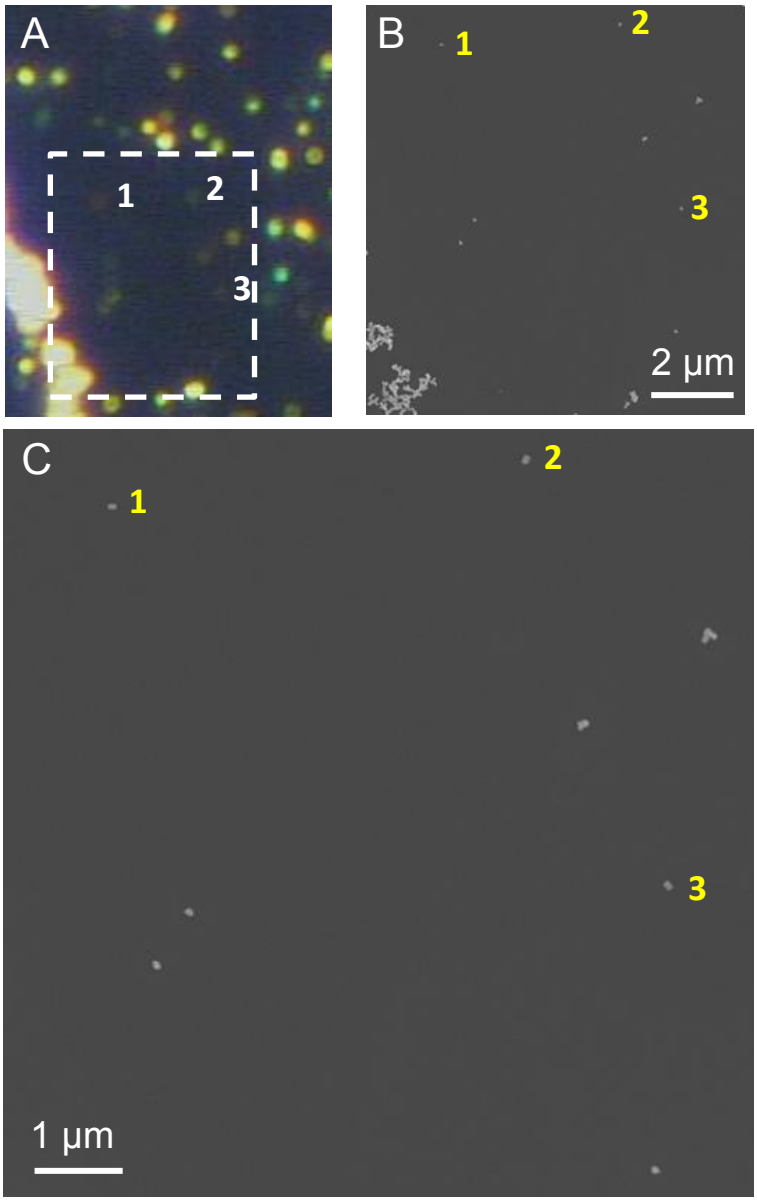

Figure S3. 5 (A) Dark-field optical image of Au nanorattles adsorbed on a silicon substrate. Labels 1, 2 and 3 each identify a representative Au nanorattle for polarization-dependent SERS measurement. (B) SEM image of Au nanorattles adsorbed on a silicon substrate from the region

marked by the white dashed box in (A). (C) Enlarged SEM image clearly identifying the three representative Au nanorattles from (B).

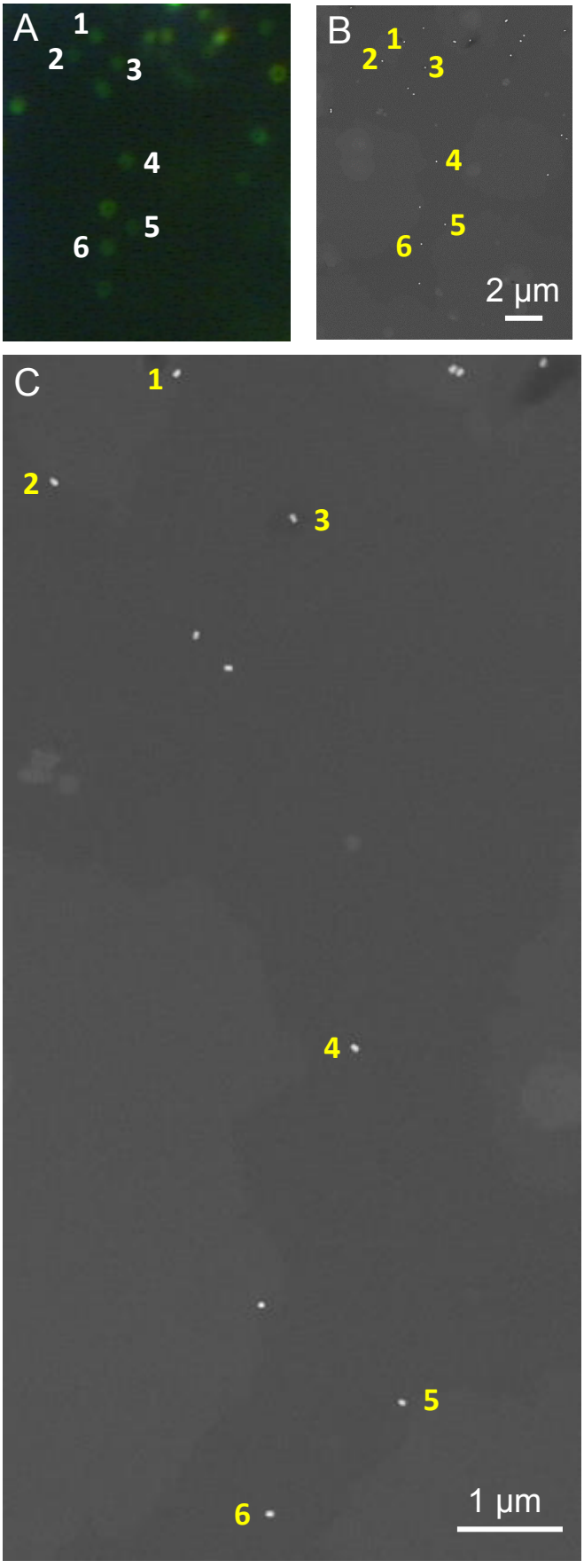
A
1
2
3
4
5
6
B
1
2
3
4
5
6
2 µm
C
1
2
3
4
5
6
1 µm

Figure S3. 6 (A) Dark-field optical image of AuNR@Ag nanocuboids adsorbed on a silicon substrate. Labels 1-6 each identify a representative AuNR@Ag nanocuboid for polarization-dependent SERS measurement. (B) SEM image of AuNR@Ag nanocuboids adsorbed on a silicon substrate from the entire region shown in (A). (C) Enlarged SEM image clearly identifying the six representative AuNR@Ag nanocuboids from (B).

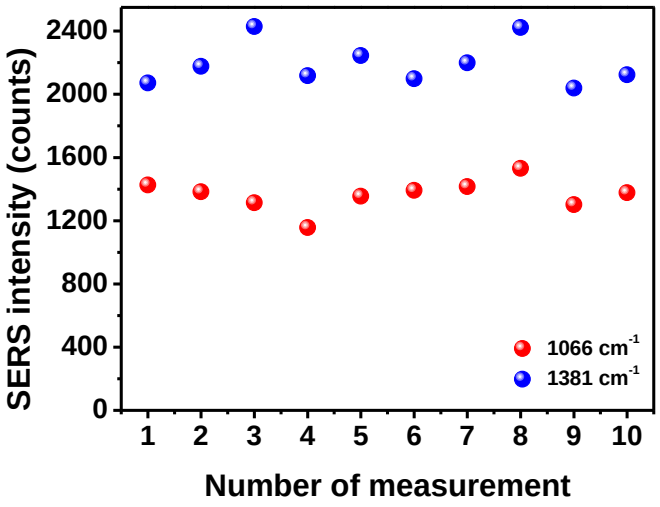

Figure S3. 7 Stability of SERS signal at 1066 cm^{-1} and 1381 cm^{-1} peaks obtained from an individual Au nanorattle at a polarization angle of 0°.

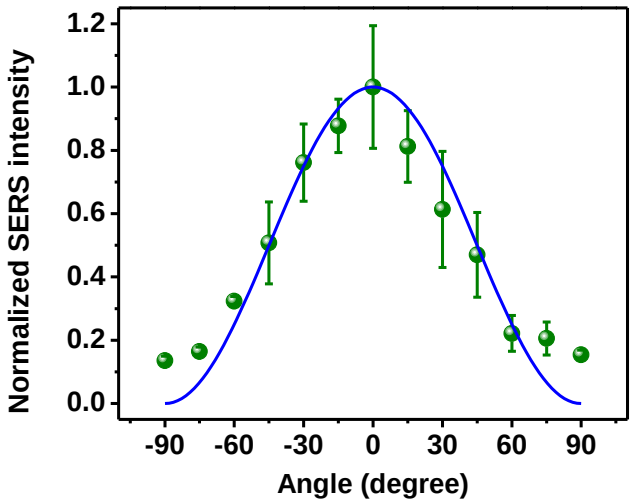

Figure S3. 8 Normalized SERS intensity (at the 1381 cm^{-1} peak) of an individual Au nanorattle as a function of polarization angle. The blue line is a fit to the $\cos^2$ function. The error bars represent the standard deviation of five identical measurements performed at each polarization angle.

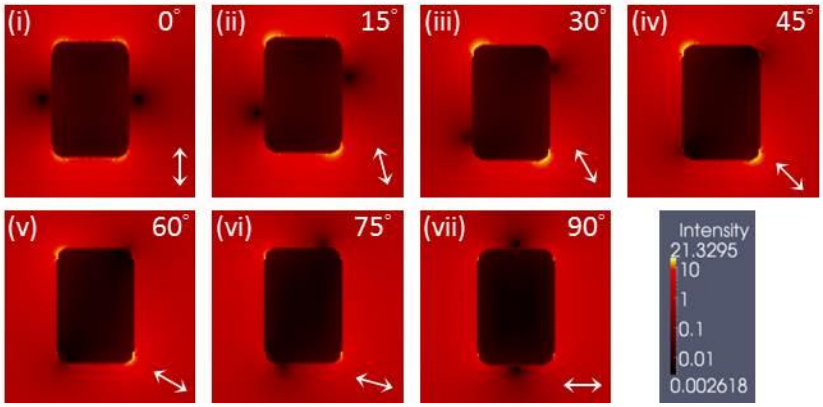

Figure S3. 9 Finite-difference time-domain (FDTD) simulations showing the electric field distribution around a AuNR@Ag nanocuboid under various incident polarization angles using 880 nm excitation wavelength. The incident polarization angle is 0°, 15°, 30°, 45°, 60°, 75° and 90° in (i)-(vii) respectively.

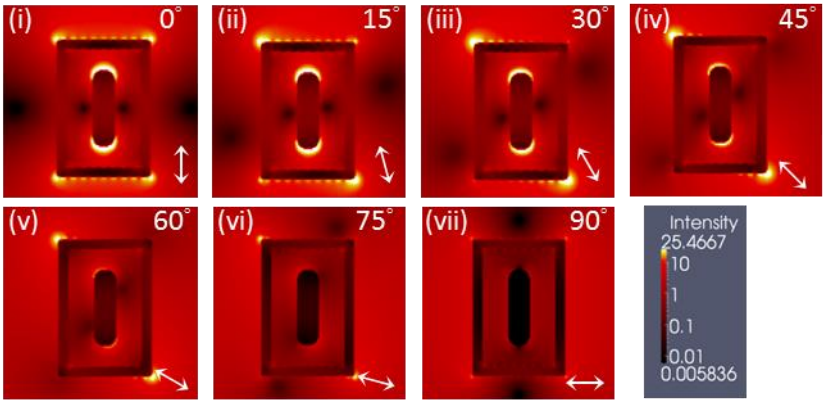

Figure S3. 10 FDTD simulations showing the electric field distribution around an Au nanorattle under various incident polarization angles using 880 nm excitation wavelength. The incident polarization angle is 0°, 15°, 30°, 45°, 60°,75° and 90° in (i)-(vii) respectively.

The SERS enhancement factor (EF) for each Au nanostructure was calculated by using the equation[149,55]:

$$\mathrm{EF} = \frac{I_{SERS}/N_{SERS}}{I_{bulk}/N_{bulk}} \quad (1)$$

where I_{SERS} and I_{bulk} are intensities of the same Raman band in the SERS and bulk spectra, N_{SERS} is the number of the 2-napthalnethiol molecules bound to the surface of the Au nanostructure and N_{bulk} is the number of the 2-napthalnethiol molecules in the excitation volume. For the Au nanorattle, I_{SERS} is ~1545 counts and $I_{bulk}$is ~125 counts. A Raman spectrum of 2-napthalnethiol in the bulk was collected using a 20x microscopy objective with a numerical aperture (NA) of 0.4. The approximate laser spot size with the 20x objective was obtained using the following expression:

$$\omega_0 = 4\lambda/\pi\mathrm{NA} \quad (2)$$

where ω_0 is the minimum waist diameter for a laser beam of a wavelength λ focused by an objective with a numerical aperture NA. So for the 20x objective,

$$\omega_0 = \frac{(4)(0.785)}{\pi(0.4)} = 2.5\ \mu m.$$
$$z_0 = \frac{2\pi{\omega_0}^2}{\lambda} = \frac{2\pi(2.5)^2}{0.785} = 50\ \mu m$$

So, the focal volume $(\tau) = (\frac{\pi}{2})^{1.5}{\omega_0}^2 z_0 = (\frac{\pi}{2})^{1.5}\times 2.5^2\times 50 = 614.75\ \mu m^2$. Density of the 2-napthalnethiol is 1.55 g/cm^3 and the molecular mass of 2-napthalnethiol is 160.24 (g/mol). Therefore,

$$N_{bulk} = \frac{(1.55 g/cm^3)(614.75 \mu m^3)}{160.24\ (g/mol)} = 5.95\times 10^{-12}\ \mathrm{mol}$$

The volume of an individual Au nanorattle with edge dimension of 89.3 x 60.6 x 60.6 nm and a AuNR core with length of 49.9 nm and width of 14.4 nm is estimated to be $(89.3 - 13)(60.6 - 13)^2 - \left[\pi(7.2)^2\times 35.5 + \frac{4}{3}\times\pi\times(7.2)^3\right] = 165533.3\ nm^3$

$$N_{SERS} = \frac{(1.55 g/cm^3)\times 165533.3 nm^3}{160.24} = 1.60\times 10^{-18}\ \mathrm{mol}$$
$$\mathrm{EF} = \frac{I_{SERS}/N_{SERS}}{I_{bulk}/N_{bulk}} = \frac{1545/1.60\times 10^{-18}}{125/5.95\times 10^{-12}} = 4.60\times 10^7$$

Appendix 4

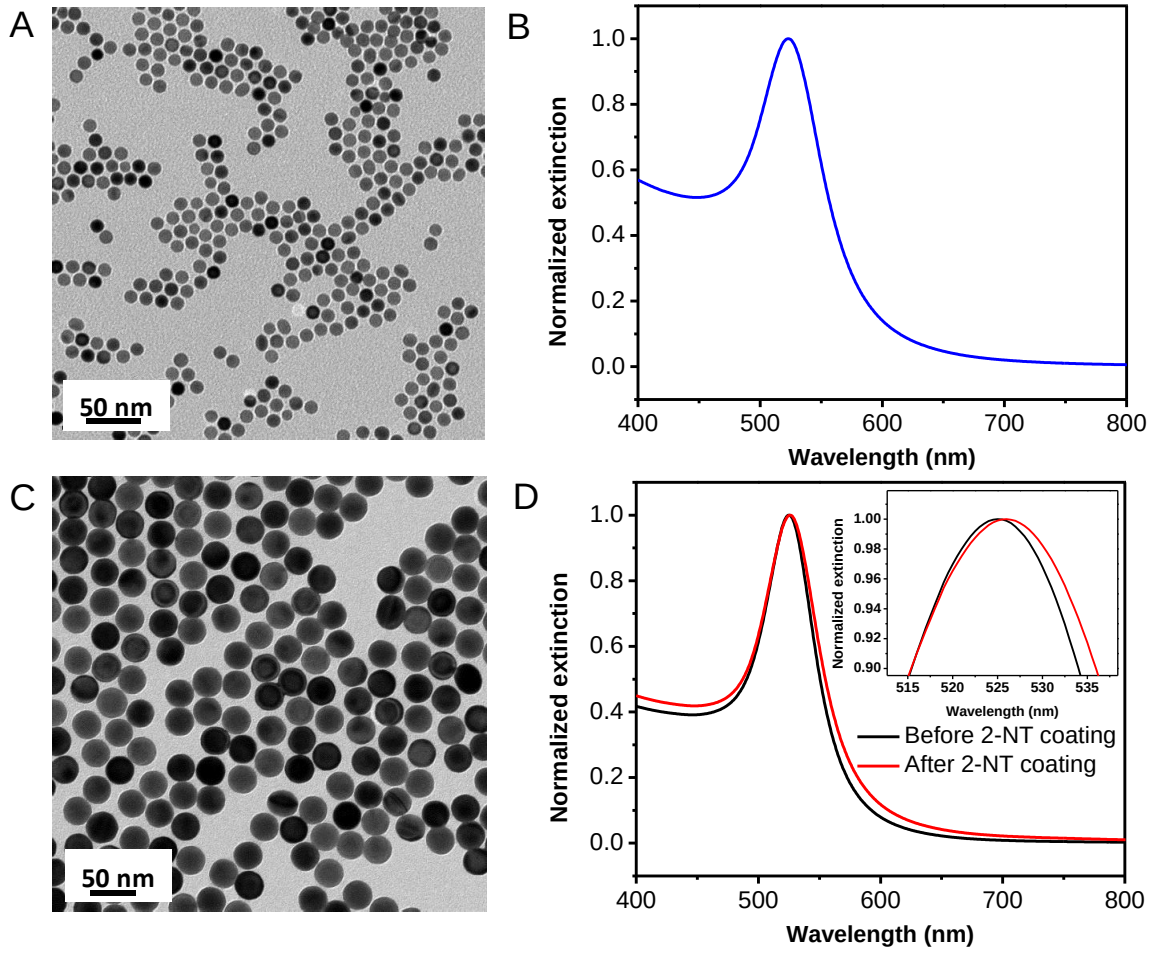

Figure S4. 1 (A) TEM image of 10 nm Au nanospheres. (B) Vis-NIR extinction spectrum of 10 nm Au nanospheres. (C) TEM image of 30 nm Au nanospheres employed as cores for the synthesis of Au@Ag nanocubes. (D) Vis-NIR extinction spectrum of 30 nm Au nanospheres before (black) and after (red) 2-NT coating.

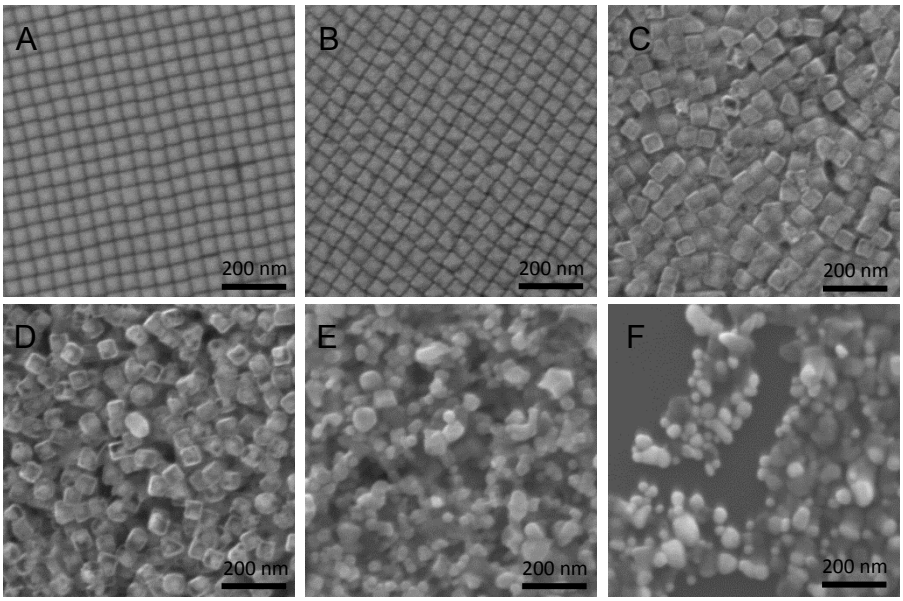

Figure S4. 2 (A)-(F) SEM images of Au@Ag nanocubes and Au nanorattles obtained by adding 0, 20, 40, 60, 80 and 100 µl of 0.5 mM $HAuCl_4$ into 100 µl of 2-NT-Au@Ag nanocubes, respectively.

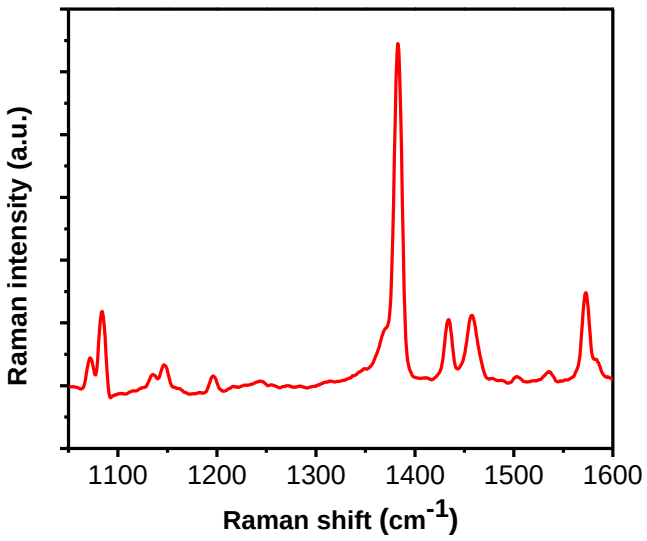

Figure S4. 3 Raman spectrum collected from bulk 2-NT.

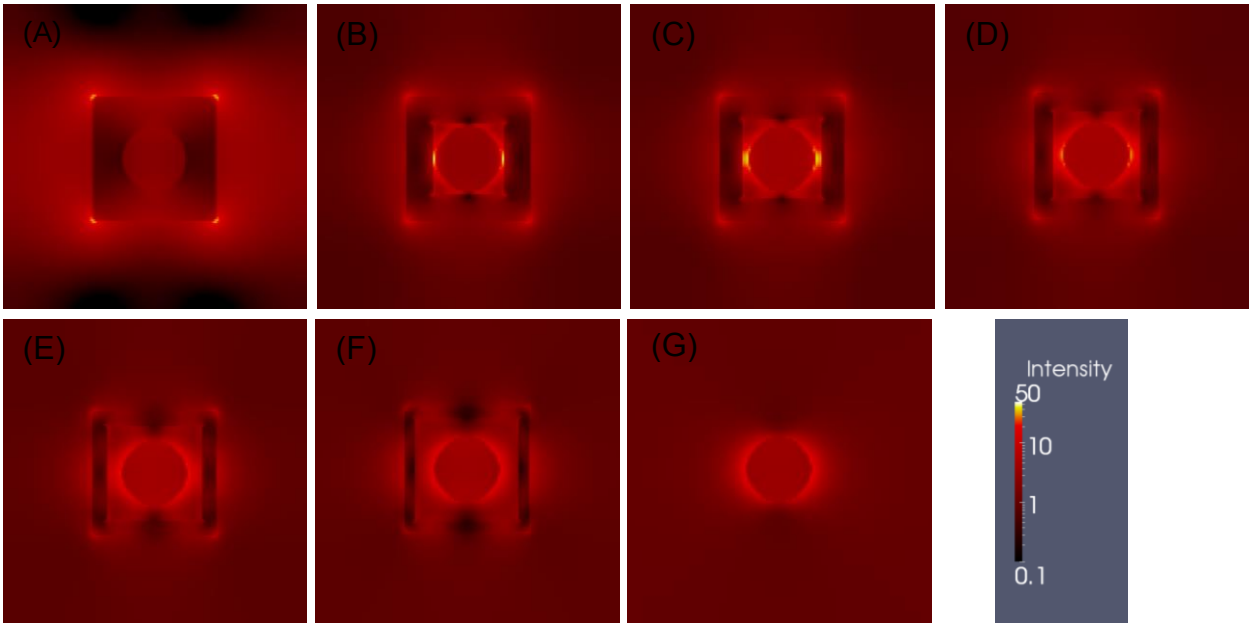

Figure S4. 4 FDTD simulations showing the electric field distribution of Au@Ag nanocube and Au nanorattles of different gaps for electric field polarized along [100] using 514 nm excitation wavelength. (A-G) correspond to electric field distribution of Au@Ag nanocubes and Au nanorattles with a gap of 2, 4, 6, 8, 10 nm and Au core only, respectively.

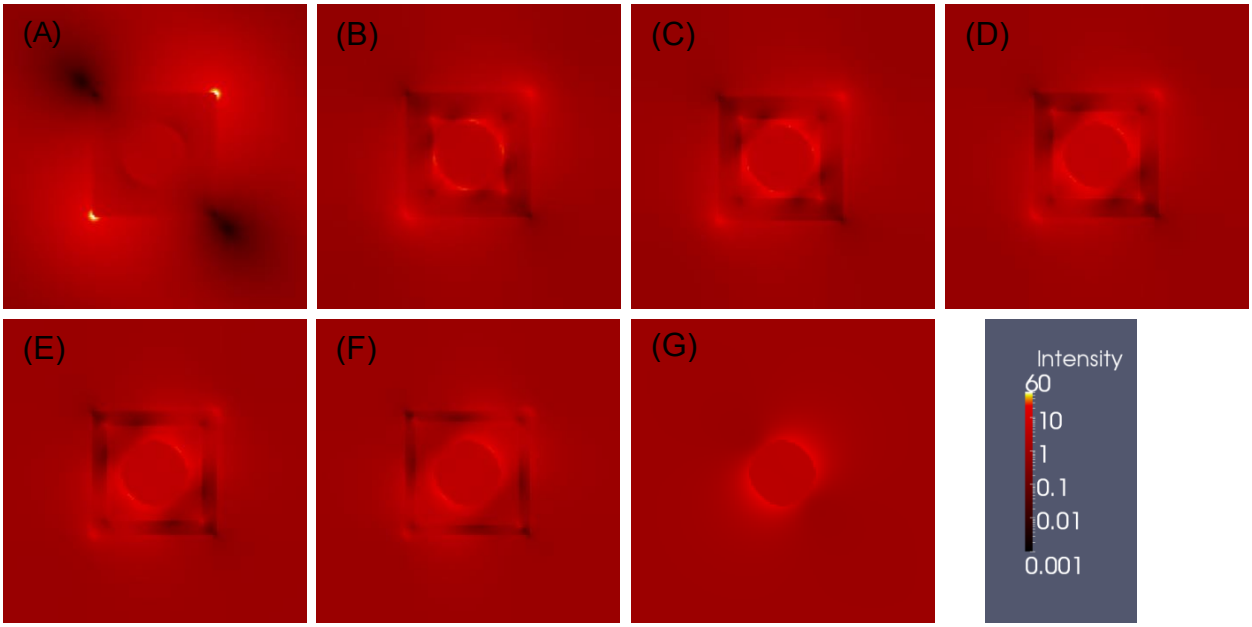

Figure S4. 5 FDTD simulations showing the electric field distribution of Au@Ag nanocube and Au nanorattles of different gaps for electric field polarized along [110] using 514 nm excitation wavelength. (A-G) correspond to electric field distribution of Au@Ag nanocubes and Au nanorattles with a gap of 2, 4, 6, 8, 10 nm and Au core only, respectively.

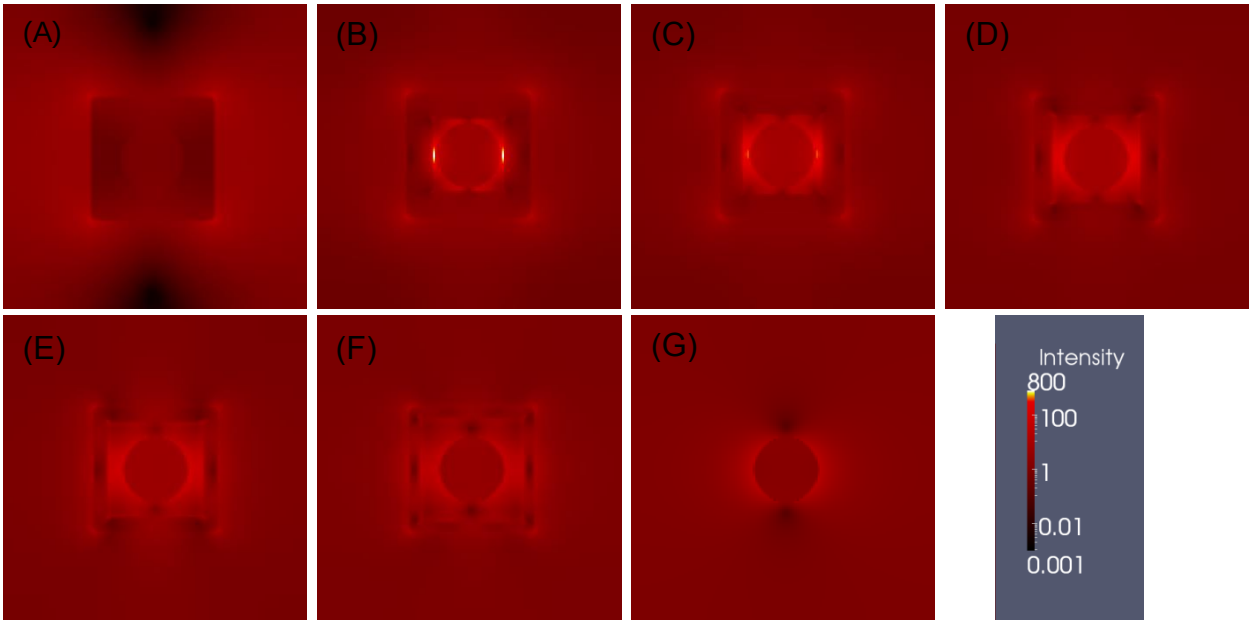

Figure S4. 6 FDTD simulations showing the electric field distribution of Au@Ag nanocube and Au nanorattles of different gaps for electric field polarized along [100] using 553 nm excitation wavelength. (A-G) correspond to electric field distribution of Au@Ag nanocubes and Au nanorattles with a gap of 2, 4, 6, 8, 10 nm and Au core only, respectively.

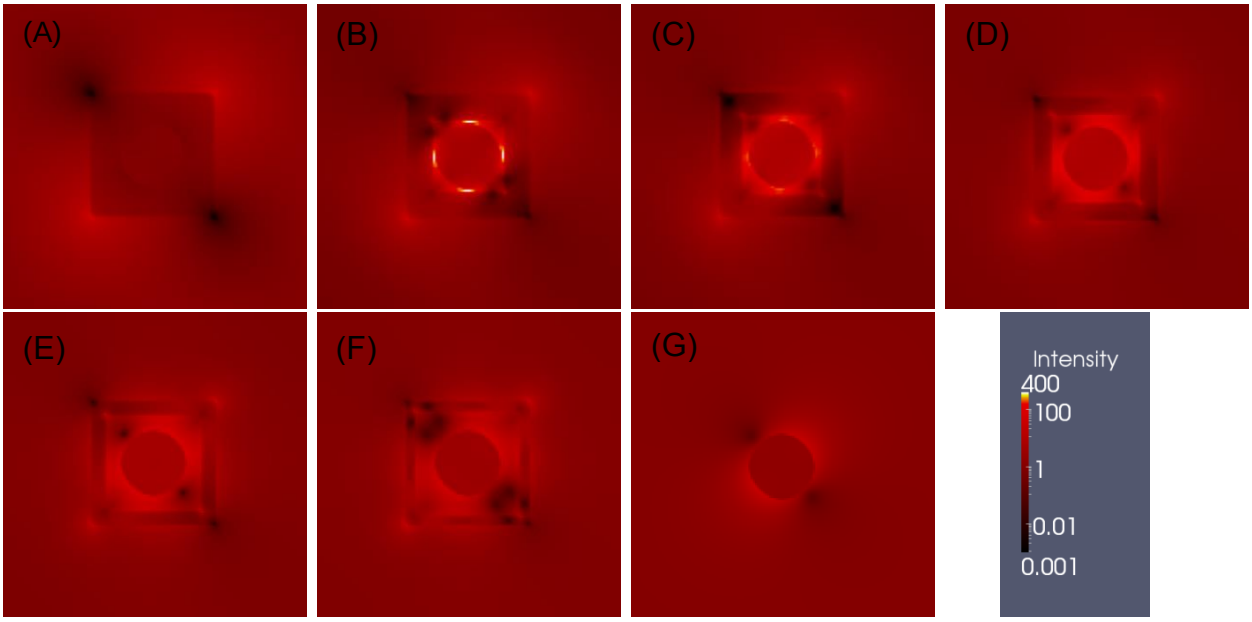

Figure S4. 7 FDTD simulations showing the electric field distribution of Au@Ag nanocube and Au nanorattles of different gaps for electric field polarized along [110] using 553 nm excitation wavelength. (A-G) correspond to electric field distribution of Au@Ag nanocubes and Au nanorattles with a gap of 2, 4, 6, 8, 10 nm and Au core only, respectively.

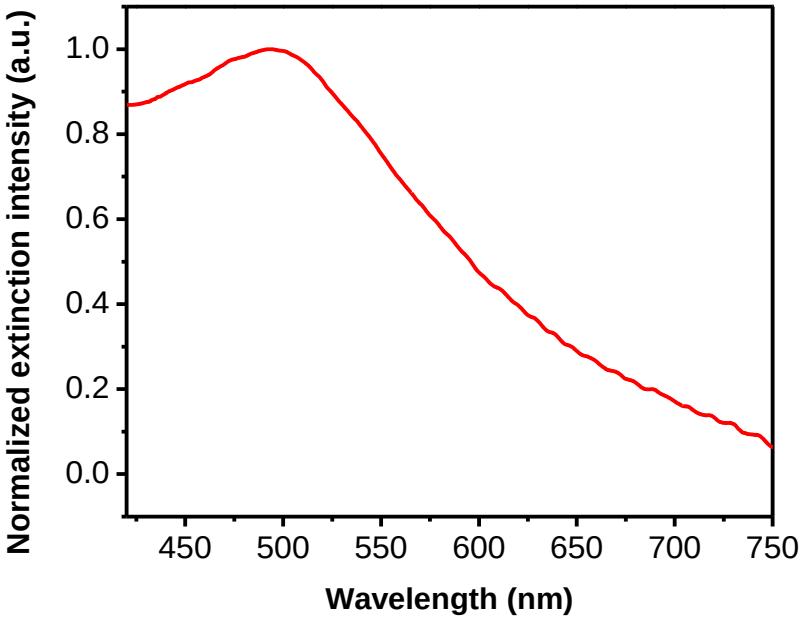

Figure S4. 8 (A) Normalized vis-NIR extinction spectrum obtained from filter paper substrate adsorbed with 20-AuNRT.

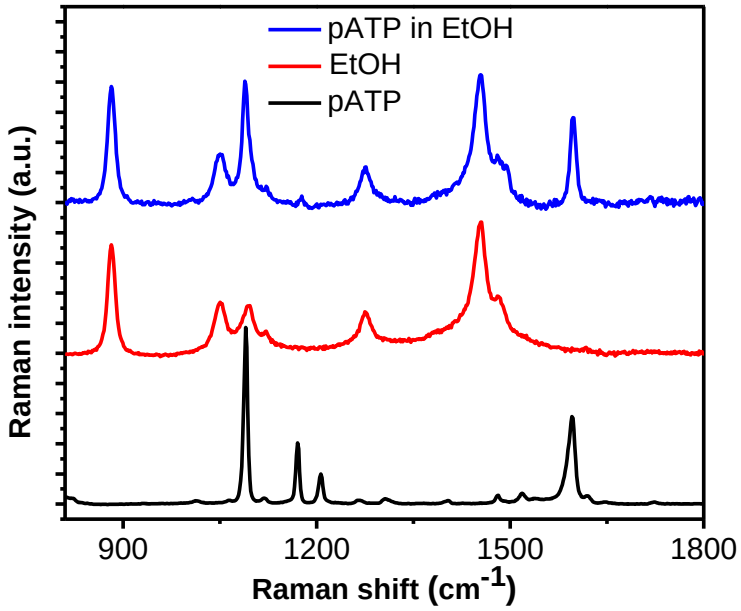

Figure S4. 9 Raman spectra collected from bulk-pATP, ethanol and pATP in ethanol.

Appendix 5

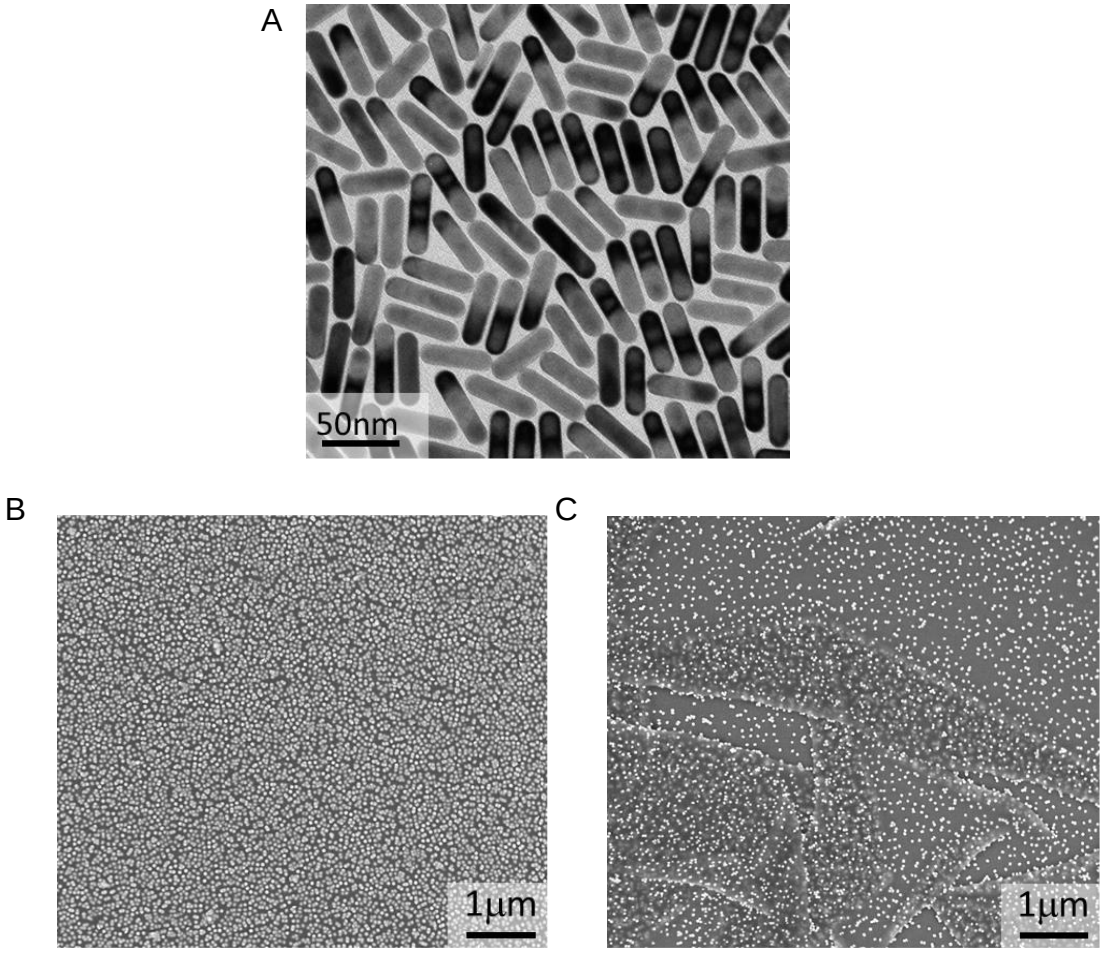

Figure S5. 1 (A) Representative TEM image of AuNRs. SEM images of (B) the pristine film and (C) folded film showing dramatic change in the distribution of nanostructures.

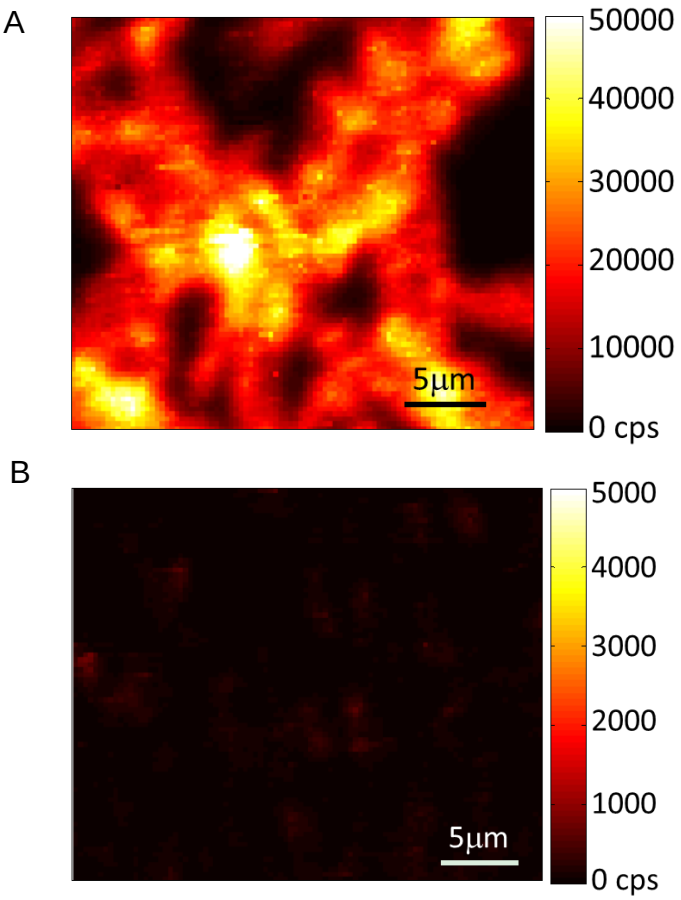

Figure S5. 2 (A) SERS intensity map from folded film showing lenticular pattern. (B) SERS intensity map from pristine film showing significantly lower intensity compared to that from folded film.

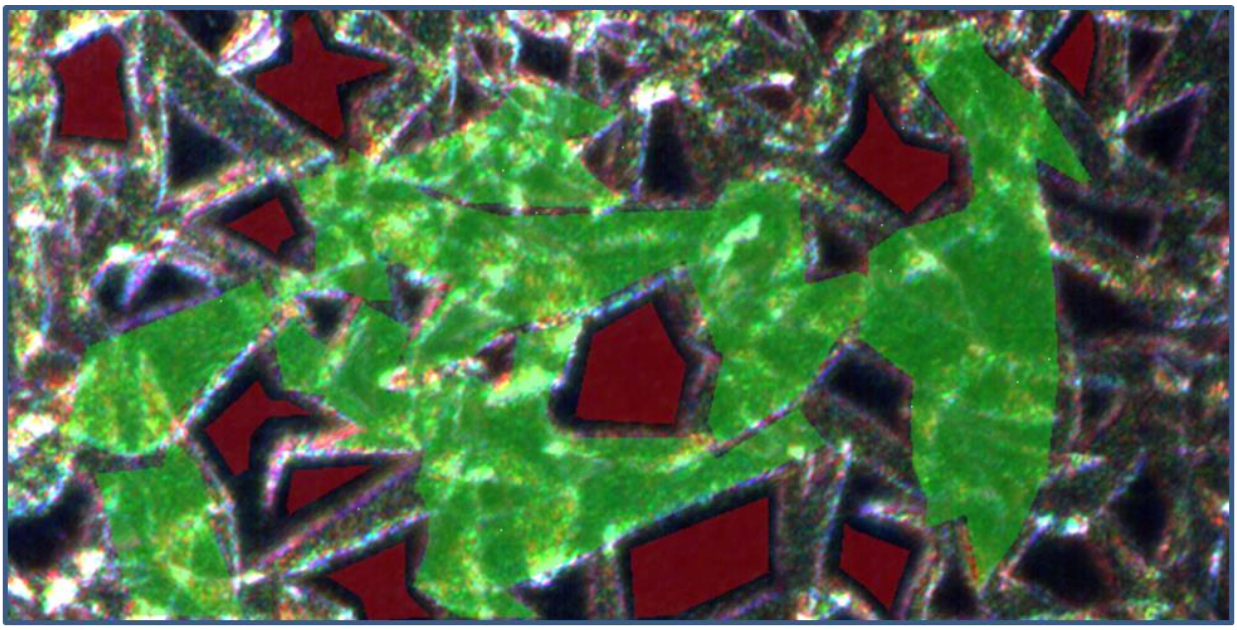

Figure S5. 3 Scattering spectra selection for the stretched (red) and folded (green) regions of the polymer film. Approximately 17,000 and 80,000 point spectra were averaged to obtain the final composite spectra for the stretched and folded regions respectively.

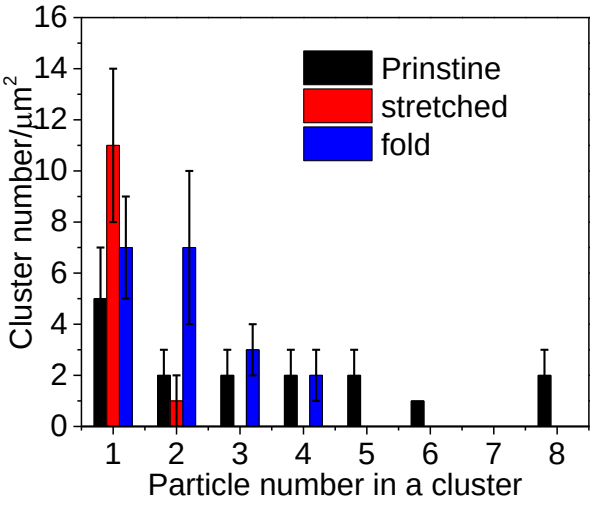

Figure S5. 4 Statistical analysis on the nanoparticle distribution on pristine film and folded film including both stretched and folded regions.

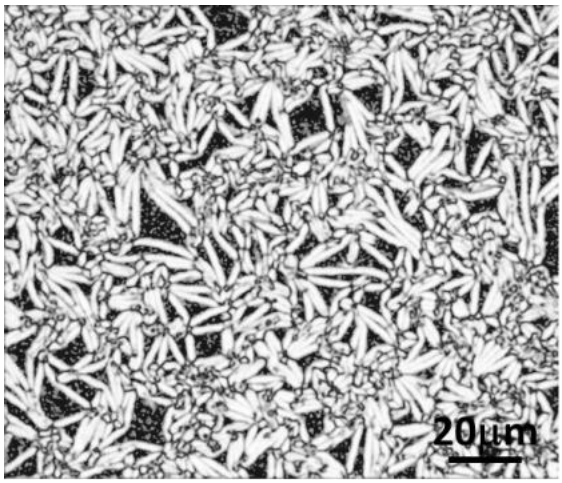

Figure S5. 5 Vector distribution reliability map, in which white color represents higher reliability.

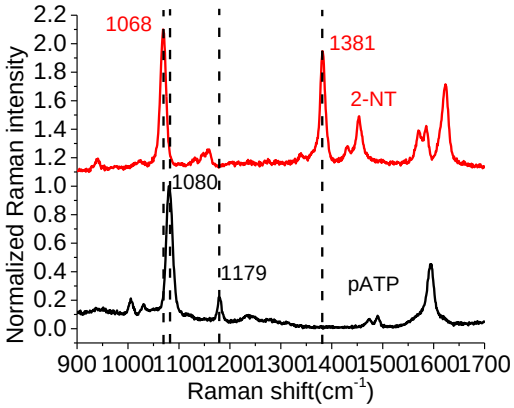

Figure S5. 6 SERS spectra collected from two Raman reporters, pATP and 2-NT, adsorbed on gold nanostructures respectively.

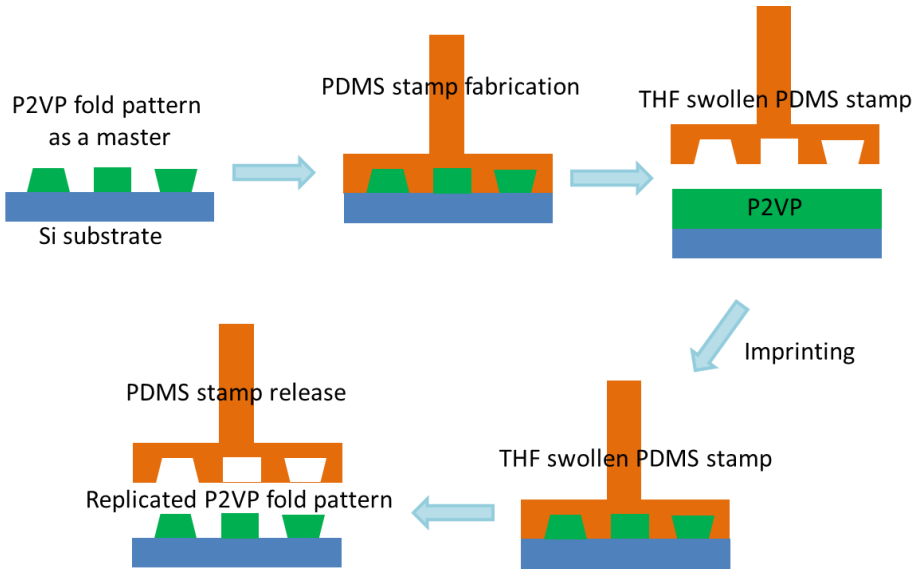

Figure S5. 7 Schematic illustration showing the procedure of replicating P2VP fold patterns using nanoimprinting technique.

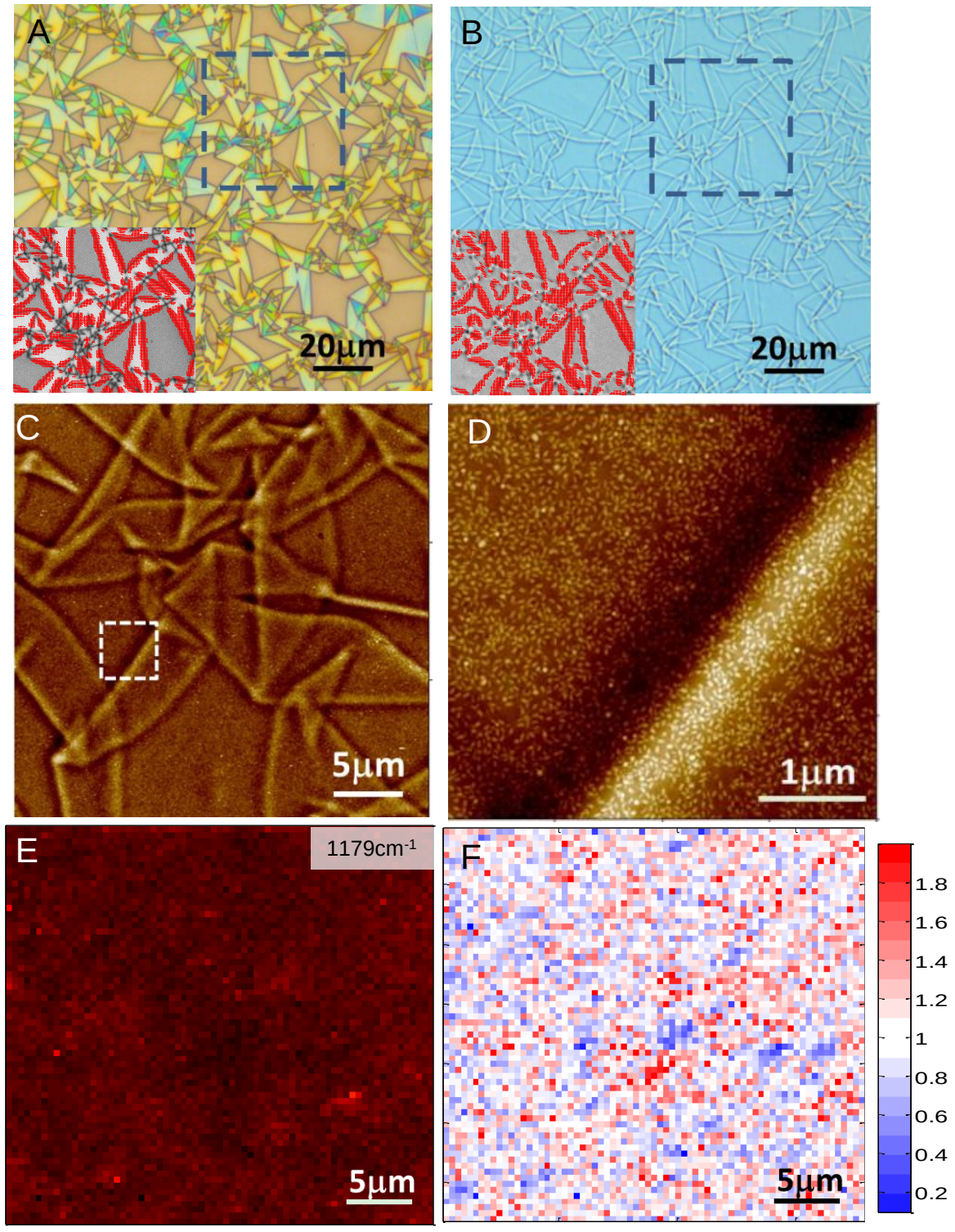

Figure S5. 8 (A) A bright-field optical micrograph of folded plasmonic gel use as a model master pattern. The inset shows the vector distribution of the outlined region. (B) Bright-field optical

micrograph of the duplicated lenticular pattern using a nanoimprinting method. The inset shows the similar vector distribution compared to the one from original image with a high correlation value of ~70%. (C) AFM images showing the replicated lenticular pattern adsorbed with a high density of gold nanorods (Height scale: 50 nm). (D) Magnified AFM image showing the uniform adsorption of gold nanorods across the entire surface. (E) SERS intensity map of pATP corresponding to Raman band at 1179 cm^{-1} showing uniform (featureless) distribution. SERS map intensity scale: 5×10^3 CPS. (F) SERS intensity ratio map of 1179 cm^{-1}/1381 cm^{-1} showing uniform (featureless) distribution, resulting from the uniformly adsorbed nanostructures as opposed to nondeterministic electromagnetic hotpots in the folded films.

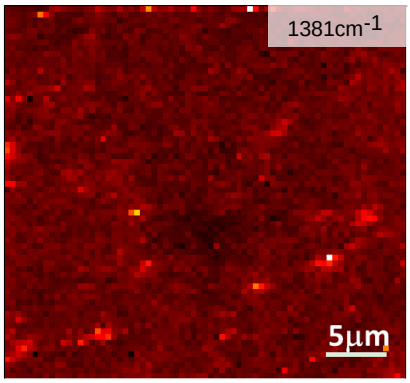

Figure S5. 9 SERS intensity map of 2-NT corresponding to Raman band at 1381 cm^{-1} showing uniform (featureless) distribution from the replicated pattern. SERS map intensity scale: 5×10^3 CPS.

Curriculum Vitae

Keng-Ku Liu

EDUCATION

2017 **Ph.D.**, Materials Science and Engineering, Washington University in St. Louis, St. Louis, MO
Advisor: Professor Srikanth Singamaneni
Dissertation: Hollow and Porous Plasmonic Nanostructures for Highly Efficient Chemical and Biological Sensing (August 2017)

2009 **M.S.**, Engineering and System Science, National Tsing Hua University, Hsinchu, Taiwan
Advisor: Professor Keh-Chyang Leou and Professor Chuen-Horng Tsai
Thesis: Synthesis of Horizontally Aligned Single-Walled Carbon Nanotubes Arrays by Chemical Vapor Deposition Method and High Frequency Characteristics Analysis

2006 **B.S.**, Engineering and System Science, National Tsing Hua University, Hsinchu, Taiwan

RESEARCH EXPERIENCE

2012-present **Graduate Research Assistant,** Washington University in St. Louis, St. Louis, MO

2010-2012 **Research Assistant**, Academia Sinica, Taipei, Taiwan

PUBLICATIONS

Refereed Journal Publications

1. **Liu, K.-K.**; Tadepalli, S.; Wang, Z.; Jiang, Q.; Singamaneni, S., Structure-dependent SERS Activity of Plasmonic Nanorattles. 2017 (submitted)

2. Tadepalli, S.; Cao, S.; Saha, D.; **Liu, K.-K.**; Chen, A.; Bae, S. H.; Raman, B.; Singamaneni, S., Remote-controlled Insect Navigation using Plasmonic Nanotattoos. 2017 (submitted)

3. Liu, J.-N.; Huang, Q.; **Liu, K.-K.**; Singamaneni, S.; Cunningham, B. T., Nanoantenna-Microcavity Hybrids with Highly Cooperative Plasmonic-Photonic Coupling. 2017 (submitted)

4. Jiang, Q.; Ghim, D.; Tadepalli, S.; **Liu, K.-K.**; Kwon, H.; Luan, J.; Min, Y.; Jun, Y.-S; Singamaneni, S., Biofouling-resistant Ultrafiltration Membrane by Harnessing Sunlight. 2017 (submitted)

5. Wang, C.; Sun, H.; Tadepalli, S.; **Liu, K.-K.**; Luan, J.; Jiang, Q.; Morrissey, J. J.; Kharasch, E. D.; Singamaneni, S., Metal-Organic Framework as a Protective Encapsulants for Biospecimen Preservation. 2017 (submitted)

6. Jiang, Q.; Kacica, C.; Soundappan, T.; **Liu, K.-K.**; Tadepalli, S.; Biswas, P.; Naik, R. R.; Singamaneni, S., In situ Grown Bacterial Nanocellulose/Graphene Oxide Composite for Flexible Supercapacitor. ***Journal of Materials Chemistry A*** 2017 (Accepted)

7. Tadepalli, S.; Wang, Z.; **Liu, K.-K.**; Jiang, Q.; Slocik, J.; Naik, R. R.; Singamaneni, S., Influence

of Surface Charge of the Nanostructures on the Biocatalytic Activity. ***Langmuir*** 2017, DOI: 10.1021/acs.langmuir.6b04490

8. **Liu, K.-K.**; Jiang, Q.; Tadepalli, S.; Raliya, R.; Biswas, P.; Naik, R. R.; Singamaneni, S., Wood-Graphene oxide Composite for Highly Efficient Solar Steam Generation and Desalination. ***ACS Applied Materials & Interfaces*** 2017, 9 (8), 7675-7681

9. Wang, C.; Tadepalli, S.; Luan, J.; **Liu, K.-K.**; Morrissey, J. J.; Kharasch, E. D.; Naik, R. R.; Singamaneni, S., Metal-Organic Framework as a Protective Coating for Biodiagnostic Chips. ***Advanced Materials*** 2017, 29, 1604433

10. Yuan, M.; **Liu, K.-K.**; Singamaneni, S.; Chakrabartty, S., Self-Powered Forward Error-Correcting Biosensor Based on Integration of Paper-Based Microfluidics and Self-Assembled Quick Response Codes. ***IEEE Transactions on Biomedical Circuits and Systems*** 2016, *PP* (99), 1-9.

11. Wang, C.; Luan, J.; Tadepalli, S.; **Liu, K.-K.**; Morrissey, J. J.; Kharasch, E. D.; Naik, R. R.; Singamaneni, S., Silk-Encapsulated Plasmonic Biochips with Enhanced Thermal Stability. ***ACS Applied Materials & Interfaces*** 2016, *8* (40), 26493-26500.

12. Tian, L.; Luan, J.; **Liu, K.-K.**; Jiang, Q.; Tadepalli, S.; Gupta, M. K.; Naik, R. R.; Singamaneni, S., Plasmonic Biofoam: A Versatile Optically Active Material. ***Nano Letters*** 2016, *16* (1), 609-616.

13. Tian, L.; **Liu, K.-K.**; Fei, M.; Tadepalli, S.; Cao, S.; Geldmeier, J. A.; Tsukruk, V. V.; Singamaneni, S., Plasmonic Nanogels for Unclonable Optical Tagging. ***ACS Applied Materials & Interfaces*** 2016, *8* (6), 4031-4041.

14. Tian, L.; Jiang, Q.; **Liu, K.-K.**; Luan, J.; Naik, R. R.; Singamaneni, S., Bacterial Nanocellulose-Based Flexible Surface Enhanced Raman Scattering Substrate. ***Advanced Materials Interfaces*** 2016, *3* (15), DOI: 10.1002/admi.201600214.

15. Schmucker, A. L.; Tadepalli, S.; **Liu, K.-K.**; Sullivan, C. J.; Singamaneni, S.; Naik, R. R., Plasmonic paper: a porous and flexible substrate enabling nanoparticle-based combinatorial chemistry. ***RSC Advances*** 2016, *6* (5), 4136-4144.

16. Luan, J.; **Liu, K.-K.**; Tadepalli, S.; Jiang, Q.; Morrissey, J. J.; Kharasch, E. D.; Singamaneni, S., PEGylated Artificial Antibodies: Plasmonic Biosensors with Improved Selectivity. ***ACS Applied Materials & Interfaces*** 2016, *8* (36), 23509-23516.

17. **Liu, K.-K.**; Tadepalli, S.; Kumari, G.; Banerjee, P.; Tian, L.; Jain, P. K.; Singamaneni, S., Polarization-Dependent Surface-Enhanced Raman Scattering Activity of Anisotropic Plasmonic Nanorattles. ***The Journal of Physical Chemistry C*** 2016**,** *120* (30), 16899-16906.

18. Jiang, Q.; Tian, L.; **Liu, K.-K.**; Tadepalli, S.; Raliya, R.; Biswas, P.; Naik, R. R.; Singamaneni, S., Bilayered Biofoam for Highly Efficient Solar Steam Generation. ***Advanced Materials*** 2016, 28, 9400-9407

19. Huang, G.; Tian, L.; **Liu, K.-K.**; Hu, B.; Xu, F.; Lu, T. J.; Naik, R. R.; Singamaneni, S., Elastoplastic Deformation of Silk Micro- and Nanostructures. ***ACS Biomaterials Science & Engineering*** 2016, *2* (6), 893-899.

20. Tadepalli, S.; Kuang, Z.; Jiang, Q.; **Liu, K.-K.**; Fisher, M. A.; Morrissey, J. J.; Kharasch, E. D.; Slocik, J. M.; Naik, R. R.; Singamaneni, S., Peptide Functionalized Gold Nanorods for the Sensitive Detection of a Cardiac Biomarker Using Plasmonic Paper Devices. ***Scientific Reports*** 2015, *5*, 16206.

21. Ray, J. R. [#]; Tadepalli, S. [#]; Nergiz, S. Z.; **Liu, K.-K.**; You, L.; Tang, Y.; Singamaneni, S.; Jun, Y.-S., Hydrophilic, Bactericidal Nanoheater-Enabled Reverse Osmosis Membranes to Improve Fouling Resistance. ***ACS Applied Materials & Interfaces*** 2015, *7* (21), 11117-11126. ([#] equal contribution)

22. **Liu, K.-K.**; Tadepalli, S.; Tian, L.; Singamaneni, S., Size-Dependent Surface Enhanced Raman Scattering Activity of Plasmonic Nanorattles. ***Chemistry of Materials*** 2015, *27* (15), 5261-5270.

23. Tian, L.; Tadepalli, S.; Hyun Park, S.; **Liu, K.-K.**; Morrissey, J. J.; Kharasch, E. D.; Naik, R. R.; Singamaneni, S., Bioplasmonic calligraphy for multiplexed label-free biodetection. ***Biosensors and Bioelectronics*** 2014, *59*, 208-215.

24. Tian, L.; Tadepalli, S.; Farrell, M. E.; **Liu, K.-K.**; Gandra, N.; Pellegrino, P. M.; Singamaneni, S., Multiplexed charge-selective surface enhanced Raman scattering based on plasmonic calligraphy. ***Journal of Materials Chemistry C*** 2014, *2* (27), 5438-5446.

25. Tian, L. [#]; **Liu, K.-K.** [#]; Morrissey, J. J.; Gandra, N.; Kharasch, E. D.; Singamaneni, S., Gold nanocages with built-in artificial antibodies for label-free plasmonic biosensing. ***Journal of Materials Chemistry B*** 2014, *2* (2), 167-170. ([#] equal contribution)

26. Jaiswal, A. [#]; Tian, L. [#]; Tadepalli, S.; **Liu, K.-K.**; Fei, M.; Farrell, M. E.; Pellegrino, P. M.; Singamaneni, S., Plasmonic Nanorattles with Intrinsic Electromagnetic Hot-Spots for Surface Enhanced Raman Scattering. ***Small*** 2014, *10* (21), 4287-4292. ([#] equal contribution)

27. Tsai, D.-S.; **Liu, K.-K.**; Lien, D.-H.; Tsai, M.-L.; Kang, C.-F.; Lin, C.-A.; Li, L.-J.; He, J.-H., Few-Layer MoS2 with High Broadband Photogain and Fast Optical Switching for Use in Harsh Environments. ***ACS Nano*** 2013, *7* (5), 3905-3911.

28. Lin, C.-T.; Loan, P. T. K.; Chen, T.-Y.; **Liu, K.-K.**; Chen, C.-H.; Wei, K.-H.; Li, L.-J., Label-Free Electrical Detection of DNA Hybridization on Graphene using Hall Effect Measurements: Revisiting the Sensing Mechanism. ***Advanced Functional Materials*** 2013, *23* (18), 2301-2307.

29. Pu, J.; Yomogida, Y.; **Liu, K.-K.**; Li, L.-J.; Iwasa, Y.; Takenobu, T., Highly Flexible MoS2 Thin-Film Transistors with Ion Gel Dielectrics. ***Nano Letters*** 2012, *12* (8), 4013-4017.

30. **Liu, K.-K.** [#]; Zhang, W. [#]; Lee, Y.-H.; Lin, Y.-C.; Chang, M.-T.; Su, C.-Y.; Chang, C.-S.; Li, H.; Shi, Y.; Zhang, H.; Lai, C.-S.; Li, L.-J., Growth of Large-Area and Highly Crystalline MoS2 Thin Layers on Insulating Substrates. ***Nano Letters*** 2012, *12* (3), 1538-1544. ([#] equal contribution)

31. Lin, Y.-C. [#]; Zhang, W. [#]; Huang, J.-K.; **Liu, K.-K.**; Lee, Y.-H.; Liang, C.-T.; Chu, C.-W.; Li, L.-J., Wafer-scale MoS2 thin layers prepared by MoO3 sulfurization. ***Nanoscale*** 2012, *4* (20), 6637-6641. ([#] equal contribution)

32. Lin, Y.-C.; **Liu, K.-K.**; Wu, C.-Y.; Chu, C.-W.; Wang, J. T.-W.; Liang, C.-T.; Li, L.-J., Efficient reduction of graphene oxide catalyzed by copper. ***Physical Chemistry Chemical Physics*** 2012, *14* (9), 3083-3088.

33. Lee, Y.-H.; **Liu, K.-K.**; Lu, A.-Y.; Wu, C.-Y.; Lin, C.-T.; Zhang, W.; Su, C.-Y.; Hsu, C.-L.; Lin, T.-W.; Wei, K.-H.; Shi, Y.; Li, L.-J., Growth selectivity of hexagonal-boron nitride layers on Ni with various crystal orientations. ***RSC Advances*** 2012, *2* (1), 111-115.

34. He, S.; **Liu, K.-K.**; Su, S.; Yan, J.; Mao, X.; Wang, D.; He, Y.; Li, L.-J.; Song, S.; Fan, C., Graphene-Based High-Efficiency Surface-Enhanced Raman Scattering-Active Platform for Sensitive and Multiplex DNA Detection. ***Analytical Chemistry*** 2012, *84* (10), 4622-4627.

35. Chen, C.-H. [#]; Lin, C.-T. [#]; Lee, Y.-H.; **Liu, K.-K.**; Su, C.-Y.; Zhang, W.; Li, L.-J., Electrical Probing of Submicroliter Liquid Using Graphene Strip Transistors Built on a Nanopipette. ***Small*** 2012, *8* (1), 43-46. ([#] equal contribution)

36. Zhang, W. [#]; Lin, C.-T. [#]; **Liu, K.-K.**; Tite, T.; Su, C.-Y.; Chang, C.-H.; Lee, Y.-H.; Chu, C.-W.; Wei, K.-H.; Kuo, J.-L.; Li, L.-J., Opening an Electrical Band Gap of Bilayer Graphene with Molecular Doping. ***ACS Nano*** 2011, *5* (9), 7517-7524. ([#] equal contribution)

37. Su, C.-Y. [#]; Lu, A.-Y. [#]; Wu, C.-Y.; Li, Y.-T.; **Liu, K.-K.**; Zhang, W.; Lin, S.-Y.; Juang, Z.-Y.; Zhong, Y.-L.; Chen, F.-R.; Li, L.-J., Direct Formation of Wafer Scale Graphene Thin Layers on Insulating Substrates by Chemical Vapor Deposition. ***Nano Letters*** 2011, *11* (9), 3612-3616. ([#] equal contribution)

38. Su, C.-Y.; F, D.; Lu, A.-Y; **Liu, K.-K.**; Xu, Y.; Juang, Z.-Y; Li, L.-J., Transfer printing of graphene strip from the graphene grown on copper wires. ***Nanotechnology*** 2011, *22* (18), 185309.

Book chapters

Tadepalli, S.; **Liu, K.-K.**; Singamaneni, S., Scanning Probe Investigation of Cellular and Subcellular Biomechanics. CRC Press 2014

Conference Proceeding

1. Liu, J.-N.; **Liu, K.-K.**; Huang, Q.; Singamaneni, S.; Cunningham, B. T, Photonic Crystal Coupled Plasmonic Hybrid Nanosensors, Hawaii, USA, Photonics Conference (IPC), IEEE, Oct. 2016

2. **Liu, K.-K.**; Jiang, Q.; Tadepalli, S.; Raliya, R.; Biswas, P.; Naik, R. R.; Singamaneni, S., Wood-Graphene Oxide Composite for Highly Efficient Solar Steam Generation and Desalination. St. Louis, USA, Missouri Materials Network, Oct. 2016

3. Tian, L.; **Liu, K.-K.**; Fei, M.; Tadepalli, S.; Cao, S.; Geldmeier, J.; Tsukruk, V.; Singamaneni, S., Harnessing Spontaneous Folding of Plasmonic Gel for Unclonable Optical Tags. Boston, USA, MRS Fall, Dec. 2015

4. **Liu, K.-K.**; Tadepalli, S.; Tian, L.; Singamaneni, S., Polarization-Dependent Surface Enhanced Raman Scattering Activity of Anisotropic Au Nanorattles. Boston, USA, MRS Fall, Dec. 2015

5. **Liu, K.-K.**; Tadepalli, S.; Tian, L.; Singamaneni, S., Size-Dependent Surface Enhanced Raman Scattering Activity of Plasmonic Nanorattles. Boston, USA, MRS Fall, Dec. 2015

6. Jiang, Q.; Tian, L.; **Liu, K.-K.**; Singamaneni, S., Bacterial Nanocellulose and Reduced Graphene Oxide Aerogel for Solar Steam Generation. Boston, USA, MRS Fall, Dec. 2015

7. Tian, L.; **Liu, K.-K.**; Luan, J.; Jiang, Q.; Tadepalli, S.; Naik, R.R.; Singamaneni, S., Plasmonic Aerogels from Bacterial Nanocellulose. Boston, USA, MRS Fall, Dec. 2015

8. Jiang, Q.; Tian, L.; **Liu, K.-K.**; Luan, J.; Naik, R.R.; Singamaneni, S., Ultra-Smooth Bacterial Nanocellulose-Based SERS Swab. Boston, USA, MRS Fall, Dec. 2015

9. Huang, G.; Tian, L.; **Liu, K.-K.**; Naik, R.R.; Xu, F.; Lu, T.J.; Singamaneni, S., Secondary Structure-Dependent Elastoplastic Deformation of Silk Micro- and Nanostructures. Boston, USA, MRS Fall, Dec. 2015

10. **Liu, K.-K.**; Tadepalli, S.; Tian, L.; Singamaneni, S., Size-dependent Surface Enhanced Raman Scattering Activity of Plasmonic Nanorattles. St. Louis, USA, WUSTL IMSE Showcase, Apr. 2015

11. Nergiz, S. Z.; Tadepalli, S.; **Liu, K.-K.**; Singamaneni, S., Plasmonic Sphere-in-Star Nanostructures for Raman-Based Theranostic Applications. Boston, USA, MRS Fall, Dec. 2014

12. Ray, J.; Tadepalli, S.; Nergiz, S. Z.; **Liu, K.-K.**; You, L.; Tang, Y.; Singamaneni, S.; Jun, Y.-S., Graphene Oxide-Gold Nanostar Hybrid Coating for Photothermally Active Multifunctional Reverse Osmosis Membranes. Boston, USA, MRS Fall, Dec. 2014

13. Tadepalli, S.; Tian, L.; Park, S. H.; **Liu, K.-K.**; Morrissey, J. J.; Kharasch, E. D.; Naik, R. R.; Singamaneni, S., Bioplasmonic Calligraphy: An Approach for Multiplexed Biosensing. Boston, USA, MRS Fall, Dec. 2014

14. Tadepalli, S.; Tian, L.; Farrell, M. E.; **Liu, K.-K.**; Gandra, N.; Pellegrino, P. M.; Singamaneni, S., Multiplexed Charge-Selective Surface Enhanced Raman Scattering Based on Plasmonic Calligraphy. Boston, USA, MRS Fall, Dec. 2014

15. **Liu, K.-K.**; Tadepalli, S.; Tian, L.; Singamaneni, S., Size-dependent Surface Enhanced Raman Scattering Activity of Plasmonic Nanorattles. St. Louis, USA, SLINN, Nov. 2014

16. Tian, L.; **Liu, K.-K.**; Morrissey, J. J.; Gandra, N.; Kharasch, E. D.; Singamaneni, S., Gold Nanocages with Built-in Artificial Antibodies for Label-free Plasmonic Biosensing. San Francisco, USA, MRS Spring, Apr. 2014

17. Tian, L.; **Liu, K.-K.**; Morrissey, J. J.; Gandra, N.; Kharasch, E. D.; Singamaneni, S., Artificial Antibodies for Label-free Plasmonic Biosensing. Boston, USA, MRS Fall, Dec. 2013

18. Tian, L.; Tadepalli, S.; Park, S. H.; **Liu, K.-K.**; Naik, R. R.; Singamaneni, S., Bioplasmonic Calligraphy for Multiplexed Label-free Biodetection. Boston, USA, MRS Fall, Dec. 2013

PATENTS

1. Direct Growth of Graphene on Substrates, Lain-Jong Li, Ching-Yuan Su, Ang-Yu Lu, Chih-Yu Wu, **Keng-Ku Liu**, US Patent, US 8685843 B2, 2014

2. Plasmonic Biosensors with Build-in Artificial Antibodies, Srikanth Singamaneni, Limei Tian, **Keng-Ku Liu**, Abdennour Abbas, Jeremiah J. Morrissey, Evan D. Kharasch, US Patent, US 20160282341 A1, 2014